# DYNAMICS OF LANGMUIR SUPERCELLS IN THE COASTAL OCEAN

by

YARGO TEIXEIRA GOMES DE MELO

(Under the Direction of C. Brock Woodson and Dana K. Savidge)

ABSTRACT

Langmuir circulations (LC) are phenomena that impact the mixing and transport of gases, heat, and momentum in the uppermost layer of the ocean. They appear as pairs of counterrotating vortices on the ocean surface, parallel to the direction of the wind. Recent studies have shown that in the coastal ocean, LC can extend through the entire water column under strong wind-wave conditions, forming Langmuir Supercells (LSC). LSCs drive significant mixing and transport not only in the surface layer of the ocean, but also in the bottom boundary layer, where wave mobilized sediments can be carried upwards. By analyzing velocity profiles and meteorological auxiliary data at different sites, researchers can better understand the dynamics and impact of LSC. This dissertation examines Langmuir Supercells to understand their behavior under different forcing conditions, how to evaluate them, and their structural organization at varying depths, including full parametrization and analysis of the deepest recorded LSC event to date. Herein I 1) propose a novel method of separation of waves and turbulence using rotary spectra analysis, 2) demonstrate existence of LSC events in a 40 m depth site while providing full parametrization, 3) propose a novel method to estimate heat flux sans pyranometry, and 4) examine and apply current methods to estimate organization of LSC to study effects of organization of LSC at varying depths.

INDEX WORDS: Turbulence, ADCP, Wind stress, Langmuir circulation, Coastal oceanography

DYNAMICS OF LANGMUIR SUPERCELLS IN THE COASTAL OCEAN

by

YARGO TEIXEIRA GOMES DE MELO

B.Sc., Pontificia Universidade Catolica de Minas Gerais, Brazil, 2016

M.Sc., Bucknell University, 2018

A Dissertation Submitted to the Graduate Faculty of The University of Georgia in Partial Fulfillment of the Requirements for the Degree

DOCTOR OF PHILOSOPHY

ATHENS, GEORGIA

2023

DYNAMICS OF LANGMUIR SUPERCELLS IN THE COASTAL OCEAN

by

YARGO TEIXEIRA GOMES DE MELO

| | |
|---|---|
| Major Professor: | C. Brock Woodson |
| | Dana K. Savidge |
| Committee: | David Emory Stooksbury |
| | R. Benjamin Davis |

Electronic Version Approved:

Ron Walcott
Vice Provost for Graduate Education and Dean of the Graduate School
The University of Georgia
May 2023

# DEDICATION

Com profunda gratidão à minha querida família e amigos, dedico esta tese de doutorado a todos vocês. Durante toda esta jornada, o amor, apoio e encorajamento inabaláveis de vocês foram minha fonte de força e motivação.

Aos meus pais, Rejane e Paulo, agradeço por instilarem em mim o amor pelo aprendizado e uma forte ética de trabalho. Seus sacrifícios e apoio inabalável tornaram possível para mim perseguir meus sonhos.

Aos meus irmãos, Yasmim e Rodolfo, obrigado por serem meus amigos e por sempre me animar, não importa o quão desafiador o caminho parecesse.

Aos meus queridos amigos, obrigado por estarem lá para mim em todos os momentos. Suas palavras gentis, risadas e apoio inabalável levantaram meu espírito e me ajudaram a perseverar.

Aos meus mentores e orientadores, Dana e Brock, agradeço por sua orientação, sabedoria e paciência. Seus conhecimentos e experiência me inspiraram a buscar a excelência em tudo que faço.

E um agradecimento especial à minha parceira, Sierra, que esteve ao meu lado em todos os momentos desta jornada. Seu amor, apoio e incentivo são inestimáveis e sou grato por tê-la em minha vida.

A todos vocês que desempenharam um papel importante em me tornar a pessoa que sou hoje, obrigado do fundo do meu coração. Esta conquista não teria sido possível sem o amor, o apoio e o encorajamento de vocês.

Com amor e gratidão,

Yargo Teixeira Gomes de Melo

ACKNOWLEDGEMENTS

Completing a PhD is a significant milestone that would not be possible without the support and contributions of many individuals. I am deeply grateful to those who have helped me along this journey and have contributed to my success.

First and foremost, I would like to express my sincere appreciation to my advisors, Dr. Brock Woodson and Dr. Dana Savidge. Their guidance, mentorship, and support have been invaluable throughout my doctoral studies. Dr. Woodson, thank you for taking a chance on me and trusting that my love for fluid dynamics would translate well into oceanography. Dr. Savidge, thank you for being patient with me and providing me with the necessary tools and knowledge to excel in a new field.

I would also like to extend my gratitude to my committee members, Dr. Ben Davis and Dr. David Stooksbury. Their feedback, insights, and guidance have significantly improved the quality and rigor of my research. Dr. Davis, thank you for taking a chance on me and being a pivotal factor in my decision to pursue my PhD at UGA. Dr. Stooksbury, thank you for introducing me to the importance of philosophy of science and expanding my perspective, reading Popper changed my internal paradigm.

I owe a debt of gratitude to my labmates, who have provided an inspiring and supportive research environment. Their camaraderie, knowledge-sharing, and encouragement have been essential to my personal and professional growth.

Finally, I would like to acknowledge the entire academic community for creating a culture of collaboration, learning, and innovation. The opportunities and experiences that have shaped my academic journey would not have been possible without this supportive community.

To my family and friends, thank you for your unwavering support, encouragement, and love throughout this journey. This accomplishment would not have been possible without you.

Yargo Teixeira Gomes de Melo

TABLE OF CONTENTS

LIST OF TABLES

LIST OF FIGURES

Page

# CHAPTER 1

# INTRODUCTION AND MOTIVATION

The surface layer of the ocean is of paramount importance for physical and biogeochemical dynamics, as it is a key region in which mixing and transport processes between the ocean and atmosphere occur. The various mechanisms that govern mixing and transport of gases, heat, and momentum in the upmost layer of the ocean are diverse in origin and in effect including tides, winds, surface waves, and buoyancy-driven currents (such as river inflows and internal waves). One of the most significant mechanisms of mixing in the surface layer is known as Langmuir circulation (LC) (Leibovich, 1983). LCs manifest as parallel pairs of vortices on the surface of the ocean due are well-studied, but only recently has attention been paid to LCs that span the whole water column in near coastal regions.

This dissertation explores the general characteristics of LCs, focusing on cases in which the circulations span the full depth of the water column, and reaching horizontal scales four to six times the water depth (Gargett and Wells, 2007), referred to as Langmuir supercells (LSCs) (Gargett et al., 2004). To achieve this goal, I analyzed three data sets at different coastal sites, with different water depths, one of which was collected at 39-meter waters, a site deeper than previously examined in literature on LSCs. After establishing the occurrence of LSCs at this deeper site, and later, the organization of the events at the different sites will be compared.

Chapter 2 of this dissertation presents a literature review of LSCs. The main objectives that will be addressed are presented in Chapter 3. Chapters 4, 5, and 6 are each a manuscript on:

a method to separate waves from fluctuations (Chapter 4), a novel method to estimate heat flux into and out of the ocean, used on the parametrization of LSC in 39-m waters (Chapter 5), and lastly, a comparison of structural organization of LSC at different depths (Chapter 6).

Chapter 7 is comprised of my final conclusions and suggestions for future work.

## 1.1 MOTIVATION

The coastal ocean is a highly dynamic environment characterized by complex interactions between physical, chemical, and biological processes. In particular, the transport and resuspension of sediments in the benthic boundary layer play a crucial role in shaping the structure and function of coastal ecosystems (Nelson et al., 1999; Jahnke et al., 2008; Savidge et al., 2008). An improved understanding of these processes is essential for the development of accurate and predictive coastal ocean models, which are necessary to inform coastal management and conservation efforts.

One of the most significant drivers of sediment transport on shallow continental shelves is the phenomenon of Langmuir Supercells (Gargett et al., 2004; Gargett et al., 2014; Savidge & Gargett, 2017). Langmuir Supercells are large, counter-rotating vortices that form under the combined influence of wind and waves (Gargett & Grosch, 2014). These powerful structures have the capacity to entrain sediments from the bottom boundary layer, resuspending them into the water column, where they can be transported considerable distances (Gargett et al., 2004; Gargett et al., 2016).

The impact of Langmuir Supercells on sediment transport has important implications for the biogeochemistry of the coastal ocean. The resuspension of benthic sediments may contain diatoms and other microorganisms (Cahoon et al., 1994), influencing nutrient cycling, altering the distribution of benthic microalgae, and affecting the light environment in the water column (Nelson et al., 1999; Jahnke et al., 2008; Savidge et al., 2008). Moreover, these processes can directly impact the functioning of benthic and pelagic ecosystems, with consequences for biodiversity and ecosystem services in the coastal zone (Gargett et al., 2004; Jahnke et al., 2008).

Despite the importance of Langmuir Supercells in coastal environments, their representation in coastal ocean models remains a challenge. This is due, in part, to the complex nature of the interactions between the wind, waves, and turbulence that drive the formation and evolution of these structures (Grosch & Gargett, 2016; Gargett & Savidge, 2020). Recent advancements in large-eddy simulation (LES) techniques and the development of new parameterizations for Langmuir Supercells have begun to address these challenges, enabling more accurate representations of these processes in coastal ocean models (Walker et al., 2016; Gargett & Savidge, 2020; Tejada-Martínez and Grosch., 2007). The importance of accounting for Langmuir Supercells in coastal models is crucial, as it can lead to better predictions of sediment transport and its associated impacts on coastal ecosystems.

Furthermore, the study of LSC has several engineering applications. For example, LSC can affect the dispersion and transport of pollutants, such as oil spills, in the ocean, making the study of LSC important for oil spill response strategies. Models with a better understanding of the dynamics of LSC can provide accurate spill response plan. Similarly, LSC can impact the distribution of sediments and nutrients in the coastal zone, making it important for coastal ecosystem management. By understanding the dynamics of LSC, engineers and coastal managers can develop more effective strategies to mitigate the impacts of LSC on these applications.

## 1.2 RESEARCH QUESTIONS

The importance of Langmuir Supercells in coastal environments and their impact on sediment transport, biogeochemistry, and ecosystem dynamics calls for further investigation to address knowledge gaps and improve our understanding of these complex phenomena. Based on the current state of the art, the following research questions emerge as key areas for exploration:

1. What are the underlying physical mechanisms that drive the formation, evolution, and decay of Langmuir Supercells in the coastal ocean, and how do these mechanisms interact with the surrounding environment (Gargett et al., 2004; Gargett & Grosch, 2014; Grosch & Gargett, 2016)?
2. How do the characteristics of Langmuir Supercells, such as their size, intensity, and duration, vary across different coastal settings, and what factors influence these variations (Gargett et al., 2014; Gargett et al., 2022)?
3. What role do Langmuir Supercells play in the transport and resuspension of sediment in deeper coastal environments compared to shallower regions, and how do these processes impact nutrient cycling, primary productivity, and benthic-pelagic coupling (Gargett et al., 2004; Savidge & Gargett, 2017)?
4. How can coastal ocean models be improved to better represent the effects of Langmuir Supercells on sediment transport and other biogeochemical processes, and what advancements in computational methods or parameterizations are needed to achieve this (Walker et al., 2016; Gargett & Savidge, 2020)?

Addressing these research questions is essential for advancing our understanding of Langmuir Supercells and their role in coastal environments. In particular, studying Langmuir Supercells in deeper coastal sites is crucial, as current research has predominantly focused on shallow shelves (Gargett et al., 2004; Savidge & Gargett, 2017). Investigating deeper sites may reveal new insights into the mechanisms driving the formation and dynamics of Langmuir Supercells, as well as their impact on sediment transport and ecosystem processes in these regions.

By answering these research questions, the scientific community will be better equipped to predict the effects of Langmuir Supercells on sediment transport, nutrient cycling, and ecosystem dynamics in the coastal ocean. Moreover, these findings will contribute to the ongoing development and refinement of coastal ocean models, ultimately leading to more accurate and reliable predictions of coastal processes and their consequences for coastal ecosystems and human societies.

## 1.3 HYPOTHESES

Given the importance of Langmuir Supercells in coastal environments and the need to better understand their occurrence and behavior in deeper coastal sites, I propose the following hypotheses for investigation:

1. Langmuir Supercells may occur in deeper coastal sites than what has been observed to date. Previous studies have primarily focused on shallow shelves (Gargett et al., 2004; Savidge & Gargett, 2017). However, it is possible that Langmuir Supercells could develop in deeper coastal environments, provided that the local conditions allow for the formation of intermediate-type waves (Gargett et al., 2004). Examining a dataset from 40-m depth coastal waters may reveal the existence of Langmuir Supercells in these

deeper environments and provide new insights into their characteristics, dynamics, and impact on sediment transport and biogeochemical processes.

2. The structural organization of Langmuir Supercells may vary with depth, due to changes in the orientation of Langmuir circulations as a function of depth. McWilliams et al. (1997) suggested that the orientation of Langmuir circulations could be influenced by the depth of the water column, which may, in turn, affect the organization and behavior of Langmuir Supercells. Investigating the structural organization of Langmuir Supercells in a 40-m depth dataset may provide valuable information on how these structures evolve with depth and how their interactions with the surrounding environment change as a result.

By testing these hypotheses, I will enhance our understanding of the occurrence, behavior, and impact of Langmuir Supercells in deeper coastal environments. This knowledge will contribute to the development of more accurate and comprehensive coastal ocean models, ultimately improving our ability to predict and manage the effects of Langmuir Supercells on sediment transport, nutrient cycling, and ecosystem dynamics in the coastal zone.

My contributions to this work include full parametrization of current flow in a 40-m depth site (CSP), which comprised of at least two Langmuir Supercell events. Full parameterizations include analysis of flow and meteorological datasets from VADCP and NDBC buoys, i.e., derivation of surface wave displacement spectra from velocity fluctuations, estimation of Stokes velocity and shear from the bottom to the water surface, wave characteristic analysis, estimation of dimensional and non-dimensional forcing parameters, creation of regime diagrams and forcing spaces to estimate dominant forcing in turbulent production. Similar analysis was undertaken with other published datasets (LEO and BUP) for validation and verification. Other contributions include proposal of a novel method for separating wave and turbulence from current data, proposal of a novel method to estimate heat-flux using SST when pyranometry is not available, and a comparison of structural organization between Langmuir Supercells at different depths.

# CHAPTER 2

# BACKGROUND AND RELATED WORK

LCs are named after the chemist Irving Langmuir, who first observed and characterized the events (Langmuir, 1938). LCs form due to the interaction between winds and waves on the surface of the ocean. Specifically, LCs develop from the interaction between Stokes drift (the average velocity of a fluid parcel as it travels with the flow) produced by surface gravity waves and vertical vorticity induced by wind-driven currents. LCs induce vertical mixing and transport which can lead to deepening of the mixed layer in the ocean's surface (Li et al., 2012) due to a combination of different forcing mechanisms, such as buoyancy, turbulence, and Langmuir forcing, all of which will be further explored in this review. The study of the mechanisms discussed above are instrumental for the understanding the complex effects on the ocean's surface caused by the interaction between ocean and atmosphere, from small-scale winds to those of strong tropical storms (Malarkey and Thorpe, 2016; Reichl et al., 2016; Teixeira, 2018; Wang et al., 2018).

LCs appear as pairs of parallel counter-rotating vortices aligned downwind (Fig. 2.1). As the wind stress acts on the surface layer, the pair of vortices may induce instability in the flow field, which can manifest on the surface as visible organized streaks with a clear gap in between. The downwind velocity component is significantly higher in the streak zones compared to the velocity in the gap zones, and the downwelling branches of the vortex pairs are faster than the upwelling branches. Given enough time, the streaks may become more chaotic, reaching a state known as Langmuir turbulence (McWilliams et al., 1997).

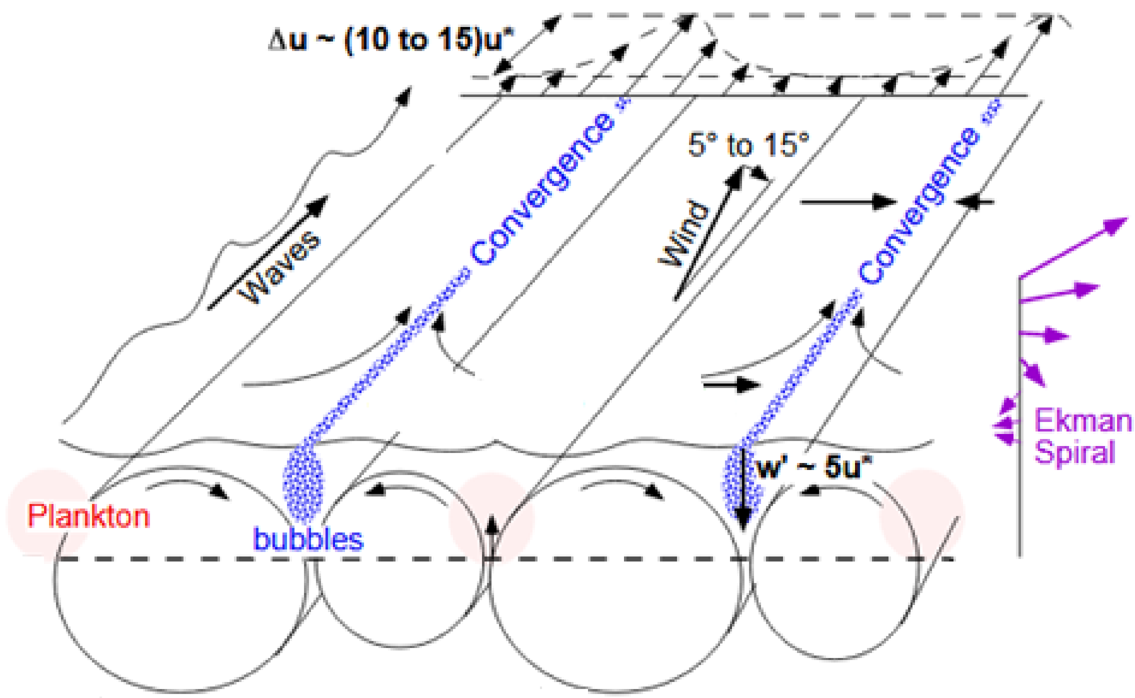


Figure 2.1 General layout of LCs on the onset of the wind (Adapted from Smith, 2001).

Craik and Leibovich (1976) proposed two distinct models (CL1 and CL2) aiming to mathematically describe the generation of LCs. Both models realistically reproduced a parallel system of vortices aligned with the wind. The resulting vortices possessed an asymmetric structure in which the downwelling speeds, aligned with the streaks, would be higher than the upwelling speeds, and comparable in scale to the mean downwind surface drift. The proposed mechanisms CL1 and CL2 are used in various computational models that aim to simulate the effects of LCs.

CL1, the first of the two proposed "vortex force" mechanisms, occurs when a fixed wind blows over otherwise undisturbed waters of unbounded length or depth, generating a surface wave field with unidirectional wind-aligned Stokes drift. If the surface velocity was only depth-dependent, the vortex force could be balanced by an analog of the hydrostatic pressure gradient. However, if the Stokes drift varies in the crosswind direction due to the current not being unidirectional, the vortex force cannot be balanced by pressure alone, which induces an overturning. Short-crested seas have surface waves of this character (Craik and Leibovich, 1976). If this overturning is maintained over a significant amount of time, torque may be generated due to horizontal fluctuations of the vortex force caused by a horizontal periodic wave, which would drive rolling motions.

The second proposed "vortex force" mechanism, CL2, does not require a coherent surface-wave structure, as the circulations are generated by the vortex force acting as an inviscid instability in the unidirectional current. Since the flow velocity decreases with depth, the flow is unstable if dissipation is sufficiently weak. In the absence of frictional effects, a current anomaly will lead to a convergence and be amplified. Through rotation and stretching of the vortex tube, another anomaly would be generated converged, and further amplified (Fig. 2.2).

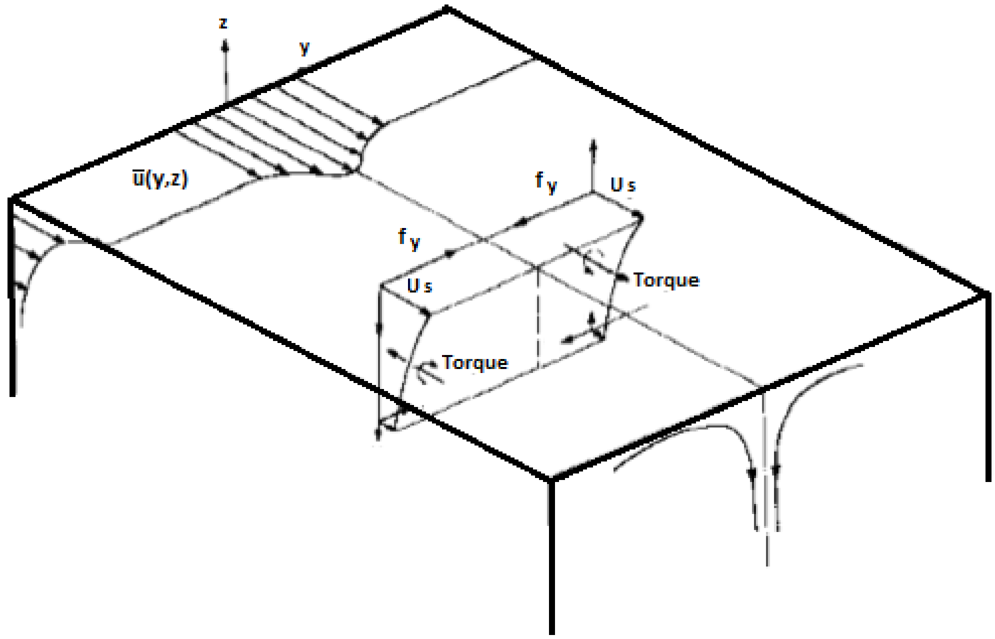


Figure 2.2 Illustration of the CL2 vortex force mechanism for generation of LC. The Stokes drift decreases with depth generating a torque. Perturbations on the current may stretch and rotate the vortex tubes amplifying and converging itself by stretching and rotating the vortex tubes, generating a side torque leading to overturning and crosswind vortex generation (adapted from Craik and Leibovich, 1976).

Using CL2, assuming the wind stress and the Stokes drift are parallel in the *x*-direction (downwind) and that eddy viscosity is not varying with depth, and ignoring stratification or surface heat flux, the Ekman definition for the wind stress can be used to derive spatially-averaged and nondimensionalized equations of motion:

$$\frac{\partial u}{\partial t} + v\ \frac{\partial u}{\partial y} + w\ \frac{\partial u}{\partial z} = La\nabla^2 u\ , \tag{2.1}$$

and,

$$\frac{\partial \Omega}{\partial t} + v\ \frac{\partial \Omega}{\partial y} + w\ \frac{\partial \Omega}{\partial z} = La\nabla^2 \Omega - \frac{du_s}{dz}\frac{\partial u}{\partial y}\, , \tag{2.2}$$

where $u_s$ is the Stokes drift, $\Omega$ is the vorticity, and *La* (further discussed below), is the Langmuir number, which represents a balance between the rate of diffusion and production of downwind vorticity caused by tilting and stretching due to the Stokes drift, i.e., the ratio of viscous to inertial forces governing the Langmuir circulation that is inversely related to the Reynolds number. *La* values in the ocean are usually on the order of 0.01 (Leibovich, 1983).

Rarely is a single forcing responsible for turbulence production in the oceans, and it is necessary to understand which forcing dominates the production of turbulence in order to improve current coastal LES models. Turbulence is generated at the surface of the ocean through direct action of the wind stress and indirectly though the effects of the wind on the surface waves, as well on the wind effects on convection and buoyancy flux. Gargett and Grosch (2014) demonstrated that situations dominated by either Langmuir vortex forcing or destabilizing surface heat flux can be identified by distinct locations in log (*La*-*Ra*) space. *La* and *Ra* are dimensionless numbers, each comparing two forcing terms in the equation of motion. *La* , the Langmuir number, is the ratio between diffusion and production of CL vortex forcing, and *Ra*, the Rayleigh number, is the ratio between buoyancy and viscous forcing. Plotted against one another, they graphically portray which effect is likely to dominate for given wind, wave, buoyancy inputs.

LCs may behave differently in shallow water regions compared to deeper regions as the LCs can be affected by the local bottom topography and depth (Chubarenko et al., 2010). However, despite the attention given to studying open-ocean Langmuir circulations, only recently has research addressed cases in which the vertical scale of Langmuir circulation reaches the full depth of the water column. Such events, called Langmuir Supercells, seem to only occur in shallow coastal regions and consequently interact with the bottom boundary layer leading to transport of sediments suspended by wave scour, elevating the sediments out of the bottom boundary layer into the middle of the water column, where horizontal velocities are larger than those in the bottom boundary layer. Gargett and Wells (2007) bring attention to the fact that most studies on LCs were taken in deep waters, where cell size is not limited by depth, leading to differences in maximum downwelling velocities which causes asymmetry of the width of upwelling and downwelling limbs, which are not affected by a bottom boundary layer. Another major difference between deep waters LCs and coastal LCs is the presence of strong bottom intensification in the latter (Gargett et al., 2004). The effects of stratification on coastal LC events, and further, how coastal LCs affect stratification, can help elucidate how LCs are formed and evolve in the open ocean.

The focus of this research is on the near coast full depth circulations or LSCs, which were only recently observed and studied for the first time. In April 2003, a vertical acoustic Doppler current profiler (VADCP) was installed 6 km off the coast of New Jersey (LEO15 observatory) in 15 m water depth. Shortly after, data revealed an interesting event in which the entire water column showed high particle backscatter during the passage of a powerful storm. Upon a more thorough examination of the data, Gargett et al. (2004) showed that the backscatter was highly patterned and correlated with the fluctuation of vertical velocity directly measured by the VADCP. High surface-origin backscatter was linked to downward vertical velocity fluctuations, and high bottom-origin backscatter was linked to upward vertical velocity fluctuations. The backscatter from the surface seemed to imply wave breaking, which is expected during the passage of storms, while the backscatter from the bottom of the water column exhibited high particle resuspension. This event was demonstrated to be compatible with full-depth Langmuir circulations and termed 'Langmuir supercells' by the authors (Fig. 2.3). Later, Dierssen et al. (2009), Scully et al. (2015), and Savidge and Gargett (2017) observed similar LSC events on the eastern Exuma region of the Bahamas (8 m depth), at about 1.5 km from the western shoreline of the Chesapeake Bay (14 m depth), and off the coast of Georgia (26 m depth), respectively.

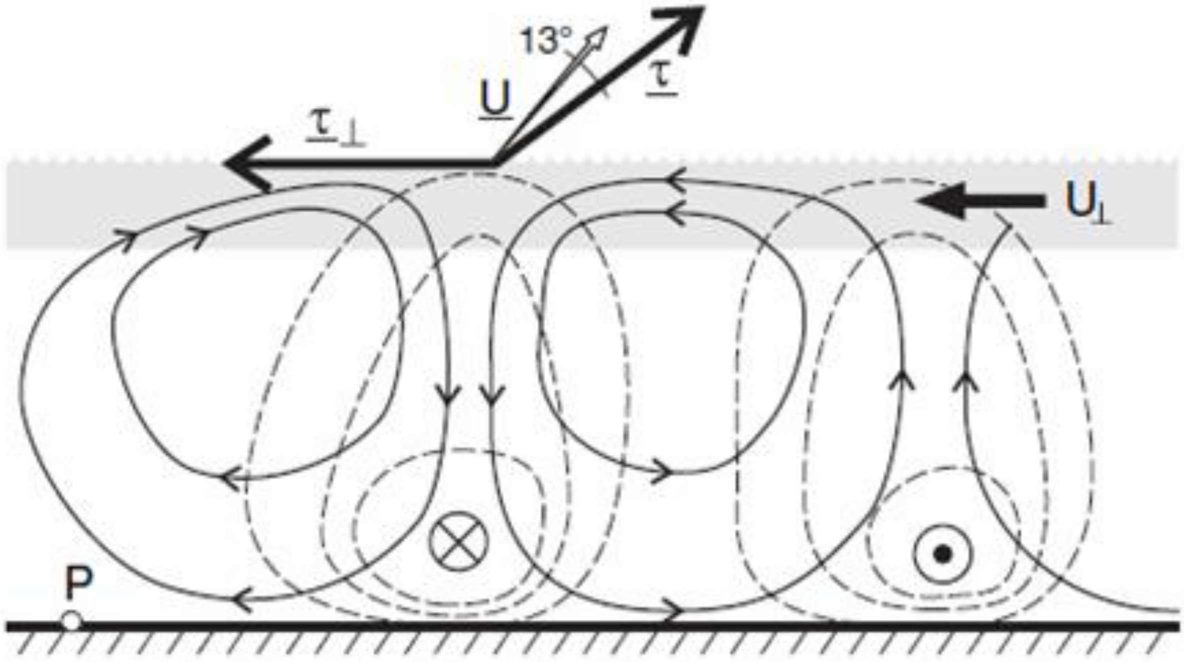


Figure 2.3 Basic features of LCs spanning full water depth in shallow coastal regions (Gargett et al., 2004).

CHAPTER 3

THEORETICAL FRAMEWORK

## 3.1 MODELING EQUATIONS

Turbulence may be generated in the surface layer of the oceans by different processes which may happen in isolation or simultaneously. The wind may produce turbulence by directly adding shear onto the ocean surface, or indirectly, through the effects of the wind on the wavefield due to the Langmuir vortex forcing as modeled by Craik and Leibovich (1976). Turbulence generated directly or indirectly by wind can be further superimposed on convection due to destabilizing surface buoyancy forcing (Gargett and Grosch, 2014).

Nondimensionalized equations of motion accounting for the three turbulence forcing processes discussed above can be used to understand when one of the processes dominates turbulence production, or when turbulence is produced by a mixture of the forcing processes. I follow the Gargett and Grosch (2014) derivation of nondimensional momentum equations in a wind-aligned coordinate system with positive $x_1$ as the downwind direction, $x_2$ as the crosswind direction, and $x_3$ as the depth positive upward from the surface. The assumptions are that density is a linear function of the deviation of a reference temperature ($T$), so that $(\rho - \rho_0) = -\alpha_T T$, where $\alpha_T$ is the thermal expansion coefficient, and that there is no rotation. Flow can be described by the wave-averaged Navier-Stokes equation (Craik and Leibovich, 1976) with added buoyancy effects:

$$\frac{Du_i}{Dt} = -\frac{1}{\rho_0}\frac{\partial \Pi}{\partial x_i} + \varepsilon_{ijn}\omega_n U_{S_j} + g\alpha_T T\delta_{i_3} + \upsilon\frac{\partial^2 u_i}{\partial x_j^2}, \quad (3.1)$$

where, $u_i$ is the $i$-th component of total wave-averaged velocity, $\omega_n$ is the $n$-th component of fluid vorticity, and $\upsilon$ is saltwater viscosity, $U_{S_j}$ is the downwind Stokes drift velocity estimated from the surface Stokes velocity $u_{s0}$, $g$ is the acceleration of gravity, and the pressure term:

$$\frac{\partial \Pi}{\partial x_i} = \frac{\partial}{\partial x_i}\left[\frac{p+P_0}{\rho_0} + \frac{1}{2}\left(U_{S_j}U_{S_j} + 2u_jU_{S_j}\right)\right], \tag{3.2}$$

which includes wave-averaged contributions on Stokes drift and imposed pressure gradient, $\frac{\partial P_0}{\partial x_i}$, which is assumed to be zero. With boundary conditions on velocity, $u_i = 0$ for i=1,3 at $x_3 = -H$; and $u_3 = 0$, $\left(\frac{\partial u_i}{\partial x_3}\right)_{x_3\,=\,0} = \frac{\tau}{\rho_0 \upsilon} = \frac{u_*^2}{\upsilon}$, $\frac{\partial u_2}{\partial x_3} = 0$, at $x_3 = 0$.

The temperature equation is obtained from the conservation of energy and conservation of mass equations under the Boussinesq approximation (density is only important when multiplied by a gravity ($g$) term).

$$\frac{DT}{Dt} = \kappa_T \frac{\partial^2 T}{\partial x_j^2}, \tag{3.3}$$

where $\kappa_T$ is the thermal diffusivity coefficient, with boundary conditions, $\frac{\partial T}{\partial x_3} = 0$ at $x_3 = -H$, and $\frac{\partial T}{\partial x_3} = \frac{-Q}{\kappa_T}$ at $x_3 = 0$, where $Q$ is the surface heat flux with convention $Q > 0$ being destabilizing and $Q < 0$ stabilizing.

**Estimating parameters**

The parameters needed to investigate the presence of LSC events in a dataset, following Gargett and Grosch (2014) are described below (see Table 3.1 for a list of variables and their definitions).

Table 3.1: Reference table for key parameters and equations.

| Variable | Description | Calculation |
|---|---|---|
| $U(x_3)$ | Mean velocity | From VADCP data |
| $U_S(x_3)$ | Stokes velocity | Equations 3.11/3.12 |
| $u_*$ | Surface stress velocity scale | $u_* = \left(\frac{\tau}{\rho_0}\right)^{1/2\,*}$ |
| $u_{S0}$ | Surface Stokes velocity | $u_{S0} = U_S(0)$ |
| $t_*$ | Time scale | Equation 3.5 |
| *Ra* | Rayleigh number | Equation 3.4 |
| *La* | Langmuir number | Equation 3.6 |
| | | (*$\boldsymbol{\tau}$ is the shear stress, and $\boldsymbol{\rho_0}$ is the density) |

The Rayleigh number is estimated as:

$$Ra = \left(\frac{\alpha_T g}{\kappa_T}\right)(Qt_*^2). \tag{3.4}$$

Where $\alpha_T$ is the coefficient of thermal expansion, $g$ is the acceleration of gravity, $\kappa_T$ is the thermal conductivity, $Q$ is the surface heat flux, and $t_*$ is a time scale (Thorpe, 2004), $t_* = g_*^{-1}$, $g_*$ being the LSC growth rate:

$$t_* \equiv \left(\frac{dU_s}{dx_3}\frac{dU}{dx_3}\right).^{-1/2} \tag{3.5}$$

And the Langmuir number is defined as:

$$La \equiv \left(\frac{u_*}{u_{S_0}}\right). \tag{3.6}$$

Where $U_S$ is the Stokes velocity, $U$ is the mean velocity, $u_*$ is the surface stress velocity, and $u_{S_0}$ is the surface Stokes velocity.

While a wave field is fundamentally represented by surface displacement spectra, other parameters measured by the VADCP in the subsurface can be used (pressure or vertical velocity) that have higher precision than what the bin size increment in surface position would provide. The appendix of Gargett and Grosch (2014) shows that for a single inviscid, incompressible wave with amplitude *a*, wavenumber *k*, frequency $\omega$, where *H* is water column depth, and surface displacement is ς = *a*cos(*kx*-$\omega$t), surface displacement variance relates to the variance of vertical velocity ($\langle w_h \rangle^2$) measured at height above bottom *h* as shown:

$$\langle \varsigma^2 \rangle = \langle {w_h}^2 \rangle \left( \frac{\sinh(kH)}{\omega \sinh(kh)} \right)^2 \tag{3.7}$$

This method assumes that the surface wave spectrum depends only on frequency (wave number) when winds and waves are aligned. It is further assumed that $\langle w_h \rangle^2 = \int_0^\infty \Phi_w(\omega) d\omega$ can be converted to an operator so the vertical velocity spectrum relates to surface displacement spectrum as:

$$\langle \varsigma^2 \rangle = \int_0^\infty \Phi_\sigma(\omega) d\omega = \int_0^\infty \Phi_w(\omega) \left( \frac{\sinh(kH)}{\omega \sinh(kh)} \right)^2 d\omega. \tag{3.8}$$

Assuming a unidirectional surface wave spectrum, the vertical shear Stokes velocity is the integral over a Stokes shear function *S*($\omega$,$x_3$) defined as:

$$\frac{dU_S(x_3)}{dx_3} = \int_0^\infty 2\, \Phi_\sigma(\omega) \omega k^2 \frac{\sinh(2k)(x_3+H)}{sinh^2(kH)} d\omega \tag{3.9}$$

$$= \int_0^\infty S(\omega, x_3) d\omega.$$

where $\omega$ and *k* are related by the full-dispersion relationship

$$\omega^2 = gk \tanh(kH). \tag{3.10}$$

and the displacement spectrum $\Phi_\sigma$ is estimated from $\Phi_w$, the noise-corrected spectrum of vertical velocity measured by the vertical beam of the VADCP at height, *h*, above bottom (depth $x_3$ = -(*H* – *h*)).

Since Equation 3.9 is integrated between 0 and infinite frequency, Stokes shear may become unbounded. Gargett and Grosch (2014) shows that it is bounded when computed at distances sufficiently below $x_3$ = 0.

A spectral Stokes velocity associated with surface wave displacement spectrum $\Phi_\sigma$ is given by the integral over frequency of a Stokes function $S(\omega, x_3)$:

$$U_S(x_3) = \int_0^\infty 2\Phi_\sigma(\omega)\omega k \frac{\cosh(2k)(x_3+H)}{2sinh^2(kH)} d\omega = \int_0^\infty S(\omega, x_3) d\omega, \quad (3.11)$$

The surface Stokes velocity $U_{S_0} \equiv U_S$ ($x_3$=0) can be unbounded, but the Stokes velocity can be calculated by evaluating the equation above at a small depth below the surface or by band limiting the surface integral. The latter option has been chosen and $u_{S_0}$ is computed as the integral of the Equation 3.11 above at $x_3 = 0$ over the range $0.005 < f < 0.4$ cps.

Gargett and Savidge (2020), however, presented a major addition to this method using a formulation of the directional wave spectra from ADCP vertical beam and slant beam velocities, the new equation becomes:

$$U_S(x_3) = \int_0^{2\pi} \int_0^\infty 2\Phi_\sigma(\omega,\theta)\omega k \frac{cosh2k(x_3+H)}{2sinh^2kH} d\omega d\theta = \int_0^{2\pi} \int_0^\infty S(\omega, x_3) d\omega, \quad (3.12)$$

Directional wave spectra calculated as in Equation 3.12 was used to verify if the assumption of alignment between winds and waves during the LSC events studied herein is valid.

## 3.2 AVAILABLE DATA

In this dissertation I make use of observational data from three distinct deployments of bottom-mounted 5 beam Vertical Acoustic Current Profilers (VADCP, leveled to be within less than a half degree of tilt and roll), alongside a set of auxiliary meteorological data available near the sites of deployment.

The first deployment occurred in 15 m depth waters off the coast of New Jersey, installed with NSF/NOAA funding on a bottom platform at the LEO-15 cabled ocean observatory (Gargett and Wells, 2007). Velocity fluctuations were measured from April 25$^{th}$ until October 31$^{st}$, 2003. Analysis of this deployment led to the first observation of LSC. Details of this deployment and analysis are available in Gargett et al. (2004) and Gargett et al. (2014). Herein, dataset related to this deployment will be referred to as LEO.

The second deployment occurred in 26 m depth waters on the Georgia mid-shelf, near Cape Hatteras at Navy Tower R2, between 2007 and 2009, as part of the NSF-funded Benthic Observatory Technology Tested on the Mid-Shelf – Understanding Processes (BOTTOMS-UP) project, imbedded within the existing longer-term observatory South Atlantic Bight Synoptic Ocean Observing Network (SABSOON) (Seim, 2000). In this dissertation I will refer to this dataset as BUP. Details of this deployment are available in Savidge et. al. (2008), Gargett et al. (2014), Savidge and Gargett (2017), Gargett and Savidge (2020), and Gargett (2022).

Lastly, an NSF funded 2015 deployment occurred off the coast of Duck, North Carolina in roughly 40 m depth waters as an addition to the ONR-funded Coupled Air-Sea Processes and Electromagnetic Wave ducting Research (CASPER) project (Wang et al., 2016). This VADCP deployment is referred to as CSP. Further in-depth explanation of characteristics and available auxiliary data for this and the other deployments are explored in Chapter 5.

### 3.3 WAVE SPECTRA ANALYSIS

Presented here are the downwind surface wave spectra following methodology presented in section 3.1, during different Langmuir Supercell (LSC) events starting from their genesis and extending for a few days past the end of an event. A time-series analysis is also offered for some of the events as a reference, plots, and data from Savidge and Gargett (2017) and Gargett and Savidge (2020) were used with authorization from the authors.

The first data set from the Bottoms-UP project (BUP), detailed in Savidge and Gargett (2017), was collected using a 600 kHz custom-built VADCP composed of four slant beams at a 30-degree angle from vertical, as well as a vertical center beam. Data was sampled at 1 Hz. All bins are 0.95 meters in size with the first bin starting at 1.6 meters above bottom with center at 2.66 meters above bottom. The VADCP was located about half a kilometer East-Southeast from the R2 tower, at approximately 26 m isobath, 65 km away from the Georgia coast. The data was divided into 7-day sessions and each session was further separated into 2-hour records. The sessions of interest here are 17, 18 (September 13th through 26th, 2007) and 21 (October 12th through 18th, 2007) including data before the onset, and after the cessation of a particular LSC event that lasted from September 16th to September 21st, 2007.

Data processing steps outlined in Savidge and Gargett (2017) were followed. Meteorological instruments on the R2 tower measured wind speed and direction, relative humidity, air temperature, barometric pressure, as well as shortwave and longwave radiation (Seim, 2000). The wind stress was estimated from wind speed data (Smith, 1988). Bulk heat and momentum fluxes were also calculated and used to estimate buoyancy forcing (Fairall et al., 1996). R2 data also included 6-min average water temperature throughout the water column (HOBO T-string), providing a way of identifying when the 26 m deep water column became unstratified.

Data above surface was eliminated, backscatter from the 5th beam of the VADCP was corrected for beam spreading and absorption, and data of the top 15% (9% for CSP) of the water column was eliminated from the slant beam data due to side-lobe contamination (required by the

30$^o$, 25$^o$ for CSP, slant beam angle to the vertical). A fish identification algorithm was also used to remove anomalous pings. A low-pass cut-off filter (20 sec) was used to eliminate wave-induced velocities (Savidge and Gargett, 2017).

Supplementary to the data processing found in Savidge and Gargett (2017) and Gargett and Grosch (2014) described further data processing to compute the (assumed downwind) wave spectra, that could further be used to estimate a proxy for the downwind Stokes velocity.

Figure 3.1 depicts the time series records for the period between 9/15/07 and 9/23/07. This is the event described in detail in Savidge and Gargett. High backscatter appears on the bottom and top of the water column on the afternoon of the 16th (Fig. 3.1a) with associated strong vertical velocities (Fig. 3.1b). The water column ceases to be stratified late that afternoon (Fig. 3.1c) coinciding with increased significant wave height (Fig. 3.1e), early that afternoon, strong winds started blowing in a single direction (Fig. 3.1f).

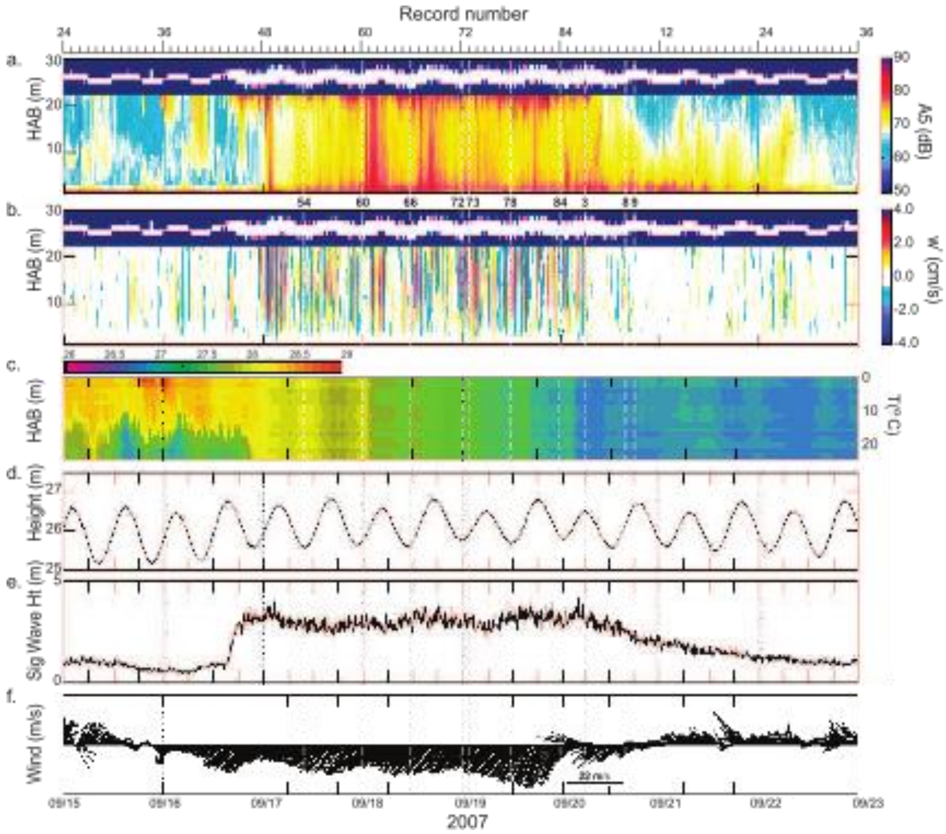

Figure 3.1 High wind and wave event recorded at R2, September 2007.Vertical beam acoustic Doppler current profiler (VADCP) data were subdivided into approximately 7-day sessions, subdivided and sequentially numbered into 2 h records. Shown are session 17, records 46–84, and session 18, records 1–36, 15–23 September 2007 (record numbers marked at the top). Panels are backscatter (a) and vertical velocity (b) from the VADCP fifth beam, with surface location (white) as identified in vertical beam backscatter; temperature evolution (c); low-frequency plus tidal water depth variation (d); significant wave height (e); and vector wind at 50 m (f). Panels a,b,c plotted as a function of height above bottom (HAB) in m, extracted from Savidge and Gargett (2017).

Presented in Figure 3.2 are some metrics of temporal variability for sessions 17 and 18. Of note is the vertical velocity variability (Fig. 3.2b), with lower values before and after the event, with higher values during the events and peaks at roughly 12-hour intervals. As for the forcing time series, the growth rates characteristic for LC are calculated and shown in Figure 3.3, as well as the Rayleigh number.

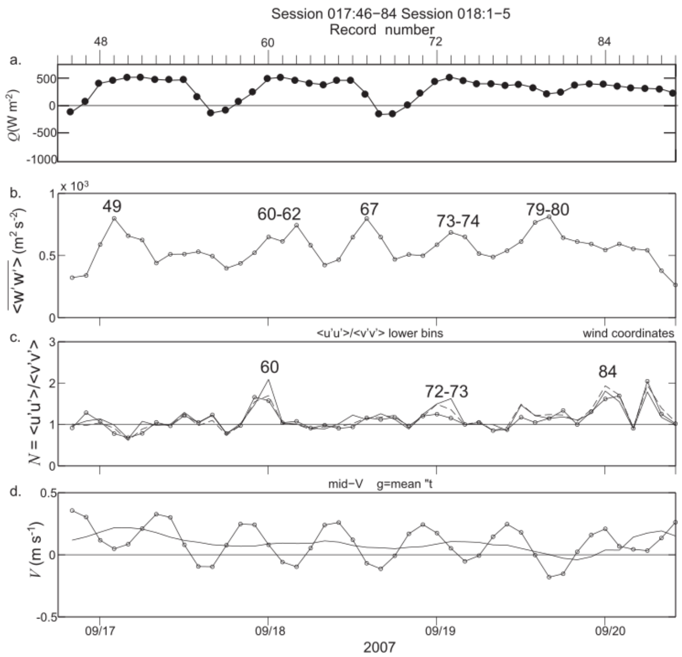


Figure 3.2 Time series of 2-h average quantities during the Langmuir supercell event in BUP: session 17, records 46–84 and session 18, records 1–5. (a) Surface heat flux, positive out of the ocean. (b) Depth-averaged vertical velocity variance $\overline{<w^2>}$ . (c) Nose diagnostic $N = \overline{\langle u'u' \rangle}/\overline{\langle v'v' \rangle}$ for bins 1–3 (bin 1, line with circles; bin 2, dashed line; bin 3, solid line). (d) Mid depth horizontal crosswind velocity, V (line with circles represents tide plus slowly varying mean; solid line represents mean only). Wind direction shifted suddenly at record 18.03, the third data point after record 17.84, the last record of session 17. Records discussed in the text are marked with record numbers in panels (b) and (c), adapted from Savidge and Gargett (2017).

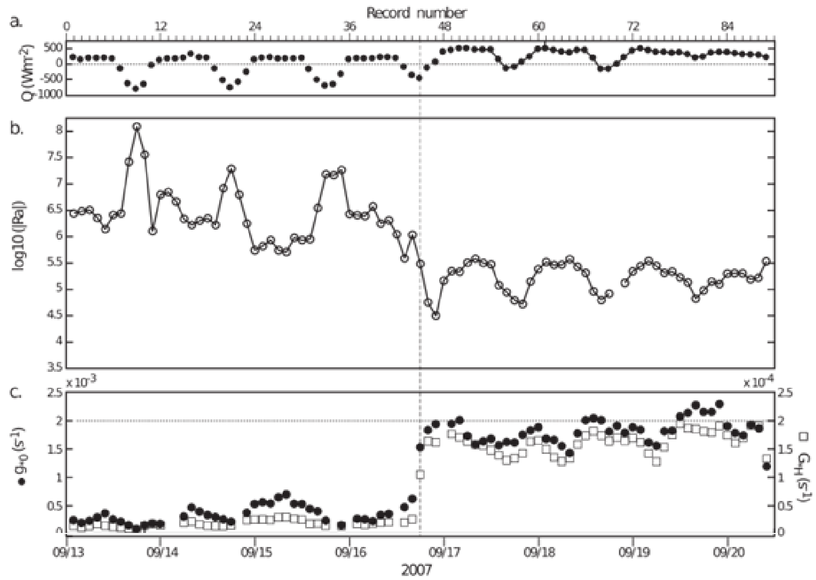


Figure 3.3 Time series of 2-h average quantities during the Langmuir supercell event of session 17, records 0–84 and session 18, records 1–5. (a) Surface heat flux, positive out of the ocean. (b) log of the Rayleigh number, $Q > 0$ implies destabilizing heat flux. (c) Near-bottom and near surface LC characteristic growth rates.

The velocity power density was calculated using Welch's method and corrected for the noise floor. A downwind displacement density spectrum was extracted by multiplying the velocity power density by the dispersion relation. The noise floor was estimated as a two-hour mean of the vertical velocity recorded near bottom during low to non-existent wind and wave forcing.

Figure 3.4 depicts the resulting (total, assumed downwind) displacement spectrum using a Hovmöller diagram. Using a base water depth of 26 m, the frequencies for transition to intermediate wave type from deep and shallow were calculated using, respectively, the 1/2 and 1/20 wavelength criteria and plotted as vertical reference dash-dotted lines. The energy density is concentrated in the intermediate wave frequency range, starting in the afternoon of the 16$^{th}$, coinciding with a sudden increase of LC growth rate both near bottom and near surface (Fig. 3.3c). In the morning of the 20th, the wind changes direction (Fig. 3.1f) followed by a decrease in the frequency of the displacement spectral density as the significant wave height diminishes (Fig. 3.1e) and the spectral density returns to normal levels with the end of the event.

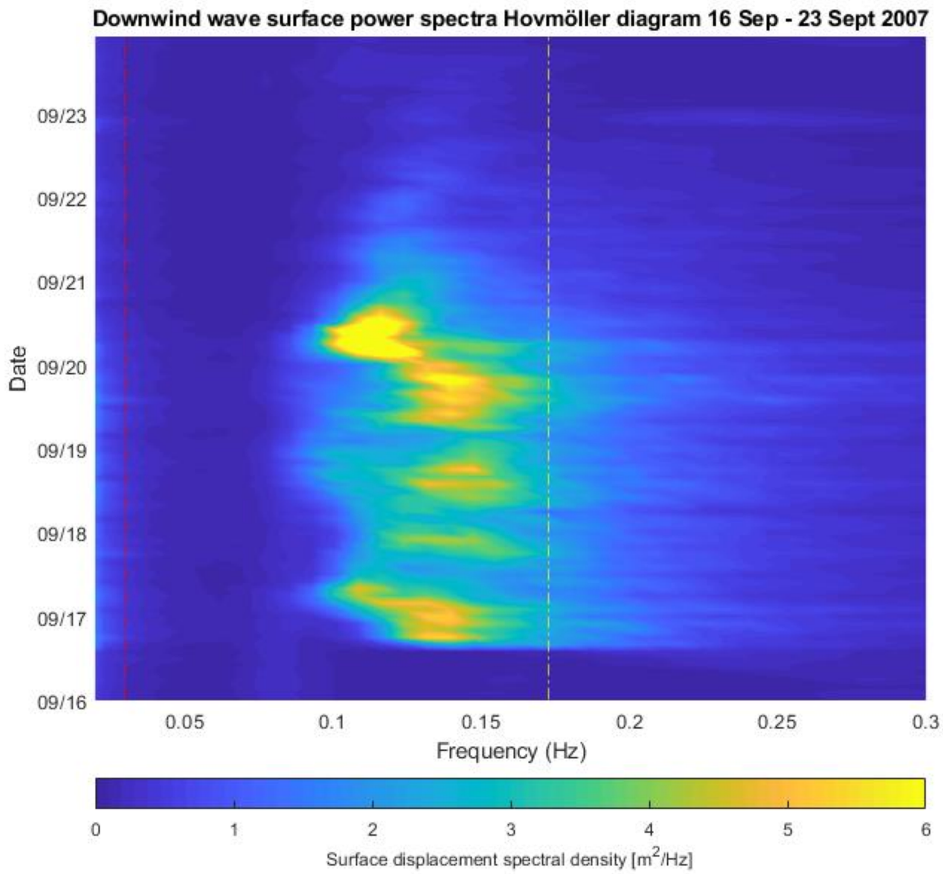


Figure 3.4 Downwind (assumed) wave surface spectra during an LSC event. The dash-dotted lines represent the frequency of transition of waves from shallow (red) and deep (yellow) types to intermediate.

A second set of LSC events from BUP with sessions of interest here ranging from 118 through 121 (August 15 through September 11th, 2008) is analyzed. The instrumentation and processing of the data was the same as described above and are detailed in Savidge and Gargett (2017). In this data set, events were identified using an analysis similar to the event in sessions 17 and 18. During this time, three separate LSC events apparently take place. The first takes place between August 19th and 25th, and the second between August 31st and September 7$^{th}$.

Figure 3.5 depicts the time series records for sessions 118 and 119 corresponding to the first LSC event of this data set. Just as the 2007 event aforementioned, the wind starts blowing in the same direction on the evening of the 20th, followed by an increase of significant wave height peaking on the afternoon of the 21st and plateauing until the afternoon of the 22$^{nd}$ followed by a slow decrease to normal levels on the 25th. Concurrently, the water column becomes more mixed until it gets unstratified on 21st, as the cell reaches the full length of the water column.

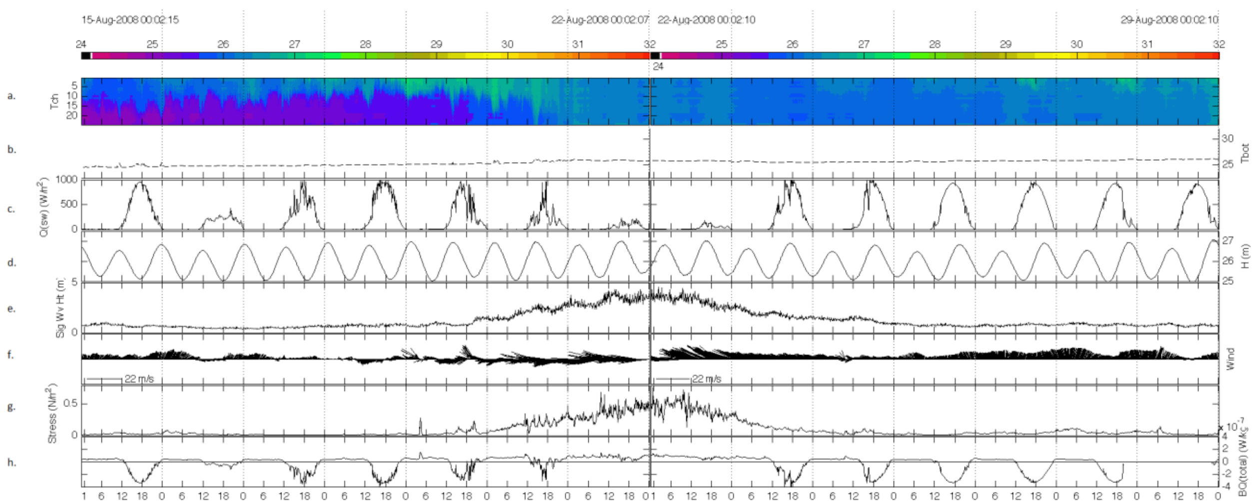


Figure 3.5: High wind and wave event recorded at R2, August 2008. Shown are session 118 (left), and session 119 (right), Water column temperature (Celsius) (a); Temperature of the bottom (Celsius) (b); Shortwave radiation (c); Tide height (d); significant wave height (e); Wind velocity and direction (f); Wind stress (g); Buoyancy flux (W/kg) (h).

The second, smaller, LSC event takes place during sessions 120. Its time series are depicted in Figure 3.6. Before the event takes place, the water is not very stratified as the previous event happened only a few days before. The wind starts blowing in the same direction on the evening of the 31st. The significant wave height increases slightly until it decreases again on the morning of the 3rd when the wind direction changes. During that period the water column is close to unstratified.

A third event takes place between sessions 120 and 121, also shown in Figure 3.6. A strong wind shifts back on the afternoon of the 4th and blows constantly until it changes directions during the evening of the 6th. During that time significant wave height increases, peaking during the 5$^{th}$, and then decreasing as the wind loses strength on the 6$^{th}$, returning to normal levels later that day.

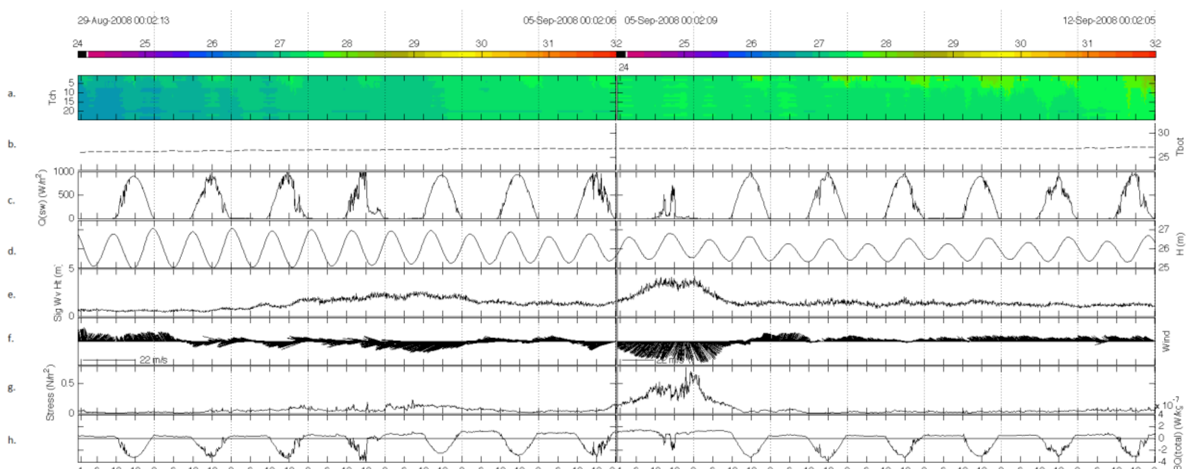


Figure 3.6 High wind and wave event recorded near R2. Shown are session 120 (left), August 2008, and session 121 (right), September 2008, Water column temperature (Celsius) (a); Temperature of the bottom (Celsius) (b); Shortwave radiation (c); Tide height (d); significant wave height (e); Wind velocity and direction (f); Wind stress (g); Buoyancy flux (W/kg) (h).

The resulting downwind displacement spectrum for these sessions was calculated and plotted, as discussed previously. In Figure 3.7 is depicted the events of sessions 118 and 119 coinciding with the time series analysis, with high energy density, followed by a period of low energy with a spike when the second, smaller, event takes place during session 120. The second event occurs at a visibly lower frequency than that of the previously seen events. The energy level decreases until the third event takes place between sessions 120 and 121, when the energy density spikes and appears through a wider range of frequencies.

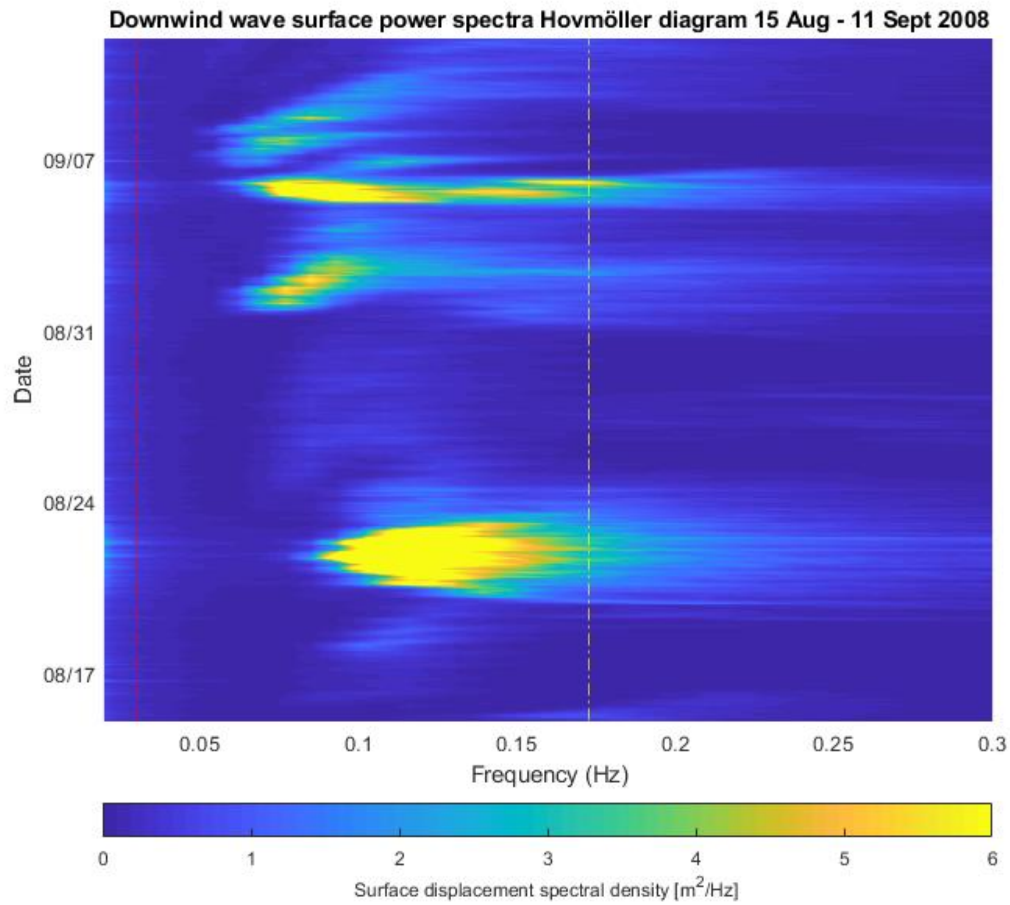


Figure 3.7: Downwind (assumed) wave surface spectra during three LSC events. The dash-dotted lines represent the frequency of transition of waves from shallow (red) and deep (yellow) types to intermediate.

Lastly, a similar dataset was collected for the CSP project in 2015. The data was collected using a 500 KHz Nortek Signature 500 5-beam VADCP, with 4 slant beams 25° from the 5th, vertical beam. All bins are 1 meter in size with the first bin starting at 2.1 meters above bottom. The VADCP was located off the coast of Duck, NC, near Cape Hatteras, in a water column approaching 40 meters.

Distinctly from BUP, there was no auxiliary data from an adjacent meteorological tower. Water column temperature, barometric, meteorological, and wind data were estimated using measurements from nearby NDBC buoys, operated by NOAA. Wave buoy stations in the vicinity of the VADCP, buoys 44014 and 41025 were deemed good candidates for measurements and estimates of meteorological parameters. After examination, data from station 44014 was used for heat flux analysis. Buoy 44014 was located 51 km north of the moorings, situated on the 47 m isobath east of Virginia Beach, VA, and provided temperature data for the air and for water at 1.1 m depth, alongside anemometer, relative humidity, and barometer data.

The VADCP data was divided into 2-hour blocks and 4 Hz was averaged into 1 Hz to match processing for BUP. A processing similar to that of BUP was done, with the exception of the heat flux data. Due to the absence of pyranometer data, the shortwave and longwave radiation were estimated using methods presented in Chapter 4.

The final event presented herein is from the CSP data discussed above. Figure 3.8 depicts the time series data for the session of interest (301), where a LSC event was identified between September 22$^{nd}$, and October 1st, 2015. The water column was heavily stratified (a) for the beginning of the session as strong winds were shown to blow unidirectionally in stations 44014 (f) and 41025 (h). Significant wave height (e) remained relatively constant until the 26$^{th}$ when it started increasing, coinciding with the destratification of the water column, slowing decreasing after the 27$^{th}$, reaching pre-event levels by the end of the session. This decrease is likely due to the weakening of the winds after the 27$^{th}$. The water column remains relatively unstratified until the end of the 30th (b).

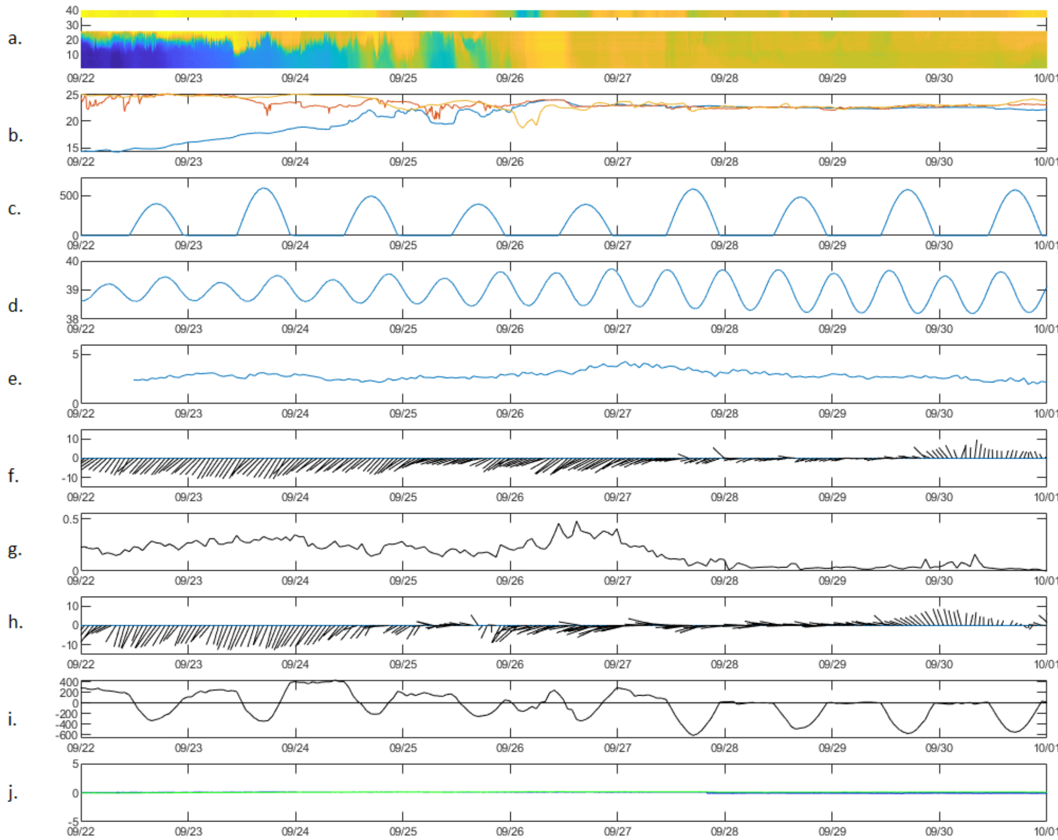


Figure 3.8: High wind and wave event recorded near Cape Hatteras. Shown is session 301, September 2015. Water column temperature (in Celsius) (a); Temperature of surface (yellow), bottom (blue), and average (orange) (in Celsius) (b); Estimated Shortwave radiation (W/m$^2$)(c); Tide height (ft) (d); significant wave height (m) (e); Wind velocity and direction (buoy station 44014)(m/s) (f); Wind stress (buoy station 44014) (N/m$^2$) (g); Wind velocity and direction (buoy station 41025) (m/s)  (h); Total buoyancy flux (W/kg)(i); pitch and roll (deg) (j).

Figure 3.9 depicts the Rayleigh number (proxy for buoyancy forcing), wind surface stress, significant wave height and buoyancy flux for the period of interest. The LSC event is expected when the $\log_{10}(Ra)$ values below 5.5 with a destabilizing buoyancy flux, which is observed between the 27th and 30th.

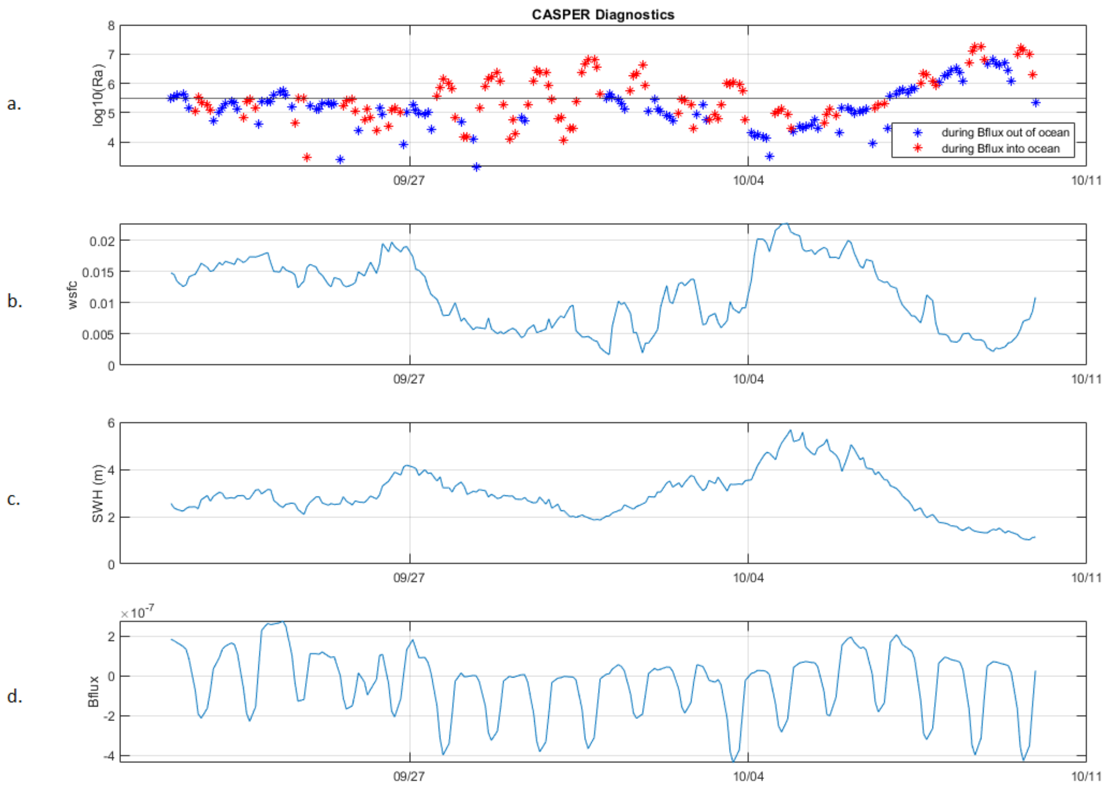


Figure 3.9: Rayleigh number (a); Surface wind stress (N/m$^2$) (b); Significant wave height (m)(c); Buoyancy flux (W/kg) (d).

The resulting downwind displacement spectrum was calculated similar to BUP (Fig. 3.10). The frequencies of transition to intermediate wave type were calculated for a 36 m water column. As expected from the time series analysis, the energy density of the event appears at a relatively higher frequency during the early afternoon of the 26th, when the water column becomes unstratified. The event lasts until the Rayleigh number no longer remains in the expected range for LSC events, on the 30th. Afterwards, the spectral density significantly decreases with the end of the event. Further diagnosis of LSC at this site, such as regime diagram and forcing space are presented in Chapters 5 and 6.

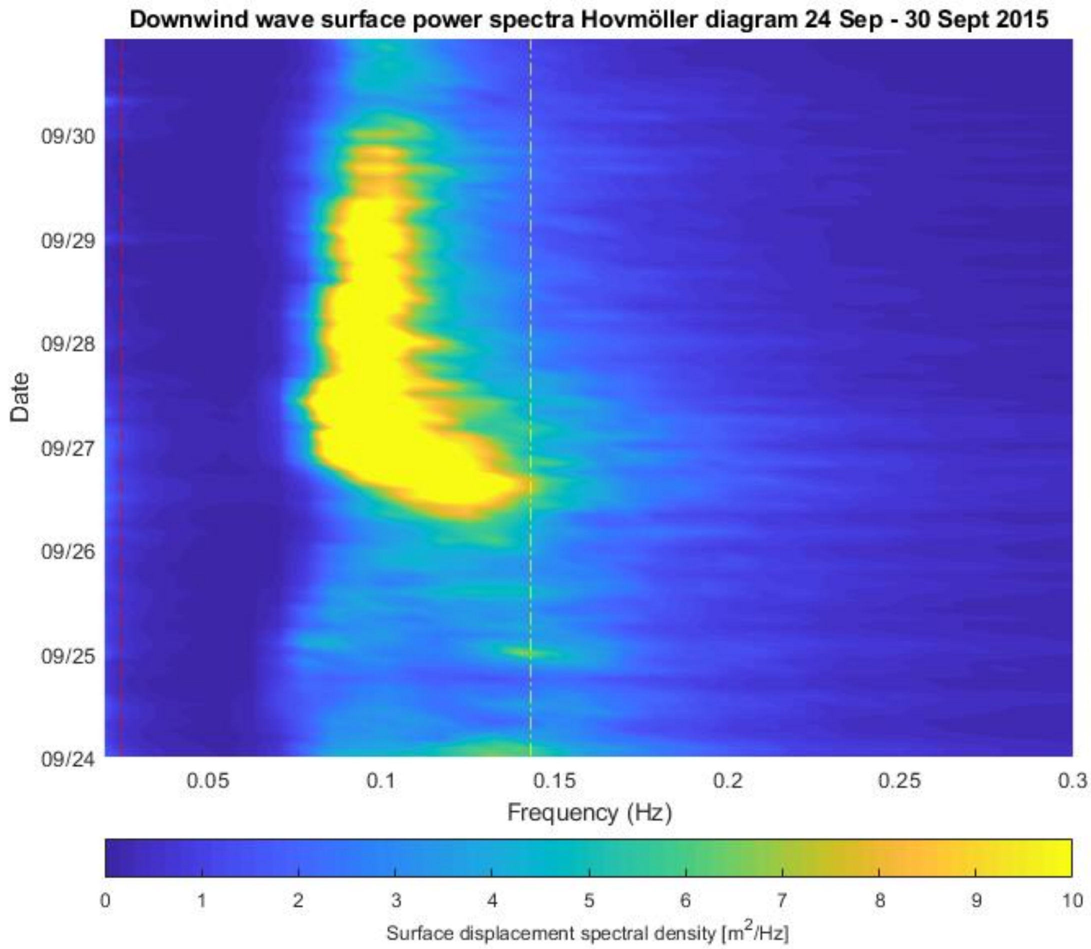


Figure 3.1: Downwind (assumed) wave surface spectra during a LSC event for CSP. The dash-dotted lines represent the frequency of transition of waves from shallow (red) and deep (yellow) types to intermediate.

# CHAPTER 4

## ROTARY SPECTRA TO SEPARATE WAVES AND TURBULENCE

*This chapter is being prepared for the Journal of Atmospheric and Oceanic Technology (De Melo, Woodson, and Savidge).*

### 4.1 INTRODUCTION

Turbulence plays a crucial role in the dynamics of shallow coastal waters, affecting stratification, regulating baroclinic and barotropic shear flows, and profoundly influencing biological processes. A significant challenge in studying these processes is accurately separating the contributions of wave motion and turbulence, as they often overlap in frequency and space. In the context of Langmuir circulations, which arise from the effects of Stokes drift in the surface wave field and manifest as pairs of counterrotating vortices roughly aligned downwind, this separation becomes even more critical.

ADCPs and pointwise velocimeters are commonly employed to collect velocity data for estimating Reynolds stresses. However, challenges arise when wave and turbulence frequency bands overlap, especially since the variance associated with waves is routinely much larger than that of the processes of interest in turbulence investigations. Additionally, misalignment of instrument coordinates relative to true coordinates and the presence of a gently sloping bed can result in wave bias in the vertical velocities significantly affecting Reynolds stress estimates. In coastal oceans, surface waves often produce velocity fluctuations much larger than those associated with turbulence, dominating covariance between vertical and horizontal velocities.

This covariance cannot be fully removed by coordinate rotation if there is uncertainty in the instrument's orientation or the wave-induced velocity field (Trowbridge, 1998).

To address these issues, various techniques for wave-turbulence decomposition have been proposed. Trowbridge (1998) suggested a widely accepted solution using two instruments, where the velocity signal from one instrument is subtracted from that of another nearby instrument. This assumes that wave velocities at the two instruments are equal and cancel out upon subtraction, and that velocity fluctuations due to waves and turbulence are uncorrelated. Building upon this two-instrument technique, Shaw and Trowbridge (2001) and Feddersen and Williams (2007) added a linear filter to predict the wave velocity of one instrument based on the velocity signal of the other.

Single-instrument techniques are of greater interest due to their lower cost and simpler logistics. Bricker and Monismith (2007) proposed a single-instrument technique based on spectral wave decomposition for separating turbulence and wave signals. This "phase" method assumes equilibrium turbulence and no wave-turbulence interaction, interpolating the magnitude of turbulence under the wave peak using the phase lag between downwind and vertical velocity components. However, such techniques struggle to separate wave and turbulence when both share a portion of their frequency range.

In an effort to address the challenges of wave-turbulence decomposition using single-instrument techniques, Kirincich and Rosman (2011) proposed a method that leverages the characteristics of ADCP measurements. Their approach utilizes a comparison of methods for estimating Reynolds stress from ADCP measurements in wavy environments, focusing on the removal of wave contamination in these measurements. By carefully considering the wave-induced components in the ADCP data, their method provides a more accurate estimation of Reynolds stress, contributing to the overall understanding of turbulence in the coastal ocean.

Data from five beam ADCPs that provide high quality vertical velocity suggests that estimates of rotary spectra in a vertical plane may provide a useful avenue for identifying the wave induced component in high temporal resolution velocity measurements. Such analysis could address the issue of shared frequency ranges by decomposing velocity time series into counter-rotating components. The approach exploits the unique features of waves, which follow elliptical trajectories with decreasing amplitude as depth increases, i.e., wave orbitals correlate with depth, whereas turbulence should be uncorrelated. This characteristic of waves manifests in a rotary spectrum as high-energy peaks at the same frequency, decreasing with depth.

ADCPs record velocities in bins at different depths, and for each bin, a rotary spectrum reveals high-energy levels at the same frequency decreasing with depth due to the wave's elliptical trajectory. When waves transition from deep to intermediate type in the coastal ocean, the wave portion of the rotary spectra appears at all depths. Correlation between time series from bins at various depths appears in a rotary spectrum, high at frequencies affected by wave motion and near zero at other frequencies. By subtracting the correlated portion of the rotary spectra from the time series, the effects of the wave in the flow can be removed.

## 4.2 METHODOLOGY

I follow the methodology of Mooers (1973) and Appendix 3 of Pugh (1996) to estimate rotary components of time series, to calculate rotary spectra, and find the correlation between rotary spectra of distinct time series.

**Rotary components of a time series velocity**

A vector time series such as current or wind velocity data is often decomposed into Cartesian coordinates. Suppose *u*(*t*) and *v*(*t*) are continuous, stationary, stochastic processes with zero mean values which can be represented by Fourier integrals as follows:

$$u(t) = \frac{1}{2\pi}\int_0^{\infty}[B_1(\omega)\cos(\omega t) + B_2(\omega)\sin(\omega t)]d\omega = \frac{1}{2\pi}\int_{-\infty}^{\infty} U(\omega)e^{i\omega t}d\omega, \tag{4.1}$$

where:

$$U(\omega) = \begin{cases} \frac{1}{2}[B_1(\omega) - iB_2(\omega)], \omega \geq 0 \\ \frac{1}{2}[B_1(\omega) + iB_2(\omega)], \omega \leq 0 \end{cases} = \int_{-\infty}^{\infty} u(t)e^{-i\omega t}\, dt, \tag{4.2}$$

and

$$v(t) = \frac{1}{2\pi}\int_0^{\infty}[B_3(\omega)\cos(\omega t) + B_4(\omega)\sin(\omega t)]d\omega = \frac{1}{2\pi}\int_{-\infty}^{\infty} V(\omega)e^{i\omega t}d\omega, \tag{4.3}$$

where:

$$V(\omega) = \begin{cases} \frac{1}{2}[B_3(\omega) - iB_4(\omega)], \omega \geq 0 \\ \frac{1}{2}[B_3(\omega) + iB_4(\omega)], \omega \leq 0 \end{cases} = \int_{-\infty}^{\infty} v(t)e^{-i\omega t}\, dt, \tag{4.4}$$

Coefficients $B_1, B_2, B_3, B_4$ can be generalized as real-valued variables *A*, *C*, $\phi$, and $\theta$ where *A* and *C* are non-negative and $\phi$, and $\theta$ are values equal or between 0 and $2\pi$ radians:

$$B_1 = Acos\phi + Ccos\theta, \tag{4.5}$$

$$B_2 = -Asin\phi - Csin\theta, \tag{4.6}$$

$$B_3 = Asin\phi - Csin\theta, \text{ and} \tag{4.7}$$

$$B_4 = Acos\phi - Ccos\theta, \tag{4.8}$$

where:

$$A = \frac{1}{2}[(B_4 + B_1)^2 + (B_3 - B_2)^2]^{1/2}, \tag{4.9}$$

and

$$C = \frac{1}{2}\left[(B_4 - B_1)^2 + (B_3 + B_2)^2\right]^{1/2}, \qquad (4.10)$$

$$tan\ \theta = \left(\frac{B_3+B_2}{B_4-B_1}\right), \qquad (4.11)$$

and

$$tan\ \phi = \left(\frac{B_3-B_2}{B_4+B_1}\right), \qquad (4.12)$$

Allowing us to write *u*(*t*) and *v*(*t*) in the following form:

$$u(t) = \frac{1}{2\pi}\int_0^\infty [A\cos(\omega t + \phi) + C\cos(\omega t + \theta)]d\omega, \qquad (4.13)$$

and

$$v(t) = \frac{1}{2\pi}\int_0^\infty [A\sin(\omega t + \phi) - C\sin(\omega t + \theta)]d\omega, \qquad (4.14)$$

A and C correspond to the amplitude, and $\phi$ and $\theta$ correspond to the phase of the counterclockwise and clockwise components of motion respectively. The above terms describe an elliptical trajectory in a hodograph for each value of angular frequency, $\omega$, with major axis equal to $|A+C|$ and minor axis equal to $|A-C|$.

As a consequence of this change of variables:

$$U(\omega) = \begin{cases} \frac{1}{2}\left[Ae^{i\phi} + Ce^{i\theta}\right], \omega \geq 0 \\ \frac{1}{2}\left[Ae^{-i\phi} + Ce^{-i\theta}\right], \omega \leq 0 \end{cases}, \qquad (4.15)$$

and

$$V(\omega) = \begin{cases} \frac{-i}{2}\left[Ae^{i\phi} - Ce^{i\theta}\right], \omega \geq 0 \\ \frac{i}{2}\left[Ae^{-i\phi} - Ce^{-i\theta}\right], \omega \leq 0 \end{cases}, \qquad (4.16)$$

$u(t)$ and $v(t)$ can be written as a complex horizontal velocity time series:

$$w(t) = u(t) + iv(t) = \frac{1}{2\pi}\int_{-\infty}^{\infty}[U + iV]\,e^{i\omega t}d\omega = \frac{1}{2\pi}\int_{-\infty}^{\infty}[W]\,e^{i\omega t}d\omega, \qquad (4.17)$$

where:

$$W(\omega) = \begin{cases} \frac{1}{2}\left[Ae^{i\phi}\right], \omega \geq 0 \\ \frac{1}{2}\left[Ce^{-i\theta}\right], \omega \leq 0 \end{cases} = \int_{-\infty}^{\infty} w(t)e^{-i\omega t}dt, \tag{4.18}$$

Due to the counterrotating nature of the rotary components of the velocity time series $w(t)$, sometimes the clockwise components and counterclockwise components will act in an additive way when they point at the same direction, and sometimes they will act in a subtractive way when they point in opposite directions. Thus, circular wave orbitals would have only one non-zero rotary component at a given frequency, whereas elliptical orbits would have both non-zero rotary components.

**Rotary spectra and coherency**

Assume now two velocity time series $w_1(t) = u_1(t) + iv_1(t)$ and $w_2(t) = u_2(t) + iv_2(t)$, each can be decomposed into its rotary components, and their one-sided cross spectra can be estimated as:

$$G_{u_j v_k}(\omega) = \left[C_{u_j v_k}(\omega) - iQ_{u_j v_k}(\omega)\right], (j = 1,2) , \tag{4.19}$$

where the real part of $G_{u_j v_k}(\omega)$, $C_{u_j v_k}(\omega)$, is the cospectrum and the imaginary part, $Q_{u_j v_k}(\omega)$, is the quadrature spectrum.

The two-sided rotary inner-cross spectrum can be estimated using cross spectra components as:

$$S_{w_j w_k}(\omega) = \frac{1}{2}\left[(C_{u_j u_k} + C_{v_j v_k}) + (Q_{u_j v_k} - Q_{v_j u_k})\right] + \frac{i}{2}\left[(C_{u_j v_k} - C_{v_j u_k}) - (Q_{u_j u_k} + Q_{v_j v_k})\right], (j,k = 1,2) , \tag{4.20}$$

with inner-autospectrum:

$$S_{w_j w_j}(\omega) = \frac{1}{2}\left[C_{u_j u_j} + C_{v_j v_j} + Q_{u_j v_j}\right], (j = 1,2)\ , \tag{4.21}$$

The two-sided inner-coherence squared, $\gamma_{12}^2(\omega)$ , is defined for $w_1$and $w_2$ as:

$$\gamma_{12}^2(\omega) = \frac{-Im(S_{w_1 w_2})}{Re(S_{w_1 w_2})}, \tag{4.22}$$

**Removing correlated parts**

The wave bias can be diminished by removing the correlated part of the rotary spectra from the velocity fluctuation measurements from two different bins. If the distance between the bins is sufficiently large compared to the correlated scale of turbulence and sufficiently small relative to the inverse wavenumber of surface waves, the correlation between the top and bottom bins in the rotary spectra will be solely due to wave effects.

This analysis is based on a set of assumptions similar to those of Trowbridge (1998). The key is that there is no correlation between turbulent velocity fluctuations with depth but wave-induced fluctuations correlate at varying depths, i.e., removing corelated parts removes waves but not turbulence. This assumption may not hold near surface under wave-breaking, as turbulence correlated with wave motion would occur. Other assumptions include that wave and turbulent fluctuations are statistically ergodic, stationary, that waves are weakly nonlinear, and narrow-banded in frequency and direction (which is the case for most LSC, since it requires that the wind blows in the same direction for a significant amount of time resulting in waves roughly aligned with the wind, such as the case for BUP and CSP, Chapter 3).

If the assumptions hold, the two-sided inner-coherence squared of the two-sided rotary inner-cross spectrum of two bins at different height is a result of rotary correlation at each frequency, which upon removal by multiplying its complement to each of the bin's rotary spectra, would result in removal of wave-induced fluctuations while preserving uncorrelated turbulent fluctuations.

**Dataset**

The method above will be applied to different datasets with mixed turbulence and wave effects. Parts of the rotary spectra at points at different depths that are correlated are removed from data to leave only non-wave velocity fluctuations. For this analysis, three data sets are examined.

The first consists of simulated data of two-dimensional wave-like motion with added random noise at all frequencies. The wave motion was simulated to generate horizontal and vertical motion, respectively, for surface waves derived by applying wave equation at a single frequency to the Laplace equation for irrotational flow:

$$u = \left(\frac{\pi H}{T}\right) \frac{\cosh\left[2\pi \frac{(z+h)}{L}\right]}{\sinh\left[2\pi \frac{(z+h)}{L}\right]} \left[cos 2\pi \left(\frac{x}{L} - \frac{t}{T}\right)\right], \tag{4.23}$$

and

$$w = \left(\frac{\pi H}{T}\right) \frac{\sinh\left[2\pi \frac{(z+h)}{L}\right]}{\sinh\left[2\pi \frac{(z+h)}{L}\right]} \left[sin 2\pi \left(\frac{x}{L} - \frac{t}{T}\right)\right], \tag{4.24}$$

where T is the wave period, H is the wave height, L is the wavelength, z is the depth, t is the time, h is the water depth, with wave frequency $\omega = \left(\frac{2\pi}{T}\right)$.

Then, random noise scaled within an arbitrary amplitude large enough to appear in the spectral analysis and small enough not to override the effects of waves, was added at all frequencies. This simple wave simulation allows for the following hypothesis: Rotary spectra for simulated data at any two bins (different depths) will peak at frequency $\omega$, and that the resulting two-sided inner-coherence squared will have maximum correlation at that same frequency. Upon removal of the correlated parts, only uncorrelated noise will remain.

The second dataset consists of ADCP data from BUP session 017 (Chapter 3), where in the appendix of Savidge and Gargett (2017), a gap in the frequency range of waves and turbulence has been found between 0.02 and 0.1 Hz. This analysis would allow for validation of the rotary spectra method against published data by checking if it would be able to successfully remove the wave portion (after 0.1 Hz), while maintaining lower-frequency fluctuations (below 0.02 Hz). For this analysis, velocity measurements were decomposed and rotated into downwind and crosswind coordinates.

Lastly, this method is tested against data from CSP session 301 (chapter 3) which present LSC events, of particular interest is the LSC of September 26$^{th}$, which begun after winds maintained stagnant direction for a significant period of time, resulting in close alignment between waves and wind. Analogous to the procedure for the BUP dataset, velocities were rotated into a wind aligned coordinate system.

## 4.3 RESULTS AND DISCUSSION

For the simulated dataset, the elliptical motions of a higher and lower bins are shown (Fig. 4.1).

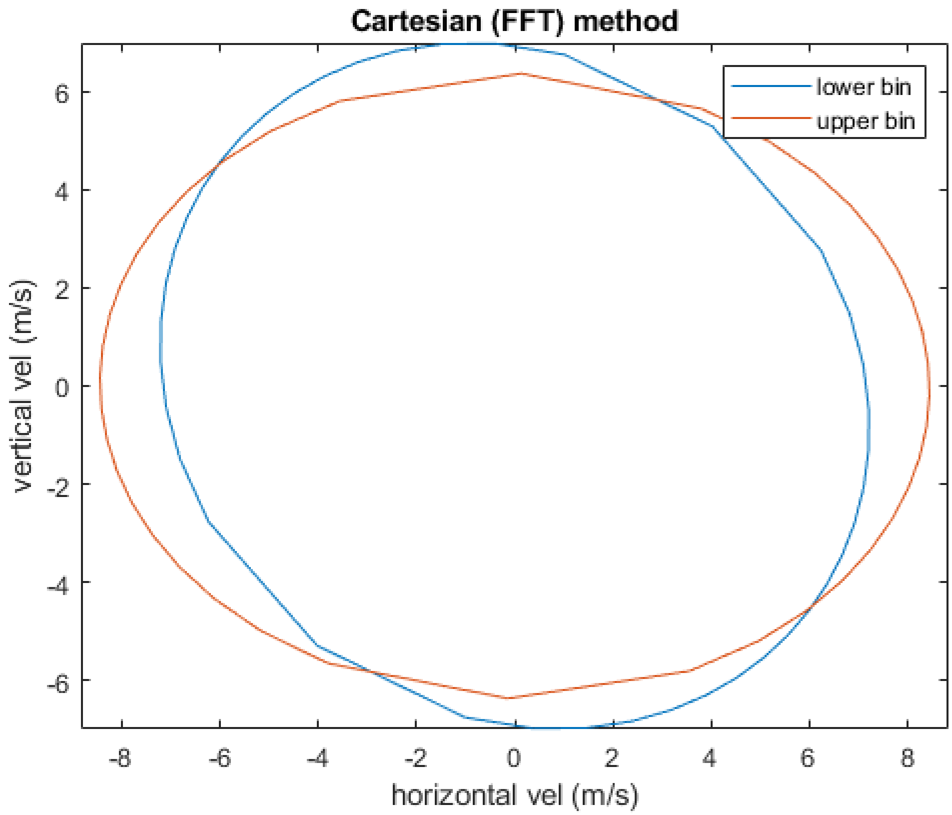


Figure 4.1: Elliptical trajectory of simulated water particles at different depths (1-meter apart) under the effects of wave motion with added noise.

Due to the nature of wave motion, the elliptical trajectories of the fluid will resemble a circle when waves are deep and will be more elliptical with decrease in depth once the waves become of intermediate type. For the case of simulated deep wave data, circles are expected with small eccentricity at different points due to added noise scaling to the amplitude of the wave (Fig. 4.1).

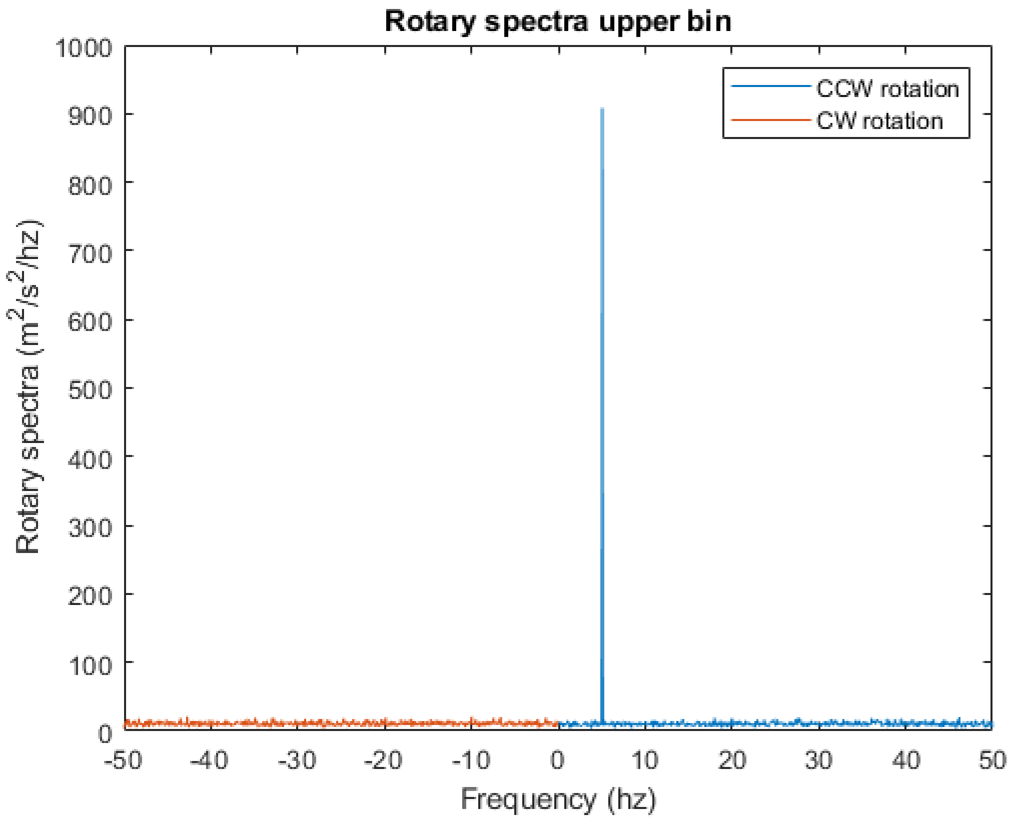


Figure 4.2: Rotary spectrum for top bin of simulated dataset.

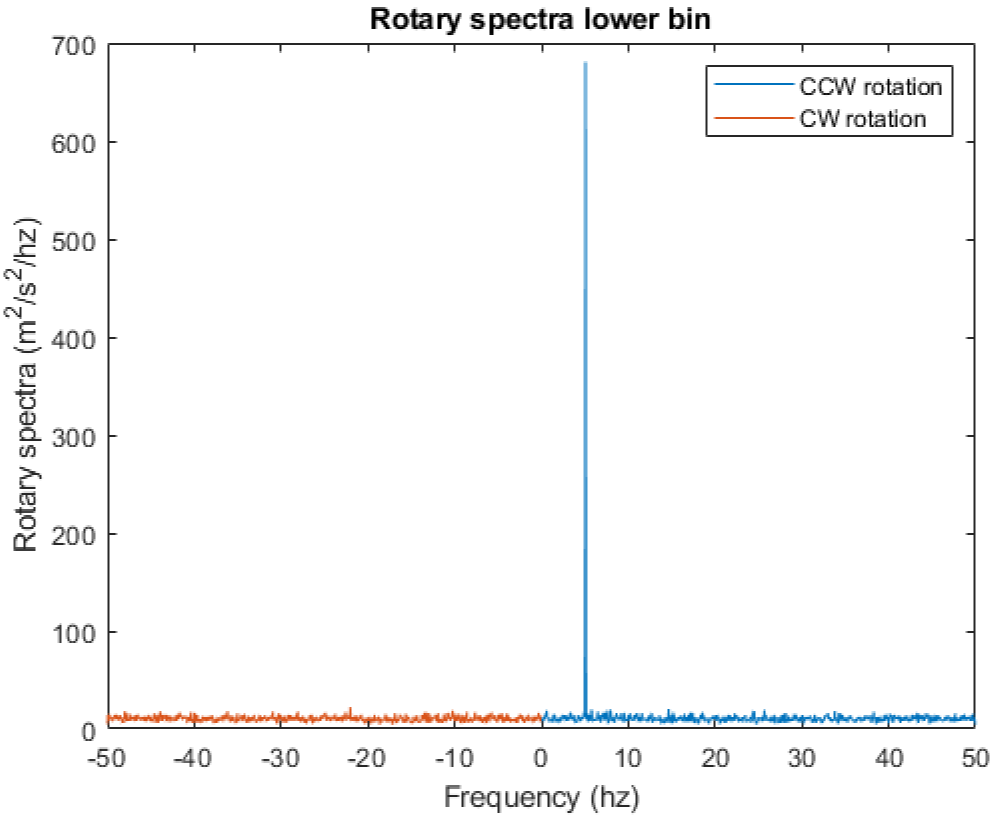


Figure 4.3: Rotary spectrum for bottom bin of simulated dataset.

The rotary spectra of the simulated dataset (Fig. 4.2 and 4.3) for the top and bottom bins reveal small fluctuations occurring at all frequencies, and a clear peak in energy for both bins at around 5 Hz, and only in the counterclockwise direction, which matches the proposed hypothesis. The higher peak at the wave frequency of the higher simulated bin is expected due to the decrease in amplitude of the wave relative to depth.

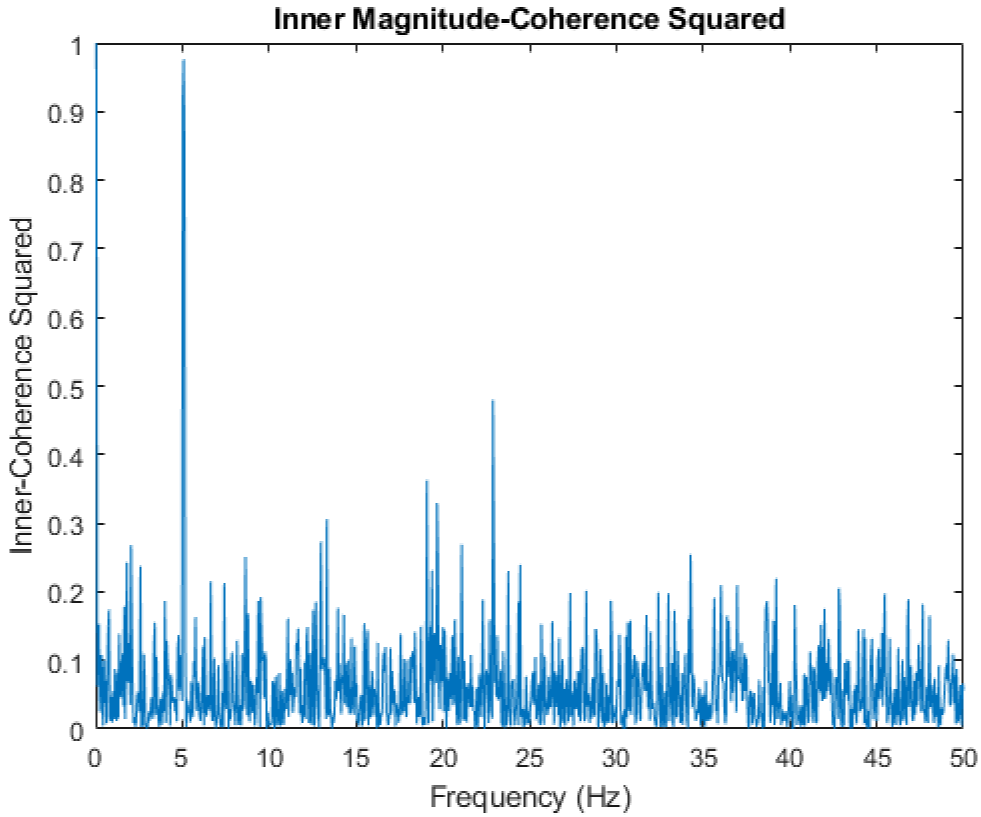


Figure 4.4: Rotary inner-coherence squared between top and bottom bins for simulated dataset.

Inner-coherence squared between the bins rotary spectra reveal peak correlation near 1 (100%) at 5 Hz (Fig. 4.4), which matches frequency of the simulated waves. Surprisingly, correlation at other frequencies due to noise are not zero, though small compared to that at the simulated wave frequency. This is likely due to a small inaccuracy in the method used to implement noise, which added positive bias in *u* and *w*, resulting in mean positive noise, rather than zero.

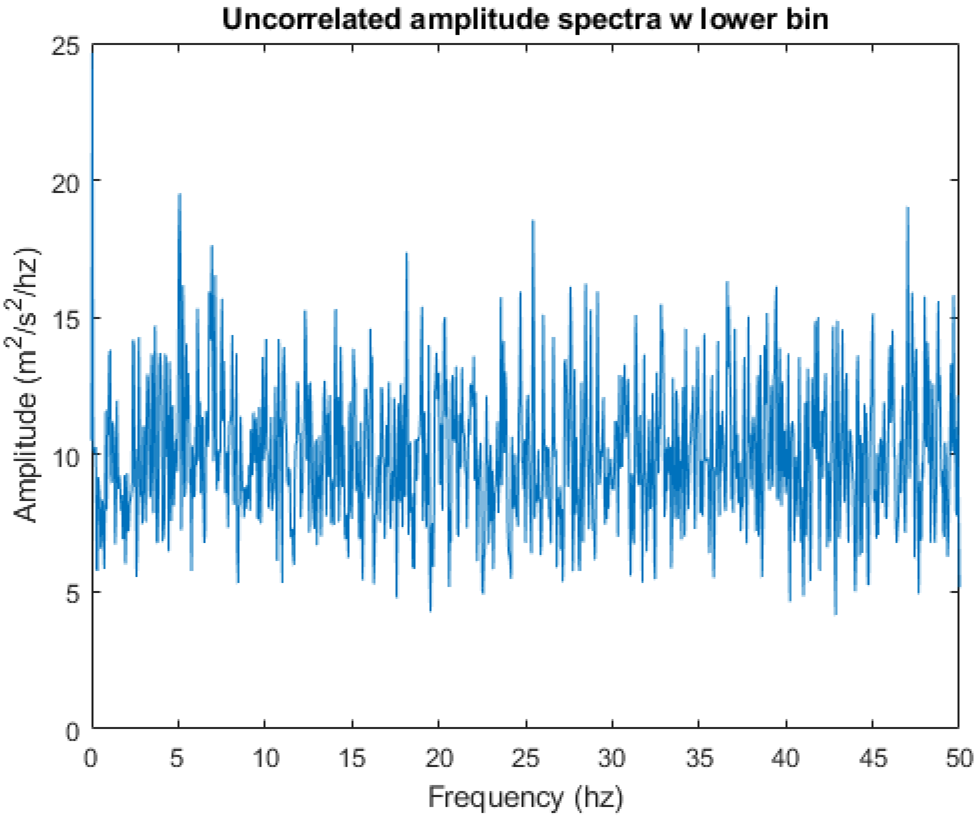


Figure 4.5: Auto-spectrum of lower bin after correlated rotary parts are removed.

The correlated portions of the data are removed from data to eliminate effects from wave, leaving behind only random noise (Fig. 4.5). The method worked as intended with the caveat that positive bias in the application of noise as discussed previously resulted in slight correlation of random fluctuations.

Real ADCP data, however, is often more complex and can have contributions from waves with multiple periods. In order to validate this method, I examine the BUP 017 dataset which was assessed to have a gap between the frequency range of turbulence and the frequency range of waves.

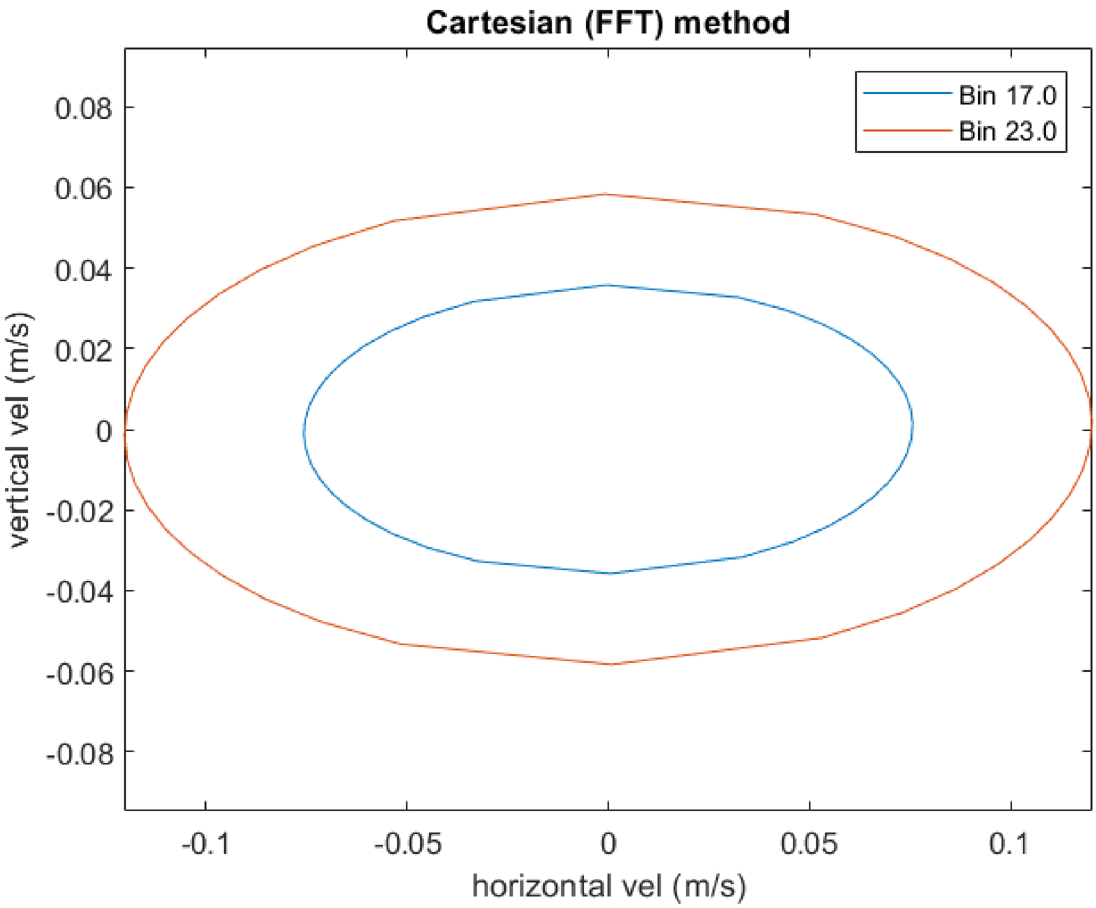


Figure 4.6: Elliptical trajectory of BUP session 017 2-hour block for bins 17 and 23 during a Langmuir Supercell event.

As a requirement for LSC, waves of intermediate type during the 2-hour block occurred, resulting in the elliptical trajectories shown in Figure 4.6, rather than circular motion associated with deep waves, due to the wave being able to feel and interact with the bottom boundary layer. Bin 23, the one closer to the surface, appeared with a higher amplitude of horizontal and vertical motion.

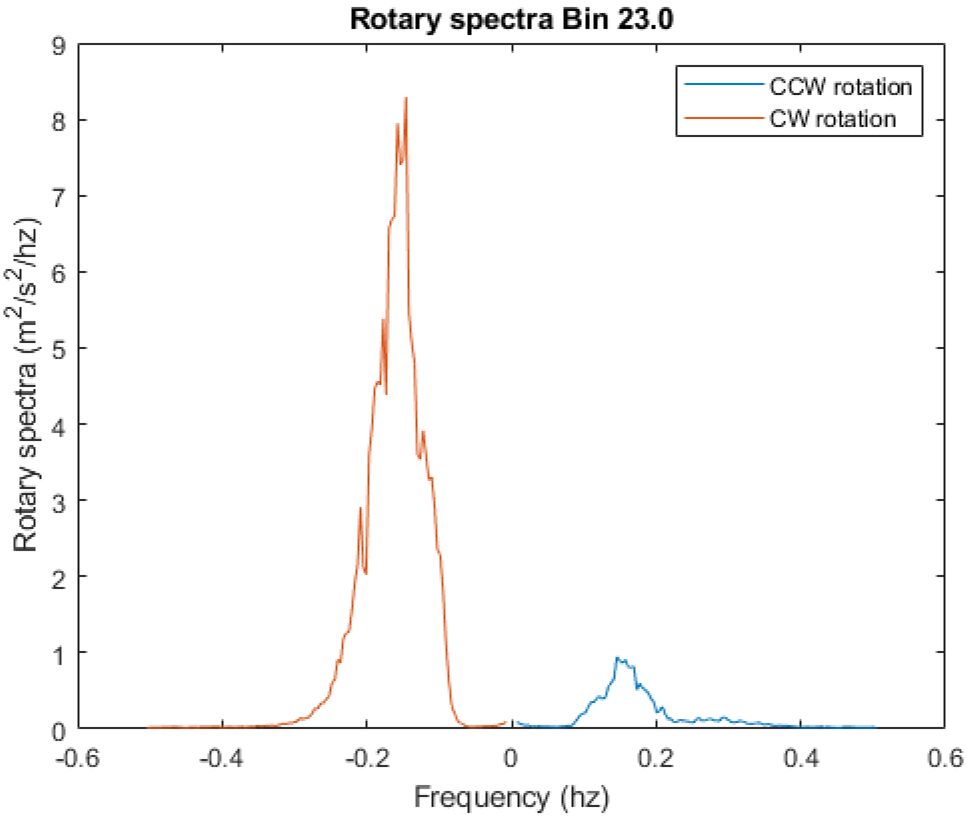


Figure 4.7: Rotary spectrum for top bin BUP 023.

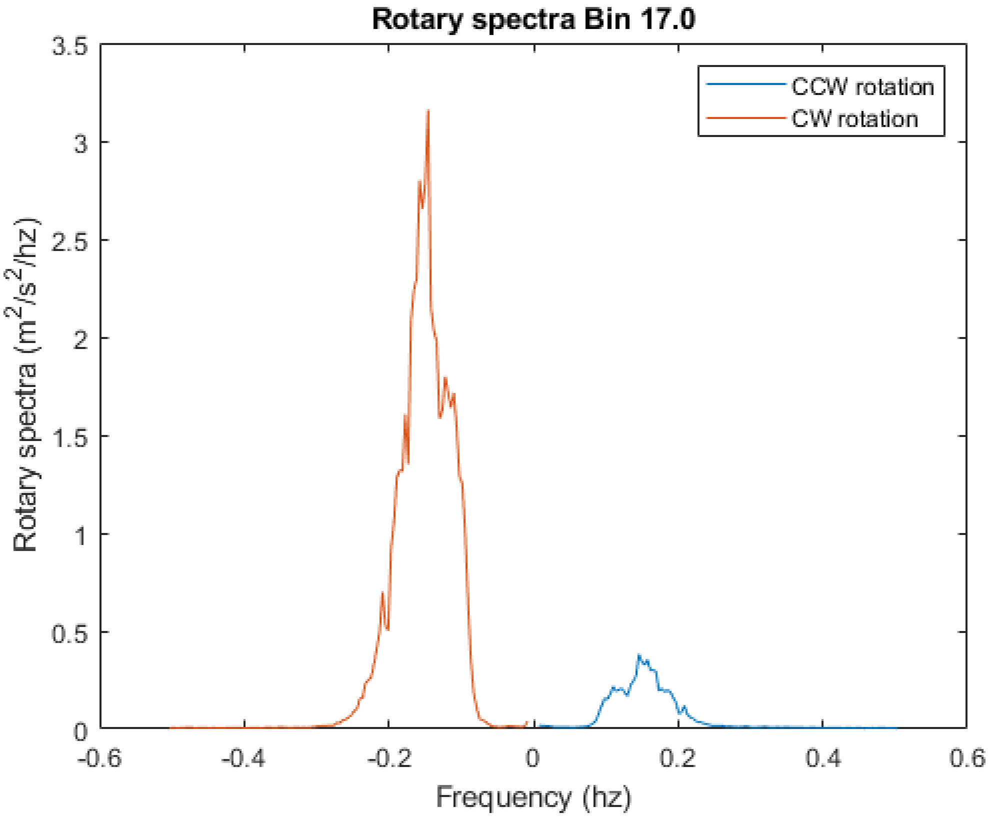


Figure 4.8: Rotary spectrum for bottom bin BUP 017.

Figures 4.7 and 4.8 depict rotary spectra for bins 23 and 17 of BUP 017, respectively. Peaks in rotary spectra occur around 0.2 Hz, mostly in the clockwise direction, with the main difference between bins being the amplitude of the peaks. Rotary amplitude occurring in the counterclockwise and clockwise direction are due to elliptical nature of waves of intermediate type.

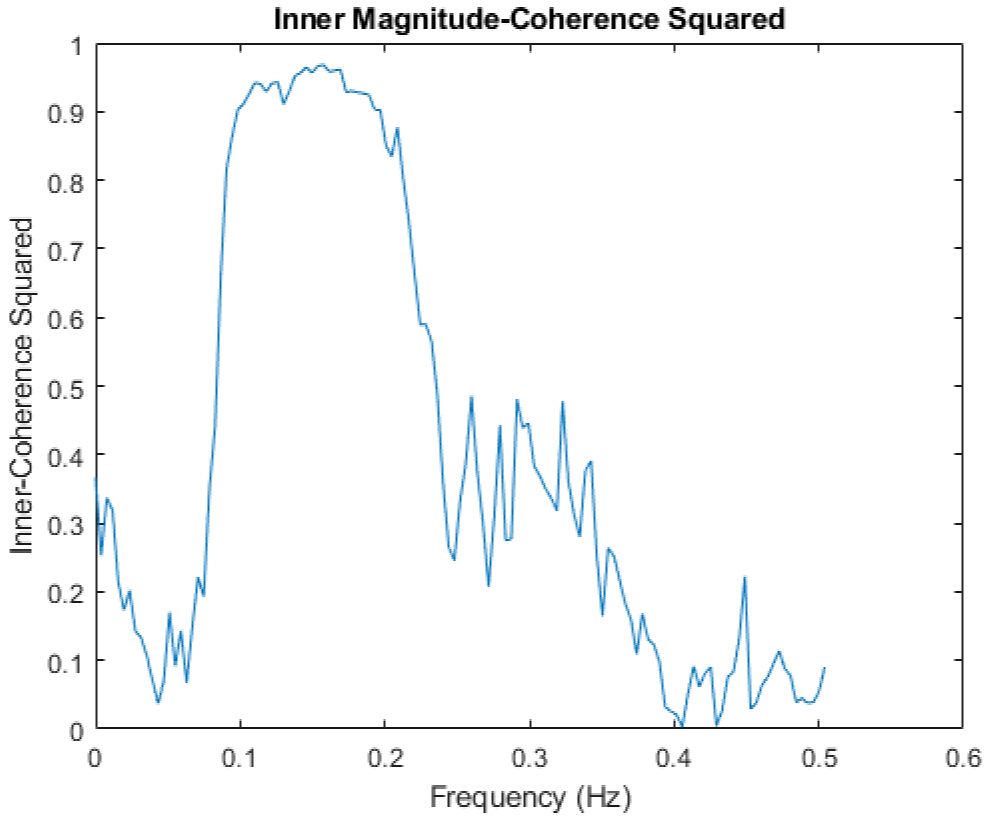


Figure 4.9: Rotary inner-coherency squared between top and bottom bins for BUP session 017 2-hour block.

Inner-coherency squared between the rotary components of the bins peaks between 0.1 and 0.2 Hz, the same range waves are expected to dominate. Coherency squared values reach values above 0.95, but never quite 1 (Fig. 4.9), potentially due to the small misalignment of wind and intermediate waves, especially.

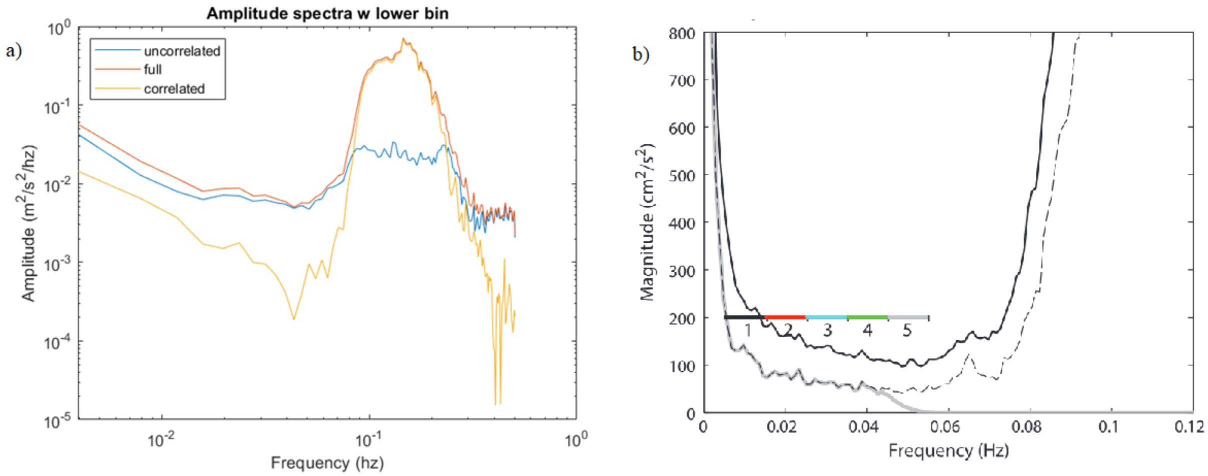


Figure 4.10: a) Full (red), correlated (yellow), and uncorrelated (blue) auto-spectra portions of BUP session 017 lower bin (17), and b) auto-spectra for downwind velocity for bin 3 (Savidge and Gargett, 2017).

The gap between turbulence and wave portions can be clearly seen in Figure 4.10. The wave portion of the dataset set has been reduced drastically, but not fully, after the gap (> 0.1 Hz). This is due to correlation at these frequencies being close to but not quite 1.

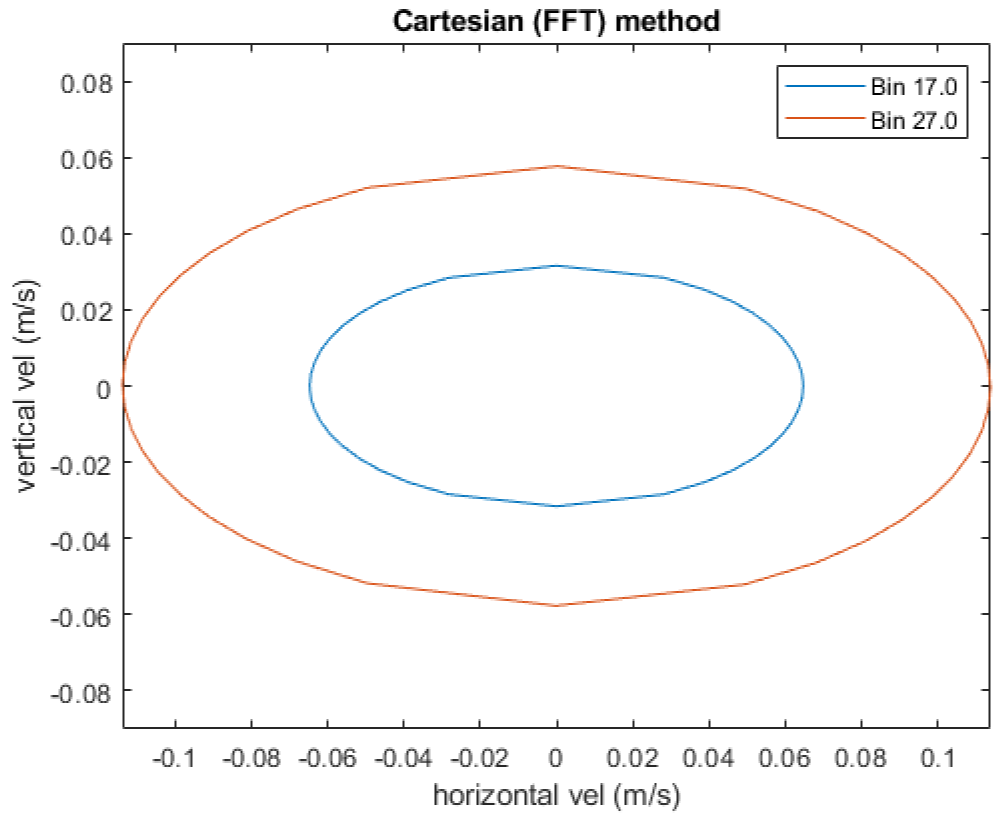


Figure 4.11: Elliptical trajectory of CSP session 301 2-hour block for bins 17 and 27.

For CSP 301, due to waves being of intermediate type after onset of LSC event, the trajectories of the fluid motion follow an elliptical motion (Fig. 4.11) as in BUP 017, with bin 27 presenting larger amplitude of motion due to being higher in the water column compared to bin 17.

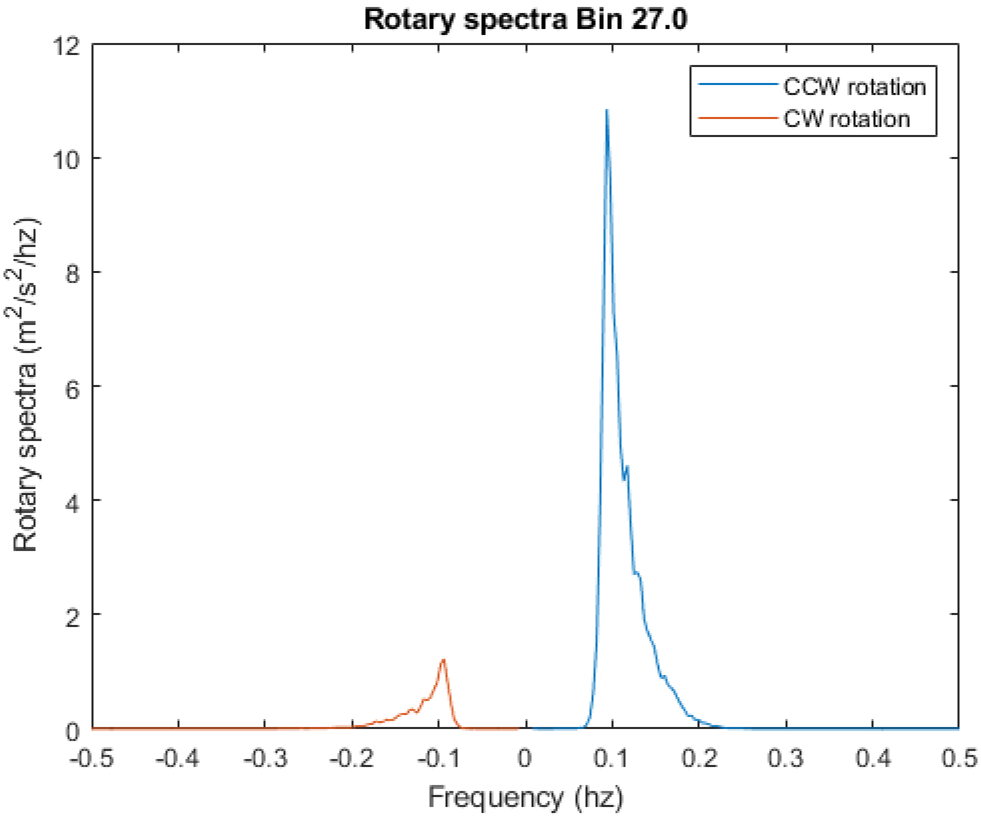


Figure 4.12: Rotary spectrum for top bin CSP session 301.

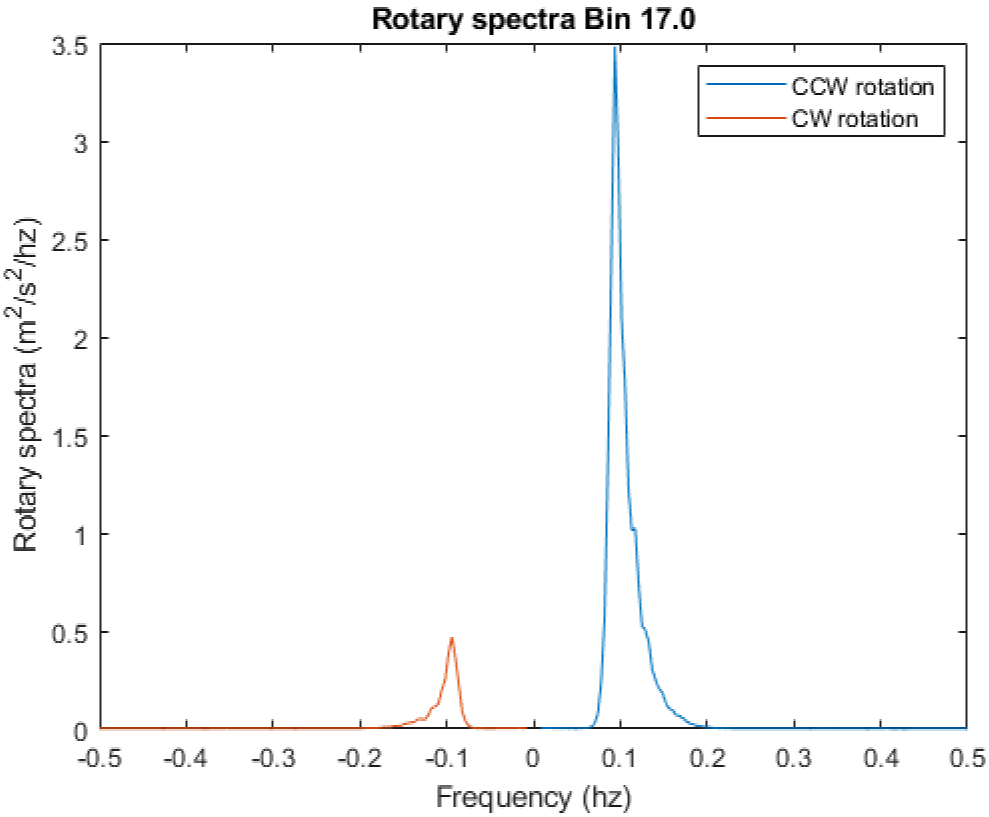


Figure 4.13: Rotary spectrum for bottom bin CSP session 301.

Similar to the observations in the BUP dataset, the peak rotary spectral amplitude for both top and bottom bins occur between 0.1 and 0.2 Hz, with a substantially higher peak at 0.1 Hz in the counterclockwise direction. This peak in amplitude is likely a result of wave motion

(Fig. 4.12 and 4.13), however, peaks in both clockwise and clockwise directions imply that orbits are elliptical rather than circular, as seen in Figure 4.11.

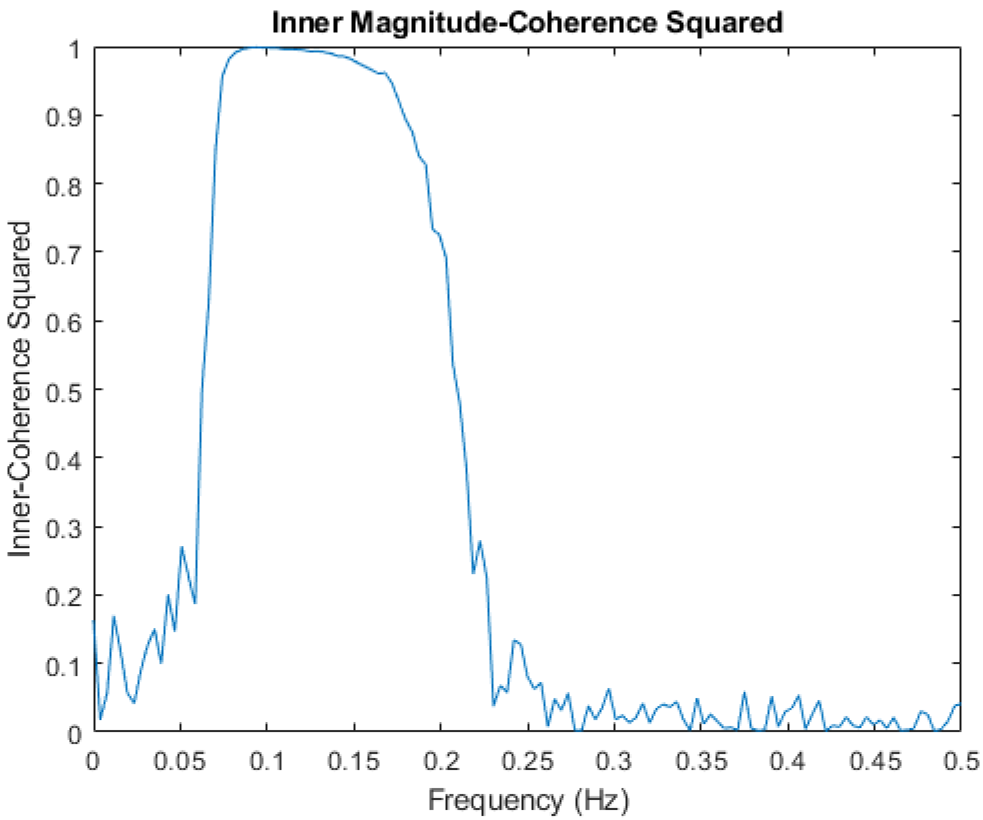


Figure 4.14: Rotary inner-coherency squared between top and bottom bins for CSP session 301 2-hour block.

The inner-coherency squared peaks at 0.1 Hz with a value of 1 (Fig. 4.14), signifying that all energy in the spectra at this frequency is attributable to wave effects. By removing this correlated portion of the spectra from the dataset, it becomes possible to separate wave effects from other fluctuations (Fig. 4.15).

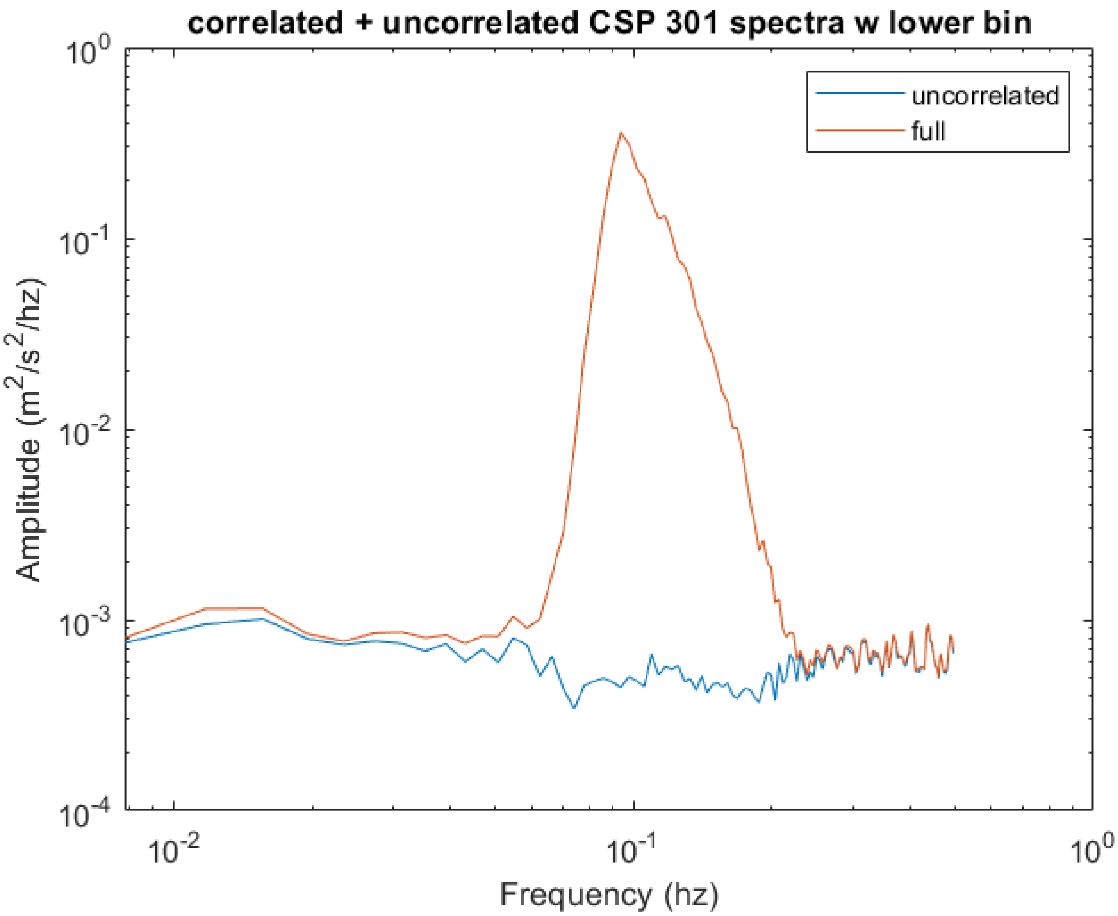


Figure 4.15: Amplitude spectra of top bin for CSP session 301: Full (correlated + uncorrelated) amplitude spectrum (orange), and uncorrelated amplitude spectrum (blue).

## 4.4 CONCLUSION AND FUTURE WORK

The rotary spectra method for separating contributions from wave motion and other velocity fluctuations presents a promising alternative to existing wave separation techniques. While the method demonstrated effectiveness for simulated data and the CSP dataset, it did a reasonable job with the BUP dataset, though waves were not fully removed, which is likely due to wind and waves being slightly misaligned. Although rotary correlation at the wave parts exceeded 95%, the energy amplitude was so substantial that even after a 95% reduction, it remained comparable to the amplitude of low-frequency variability.

For BUP 017, a frequency gap between waves and low-frequency variability occurred between 0.02 and 0.1 Hz, as reported in Savidge and Gargett (2017). Although the rotary spectra method identified the same gap, the approach used in Savidge and Gargett—employing a low-pass filter to eliminate all wave effects—outperformed the rotary spectra method. However, the low-pass filter is only viable when waves and other fluctuations do not share any frequency range, in which case the rotary spectra method would be preferable.

A limitation of the rotary spectra method is its inability to entirely remove wave effects if, due to the beams not measuring fluctuations at the same point, the wave portion of the dataset at different depths does not fully correlate. Furthermore, if the distance between bins is insufficient, the same large-scale vortices may impact both bins, causing the turbulent fluctuations to have non-zero correlation, which would be partially removed along with the effects of waves.

## CHAPTER 5

## A METHOD FOR ESTIMATING HEAT FLUX OVER THE OCEAN USING COMMONLY AVAILABLE DATA

*This chapter is being prepared for the Journal of Geophysical Research - Oceans (De Melo, Woodson, and Savidge).*


### ABSTRACT

Langmuir Supercells (LSC) can exert a profound influence on sediment transport on shallow shelves. Methods to identify occurrence of LSC include buoyancy and convection forcing parametrization. Pyranometry is often used to estimate shortwave and longwave heat fluxes necessary to estimate such forcing. In this article I present an alternative method to estimate radiation using satellite SST imagery and meteorological data from NDBC buoys and towers without the need for a pyranometer, which would be useful to evaluate whether LSC could potentially exist at deeper sites, without direct confirmation from a locally mounted, well-leveled VADCP and co-located pyranometers. The Estimates from Commonly Available Data (ECAD) method to estimate longwave and shortwave radiation proved comparable to the traditional use of pyranometers when utilized to assess forcing compatibility with LSC dominance over other processes. This successful method assists in establishing LSC occurrence at a 40-m depth site, corroborated in-situ by measurements with a well-leveled VADCP.


### 5.1 INTRODUCTION

Wind speeds greater than 3 m/s steadily blowing in a single direction over a large body of water such as a lake or the ocean generate shear over the water surface and upon interaction with the wave field, Langmuir circulations (LC) may manifest. LC consist of pairs of counter-rotating vortices roughly aligned with the wind. The wind-wave interaction involves the Stokes drift velocity induced by surface gravity waves acting with the wind-driven shear current. Historically, LC have been observed within the upper mixed layer of open oceans and large lakes with their depth limited by the thermocline. However, Gargett et al. (2004) and Gargett and Wells (2007) reported measurements of Langmuir cells in the coastal ocean that encompassed the full water column in 15 m depth at the LEO-15 observatory off the New Jersey shelf (LEO). Such full depth structures, coined Langmuir Supercells (LSC), were able to capture and resuspend sediment from the bottom boundary layer. When not limited to the upper water column by strong stratification, full depth cells also dominate the horizontal transport of sediments, as their strong vertical velocities elevate wave-mobilized sediments out of the bottom boundary layer into the mid and upper water column where currents are stronger compared to the bottom. Since their discovery, LSC have been increasingly gaining prominence in coastal oceanography research, with special attention being given to parameterization and comprehension of what forcing conditions may give rise to LSC structures, including comparison of dominating forcing in regime diagrams (Gargett and Grosch, 2014), or forcing spaces (Gargett, 2022). Since the first demonstrated LSC by Gargett et al. (2004), similar full depth structures have been observed at deeper sites, such as in 26 meters depth on mid-shelf off the coast of Georgia (Savidge and Gargett, 2017; Savidge et al.; 2008; Gargett et al., 2014), which raised further questions about what conditions are conducive to the formation of LSC features and how deep they can occur.

To tackle the questions posed above, I verify the method using some of the deepest Langmuir Supercells events observed to date: those examined by Savidge and Gargett (2017) in

26m water depth off Georgia, in approximately the middle of the South Atlantic Bight (SAB), the broad and shallow continental shelf of the southeastern United States between Cape Hatteras and Cape Canaveral. The SAB is underlain predominantly with sandy sediments that host populations of benthic primary producers, primarily diatoms. Because much of the SAB bottom is within the euphotic zone - the average shelf depth is 26 m, with a 60 m depth shelf break (Jahnke et al. 2008) - these populations contribute substantially to total primary production in the SAB (Nelson et al. 1999). Consequently, processes that affect bed mobilization and horizontal sediment transport during high wind and wave events are of interest to understand bed evolution, sediment transport, and the fate of organic carbon.

From 2007-2009, the Benthic Observatory Technology Testbed on the Mid-Shelf – Understanding Processes (BOTTOMS-UP) project (Savidge et al., 2008) imbedded a suite of instrumentation in the SAB at the 26 m isobath to examine fluxes within and processes affecting the seabed. BOTTOMS-UP was imbedded within an existing longer-term year-round observatory on the continental shelf of Georgia, the South Atlantic Bight Synoptic Ocean Observing Network (SABSOON), operated by the Skidaway Institute of Oceanography (SkIO). In particular, BOTTOMS-UP added a five-beam 600 kHz acoustic Doppler current profiler (VADCP) sampling at 1 Hz and full depth temperature measurements at 1 m vertical interval (Hobo TidBits, T-chain) to existing SABSOON meteorological and in-water sensors at the Navy tower ‘R2’ (Fig. 5.1).

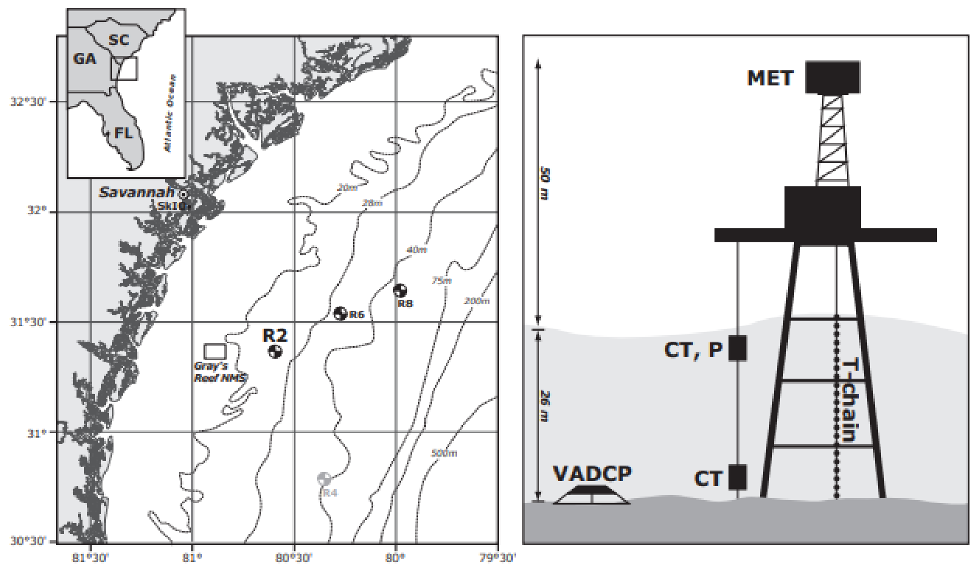


Figure 5.1: BOTTOMS-UP study site and instrumentation. Left panel: SkIOs SABSOON observatory instrumented several Navy towers on the SAB shelf, including R2 at the 26 m isobath, R6 at the 35 m, and R8 at 42 m, near the shelf break. Of the three, R2 was the most continuously operated over the 10-year period of observatory operation. Self-contained project-specific instrumentation was deployed by colleagues sporadically at E4, at approximately 40 m depth. Right panel: Schematic of BOTTOMS-UP instrumentation at R2 included a 1 m resolution HOBO T-chain, a VADCP mounted on a pipe jetted into the sandy sediments, leveled by diver so that the vertical beam was within 0.6° deg of vertical, and cabled to the R2 tower above water instrumentation. These assets were imbedded within the existing SABSOON instrumentation at R2, which included a meteorological package as described in the text, near surface and near bottom Seabird microcat CTs, and a near surface ParoScientific wave and tide gauge (Savidge and Gargett, 2017).

One primary result from BOTTOMS-UP was the demonstration of Langmuir circulation extending through the entire water column (Savidge and Gargett 2017). As at LEO, LSCs on the

Georgia shelf appear to be the predominant response of the coastal ocean to high wind and wave events. An example event from the BOTTOMS-UP project is apparent from backscatter and vertical velocity from the VADCP along with thermal stratification from the T-chain, winds and significant wave height (Fig. 5.2). Savidge and Gargett (2017) first described this event and diagnosed these phenomena as full depth Langmuir cells, similar to those first discovered at LEO. Diagnosis depended upon a number of analysis techniques utilizing the rich and unique look afforded by well-leveled VADCPs sampling at high frequency. Such approaches include examining short periods of wind-aligned three-dimensional velocity timeseries, to determine whether cell-like structures exist, conditional averaging of sequences of such structures, vertical profiles of normal and shear stresses, Lumley traces of higher order invariants, and wavelet analysis of the time variation of defining parameters like vertical velocity fluctuations (Gargett et al., 2004; Gargett and Wells, 2007, Gargett et al. 2014; Savidge and Gargett, 2017).

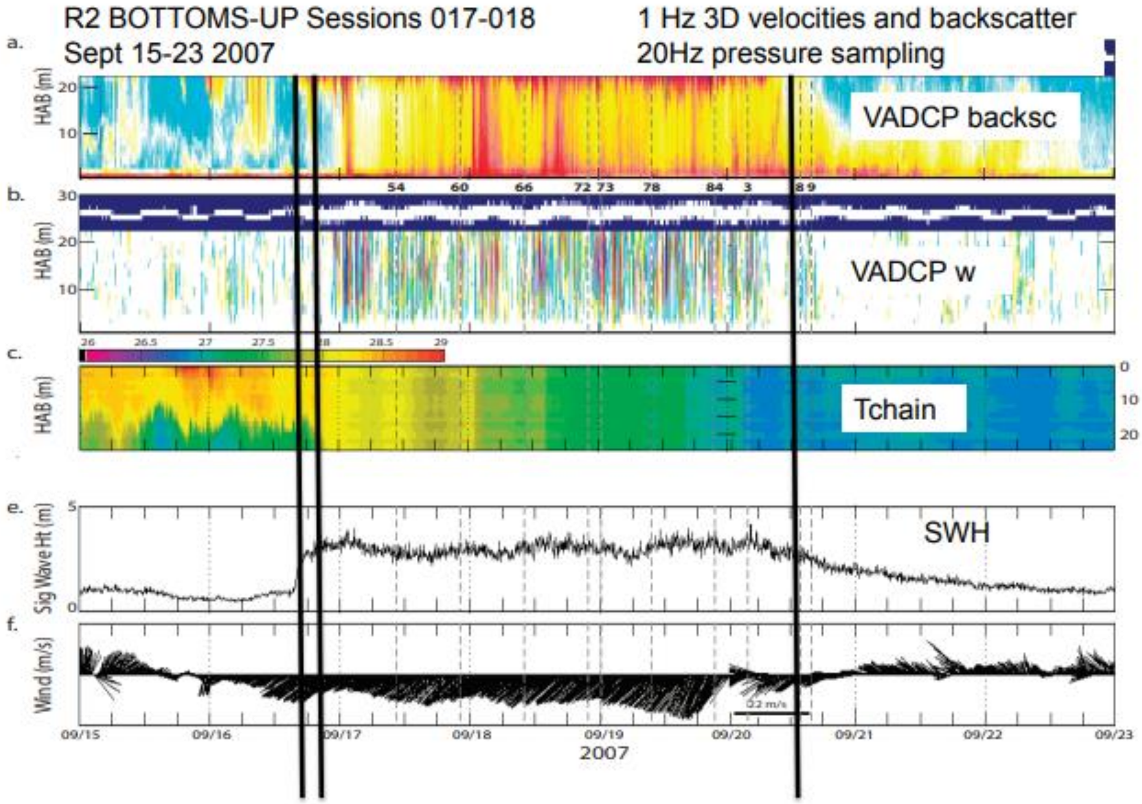


Figure 5.2: Copy of Figure 3.1. High wind and wave event recorded at R2, September 2007.Vertical beam acoustic Doppler current profiler (VADCP) data were subdivided into approximately 7-day sessions, subdivided and sequentially numbered into 2-h records. Shown are session 17, records 46–84, and session 18, records 1–36, 15–23 September 2007 (record numbers marked at the top). Panels are backscatter (a) and vertical velocity (b) from the VADCP fifth beam, with surface location (white) as identified in vertical beam backscatter; temperature evolution (c); low-frequency plus tidal water depth variation (d); significant wave height (e); and vector wind at 50 m (f). Panels a,b,c plotted as a function of height above bottom (HAB) in m, extracted from Savidge and Gargett (2017).

Given the demonstration of LSC on the Georgia mid-shelf at almost twice the depth where they were first identified at LEO, and the disproportionately large effect they have on sediment transport (including organic carbon therein), the maximum shelf depths to which they can affect sediments becomes an important question. The two VADCP datasets used so far in examining LSC (LEO, 15 m depth, and R2, 26 m depth) were both installed within existing observatory settings, and thus benefitted from sufficient power, bandwidth and memory capacity to accommodate 1 Hz sampling and storage of velocities and backscatter from 1 *m* bins along all five beams. Such observatories also offer measurements of meteorological and auxiliary in-water parameters that are useful in the examination of storm events. Unfortunately, such observatory level power, bandwidth or memory are exceedingly rare, limiting the ability to investigate the potential for LSC existence elsewhere.

At both tower R2 and LEO, Gargett et al. (2016) found that, in the absence of stratification, with constant wind direction, and wind-aligned waves, LSC are observed in VADCP data when the wave field is 'intermediate' in character (Fig. 5.3) and the Rayleigh number ($Ra$) becomes 'small': $\log_{10}(Ra)<5.5$ (Table 3.1 or 5.1) as derived in Gargett and Grosch (2014). A further precondition is that either the Langmuir number ($La$) or its square root, the turbulent Langmuir number ($La_t$) is 'small': $\log_{10}(La)<-0.5$ (Table 3.1 or Table 5.1), as defined by thresholds in Gargett and Grosch (2014) and Li et al. (2005). This precondition is routinely met for high wind and wave events at the two locations where LSC have been observed.

The requirement for a transition to a wave field that is 'intermediate' in character is fairly intuitive. Since Stokes shear is responsible for driving Langmuir cells, wave fields with shear that extends to the bottom would seem consistent with cells reaching bottom (Fig. 5.3). While the circular orbits of deep ocean waves have large vertical shear in horizontal orbital velocities in the upper ocean, that shear does not extend to the bottom. Shallow water wave elliptical orbits extend to the bottom but exhibit almost no shear in horizontal wave velocities. Intermediate wave elliptical orbits extend to the bottom, exhibiting vertical shear in the horizontal velocities throughout the water column. This suggests why intermediacy is important for Langmuir circulation to develop in a wave field with Stokes drift (i.e., a wave field that deviates from linearity). Calculations with the complete wave equations support the assertion that maximum Stokes drift near bottom occurs for intermediate wave fields.

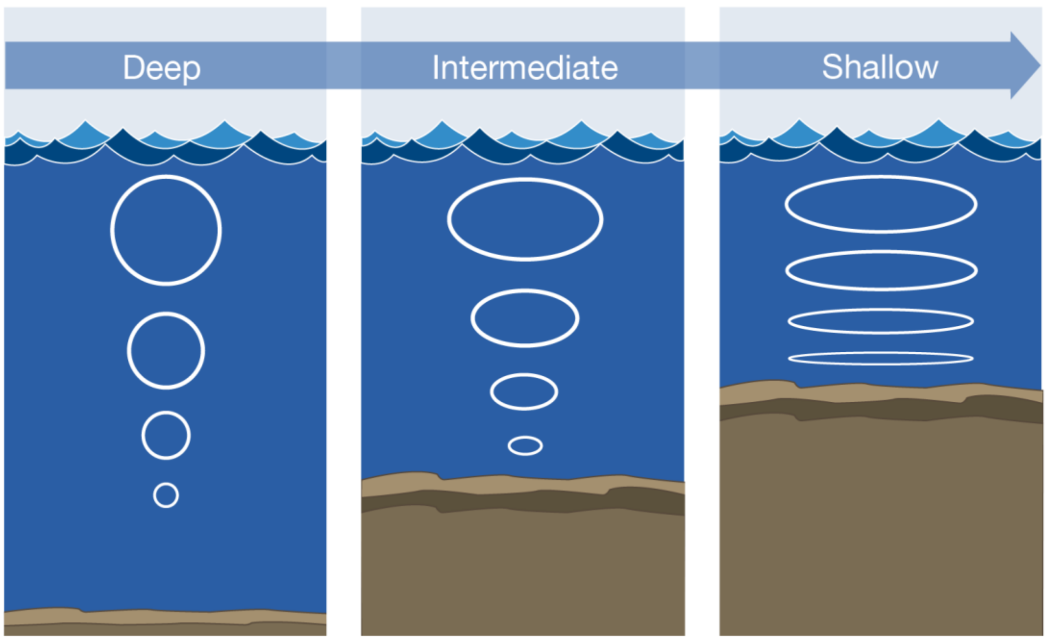


Figure 5.3: Wave elliptical trajectories under distinct wavelength/depth ratios. Panels from left to right respectively presenting typical wave trajectories for deep, intermediate, and shallow waves. Waves start “feeling” the bottom at the intermediate state, leading to increased eccentricity with depth.

The Rayleigh number used herein as a representation of buoyancy forcing relative to vortex forcing results from a non-dimensionalization of the momentum equation appropriate to the storm-forced coastal ocean (Gargett and Grosch, 2014). Calculation of *Ra* requires measurements or estimates of surface heat fluxes, wind stress and near-surface wave spectra. As in Gargett and Grosch (2014), wave spectra, wind-stress and heat-fluxes, are used to calculate *Ra*, where the wave spectra contribute to the definition of turbulent timescale, $t_*$. Wave spectra and wind-stress are used to verify low *La* or $La_t$, in all high wind and wave events examined. For clarity, all important parameters and their mathematical definitions are shown in Table 5.1 (First copy of Table 3.1 added here for easier accessibility).

Table 5.1: Reference table for key parameters and equations (Adapted copy of Table 3.1).

| **Variable** | **Description** | **Calculation** |
|---|---|---|
| $U(x_3)$ | Mean velocity | From VADCP data |
| $U_S(x_3)$ | Stokes velocity | Equations 5.9/5.10 |
| $u_*$ | Surface stress velocity scale | $u_* = \left(\frac{\tau}{\rho_0}\right)^{1/2}$ * |
| $u_{S0}$ | Surface Stokes velocity | $u_{S0} = U_S(0)$ |
| $t_*$ | Time scale | Equation 5.3 |
| $Ra$ | Rayleigh number | Equation 5.2 |
| $La$ | Langmuir number | Equation 5.4 |
| | | (*$\boldsymbol{\tau}$ is the shear stress, and $\boldsymbol{\rho_0}$ is the density) |

The parameters necessary to examine wave character and *Ra* to assess whether forcing is consistent with the production of LSC (high resolution velocity, heat fluxes, wind-stress, and wave spectra) are available from weather/oceanographic buoys around the world, such as the

NDBC network in the United States. Such buoys collect most of the wave and meteorological parameters needed to assess forcing with these two diagnostics (*Ra*, *La*). For example, buoy 41008, located on the Georgia shelf at 15 m depth records hourly wind speed and direction, wave spectra, water temperature, air temperature and relative humidity. With the exception of longwave and shortwave surface heat fluxes, everything needed to assess *Ra* and the wave field character are available at buoy 41008.

In the following, a method to estimate the missing heat-flux components is devised, based on satellite sea surface temperature (SST) records. *Ra* and wave character estimates are made from these combined NDBC and SST parameters, referred herein as the Estimates from Commonly Available Data (ECAD) method. These ECAD forcing assessments are then compared to direct diagnosis of LSC from both the internal (VADCP diagnostics) and external (forcing diagnostics from winds, waves, and surface heat fluxes) measured at navy tower R2. Once the efficacy of the ECAD method is evaluated, I apply it to a data set acquired in 2015 off the coast of Duck, NC, in 39 m water depth as part of the Coupled Air-Sea Processes and Electromagnetic Wave ducting Research (CASPER) project (Wang et al., 2016). External diagnostics estimated from the high frequency (hourly) co-located wind, wave and heat flux estimates and from the NDBC buoy-based estimates, including the ECAD shortwave ($Q_{sw}$) and longwave ($Q_{lw}$) radiation estimates are examined to identify whether LSC events occur in the deeper CASPER dataset, which is validated with demonstration of LSC using high frequency VADCP internal diagnostics.

## 5.2 DATA AND METHODS

### Estimating Parameters

In the following, ‘external diagnostics’ of LSC (i.e., the wave character and *Ra* diagnostics used to identify periods when LSC are expected as the predominant circulation response to wind and wave forcing) are described alongside ‘internal diagnostics’ (i.e., the expression of LSC circulations in the water column from measured velocities and associated diagnostics).

Rarely a single forcing is responsible for turbulence production in the oceans, and it is necessary to understand which forcing dominates turbulence production to assess the presence of LSC. Turbulence is generated at the surface of the ocean through direct action of the wind stress and indirectly though the effects of the wind on the surface waves, as well as the wind effects on convection and the level of destabilization due to buoyancy flux that may compete with wind-wave forcing as seen in the transport equation for TKE Budget following (Kitaigorodskii and Lumley, 1983; Polton and Belcher, 2007):

$$0 = -\overline{u'w'}\frac{\partial \bar{U}}{\partial z} - \overline{v'w'}\frac{\partial \bar{V}}{\partial z} - \overline{u'w'}\frac{\partial U_s}{\partial z} + \overline{w'b'} - \frac{\partial}{\partial z}\left(\overline{w'E'} + \frac{1}{\rho}\overline{w'p'}\right) - \in, \qquad (5.1)$$

where *u* is the horizontal component parallel to surface stress, and *v* is the perpendicular component; overbar denotes average; *w* is the vertical component of the current, with positive sign upwards; $\rho\overline{u'w'}$ and $\rho\overline{v'w'}$ are components of the Reynolds stress vector, where the primes denote fluctuations from the mean. $\overline{w'b'}$ is the turbulent buoyancy flux, $\overline{w'E'}$, the turbulent energy flux, $\overline{w'p'}$ the pressure work flux; $\in$ is the dissipation rate; and $\rho$ is density.

In Equation 5.1, the first two terms of the right-hand side represent production of TKE due to shear in the mean current, the third term is production due to Stokes shear, the fourth is production or destruction due to buoyancy effects, the fifth term represents transport of TKE due to turbulent fluctuations, and the sixth term is the destruction of TKE due to viscous effects.

Gargett and Grosch (2014) demonstrated that situations dominated by either Langmuir vortex forcing (necessary for LSC), or destabilizing surface heat flux (dominated by convection) can be identified by distinct locations in log (*La*-*Ra*) space, which allows for the identification of the dominate forcing behind measured velocity fluctuations, as the conditions for development of LSC requires that the forcing due to wind-wave interactions dominate over convection. An explanation of the estimation of *La* and *Ra* follows.

Total fluxes are then used to calculate *Ra* as:

$$Ra = \left(\frac{\alpha_T g}{\kappa_T}\right)(Qt_*^2), \tag{5.2}$$

Where $\alpha_T$ is the coefficient of thermal expansion, $g$ is the acceleration of gravity, $\kappa_T$ is the thermal conductivity, $Q$ is the surface heat flux, and $t_*$ (Table 5.1) is a time scale, $t_* = g_*{}^{-1}$, $g_*$ being the LSC growth rate:

$$t_* \equiv \left(\frac{dU_S}{dx_3}\frac{dU}{dx_3}\right)^{-1/2}, \tag{5.3}$$

And the Langmuir number is defined as:

$$La \equiv \left(\frac{u_*}{u_{S_0}}\right), \tag{5.4}$$

Where $U_S$ is the Stokes velocity, $U$ is the mean velocity, $u_*$ is the surface stress velocity, $u_{S_0}$ is the surface stokes velocity, and $x_3$ is vertical distance with positive upwards from the water surface.

A value for $u_{S_0}$ is necessary to determine *La*. The appendix of Gargett and Grosch (2014) shows that for a single inviscid, incompressible wave with amplitude *a*, wavenumber *k*, frequency $\omega$, where *H* is water column depth, and surface displacement is idealized as $\varsigma = a\cos(kx-\omega t)$, surface displacement variance relates to the variance of vertical velocity ($\langle w_h \rangle^2$) measured at height above bottom *h* as:

$$\langle \varsigma^2 \rangle = \langle {w_h}^2 \rangle \left( \frac{\sinh{(kH)}}{\omega \sinh{(kh)}} \right)^2, \tag{5.5}$$

This method assumes that the surface wave spectrum depends only on frequency (wavenumber) when winds and waves are aligned. It is further assumed that $\langle w_h \rangle^2 = \int_0^\infty \Phi_w(\omega) d\omega$ can be converted to an operator so the vertical velocity spectrum relates to surface displacement spectrum as:

$$\langle \varsigma^2 \rangle = \int_0^\infty \Phi_\sigma(\omega) d\omega = \int_0^\infty \Phi_w(\omega) \left( \frac{\sinh{(kH)}}{\omega \sinh{(kh)}} \right)^2 d\omega, \tag{5.6}$$

Assuming a unidirectional surface wave spectrum, the vertical shear Stokes velocity is the integral over a Stokes shear function *S(ω,x*₃*)* defined as:

$$\frac{dU_S(x_3)}{dx_3} = \int_0^\infty 2\, \Phi_\sigma(\omega) \omega k^2 \frac{\sinh{(2k)(x_3+H)}}{sinh^2 kH} d\omega = \int_0^\infty S(\omega, x_3) d\omega, \tag{5.7}$$

where $\omega$ and k are related by the full-dispersion relationship:

$$\omega^2 = gk\, tanh(\, kH) \tag{5.8}$$

and the displacement spectrum $\Phi_\sigma$ is estimated from $\Phi_w$, the noise-corrected spectrum of vertical velocity measured by the vertical beam of the VADCP at height *h* above bottom (depth $x_3$ = - (*H* – *h*)). Since Equation 5.7 is integrated between 0 and infinite frequency, Stokes shear may become unbounded. Gargett and Grosch (2014) shows that the integral is bounded when computed at distances sufficiently below $x_3$ =0.

A spectral Stokes velocity associated with surface wave displacement spectrum $\Phi_\sigma$ is given by the integral over frequency of the Stokes function $S(\omega, x_3)$:

$$U_S(x_3) = \int_0^\infty 2\Phi_\sigma(\omega) \omega k \frac{\cosh{(2k)(x_3+H)}}{2sinh^2(kH)} d\omega = \int_0^\infty S(\omega, x_3) d\omega, \tag{5.9}$$

In the diagnosis of LSC to date, this measure is primarily used during periods when net heat fluxes are positive, or out of the ocean. These periods are used because destabilizing fluxes could compete with LSC as the dominant source of observed turbulence, as measured by *Ra*, though LSC may develop in stabilizing heat flux conditions (Gargett, 2022).

The surface Stokes velocity $U_{S_0} \equiv U_S$ ($x_3$=0) can be unbounded, but the Stokes velocity can be calculated by evaluating equation 5.9 at a small depth below the surface or by band limiting the surface integral. The latter option has been chosen here (following recommendation from Gargett and Grosch, 2014) and $u_{S_0}$ is computed as the integral of equation 9 at $x_3 = 0$ over the range $0.005 < f < 0.4$ cps.

Gargett and Savidge (2020), adapts this method using a formulation of the directional wave spectra from ADCP vertical and slant beam velocities, as:

$$U_S(x_3) = \int_0^{2\pi}\int_0^{\infty} 2\Phi_\sigma(\omega,\theta)\omega k \frac{cosh2k(x_3+H)}{2sinh^2kH} d\omega d\theta = \int_0^{2\pi}\int_0^{\infty} S(\omega, x_3)d\omega, \qquad (5.10)$$

Directional wave spectra are used when the surface displacement wave spectra depend on direction, or to verify assumptions of wind-aligned waves, which was the case for Gargett and Savidge (2020), where directional wave spectra showed consistent results to those of wind-aligned wave spectra calculated from VADCP data at R2.

The wave field character is obtained from the Stokes Velocity scale associated with surface wave displacement spectrum $\Phi_\sigma$, estimated from wave spectra following Equation 5.9. To determine whether intermediate waves are contributing to the Stokes drift, the integration is split between shallow, intermediate, and deep wave contributions. Shallow-water and deep-water waves are defined using local water depth (*H*) and wavelength ($\lambda$) as $\lambda_{shallow} > 20H$ and $\lambda_{deep} \leq 2H$ with intermediate waves between these two thresholds.

**Datasets**

Subsets of data from several projects are referred to in the following. SABSOON (Seim, 2000) instrumentation at three Navy towers on the Georgia shelf resulted in a near continuous ten-year record of multiple parameters (i.e., IMET, ADCO, wave data, CTD, etc.) at R2 (65 km offshore) from 1999-2009, with more limited temporal and parameter coverage at towers R6 and R8 (Fig. 5.1). IMET packages (Seim, 2000) subsets of the in-water suite available at R2 were sporadically deployed at R6 and R8. Data from NDBC buoy 41008, located at 31.4 N 80.866 W (28.5 km northwest of R2) in 15 *m* depth water, within the Gray's Reef Marine Sanctuary has also been accessed. In the following, concurrent measurements from Gray's Reef and towers R2 and R8 in 2004 are examined.

Savidge and Gargett (2017) imbedded instrumentation within SABSOON at the R2 tower to examine the in-water response to high winds and waves at R2 during BOTTOMS-UP with a custom cabled RDI 600 kHz VADCP, sampling all five beams nearly synchronously at 1 Hz. The instrument was affixed to a diver-jetted-in pipe and leveled to within 0.5 degrees of vertical. The 2004 R2 event is compared with the parameters measured at R2 augmented by the BOTTOMS-UP project during 2007-2009 (Savidge et al., 2008). Backscatter from both the 300 and 600 kHz instruments is inspected to indicate periods when bubble clouds exist near the surface, and when near bottom or full-water backscatter indicates the mobilization of sediments. High intensity backscatter at the top of the water column during high wind and wave conditions indicates wave-breaking. In contrast, high intensity backscatter on the bottom of the water column during such conditions are associated with bottom sediment resuspension and transport.

Estimates from pressure records at towers R2, R6, and R8 were obtained from ParoScientific pressure gauges mounted on towers at 6 m below mean sea level, sampling at 20 Hz and corrected for pressure attenuation with depth using linear wave theory (eliminating frequencies of 0.25 Hz and higher to avoid noise amplification; Bishop and Donelan, 1987). The 6-minute 20 Hz sampling intervals were used to estimate wave spectra from the pressure records, which were then integrated in frequency to estimate significant wave height (Savidge and Gargett, 2017). Wave spectra were also assessed over each 2-hour interval of the VADCP data. Additionally, directional and non-directional wave spectra were also estimated at R2 from the VADCP using near-surface beam velocities, as described in Gargett and Grosch (2014) for each 2-hour record. Hourly wave spectra were also obtained from NDBC buoy 41008. Instrumentation, sampling, and processing details are available through the NDBC website (https://www.ndbc.noaa.gov/).

Meteorological data from towers R2, and R6 came from packages mounted at 50 m above the sea surface, while the met package at R8 was at 38 m height above the sea surface. Instruments included an anemometer (R.M. Young, Traverse City, MI) for wind speed and direction, relative humidity, and air temperature sensors (Rotronics, Hauppauge, NY), barometric pressure (IntelliSense, Woburn, MA), and pyranometry. (Eppley, Newport, RI). All instruments were operated continuously and recorded averaged values at 6-min intervals. Near surface water temperature was also available nearly continuously at R2 from a Seabird SBE-37 sensor, with identical sensors deployed more intermittently at R6 and R8, all positioned ~6 m subsurface. During BOTTOMS-UP, a T-Chain of internally recording temperature sensors (Onset HOBO Tidbits) with 1 m vertical spacing was also deployed at tower R2, sampling continuously at 5-minute intervals.

Meteorological data was also available hourly from NDBC buoy 41008, including relative humidity, air temperature, wind speed and direction. Instrument and sampling details are available on the NOAA NDBC website (https://www.ndbc.noaa.gov/). The wind sensor is situated 4.9 m off the sea surface. Near surface water temperature was also available hourly.

Finally, in the fall of 2015, a diver-leveled Nortek Signature 500 VADCP was deployed off the coast of Duck, NC, in 40-meter water depth, as an NSF-sponsored addition to the ONR project known as CASPER: Coupled Air-Sea Processes and Electromagnetic (EM) Ducting Research (Wang et al., 2018). For this analysis, data from nearby NDBC buoys 44014 (36.609 N 74.842 W) and 41025 (35.010 N 75.454 W) are used for standard buoy data and to estimate heat fluxes using the ECAD method. The CSP VADCP sampled all five beams synchronously at 4 Hz, saved as beam velocities and backscatter, which were subsequently averaged to 1-Hz, and divided into two-hour records from September 11 through October 10, as in Savidge and Gargett (2017). As with the LEO and BOTTOMS-UP VADCP deployments, a spectral gap fortuitously existed between the wave and turbulent responses signals in the records, allowing for a 20-sec low-pass filter to effectively separate those signals with no need of more elaborate methods (processing details follow Savidge and Gargett, 2017).

As in the analysis of earlier data sets, backscatter signal was inspected after correction for beam spreading and attenuation following Savidge and Gargett (2017). Unfortunately, raw backscatter intensity for the CASPER dataset was saturated through much of the lower water column during wind and wave events, as the signal fell in excess of the linear range of transducer response and so cannot be used (NORTEK, 2001). While sediment resuspension signals in backscatter is a convenient starting point for detecting potential LSC events, it is a consequence, not a cause of LSC. Therefore, the absence of a good sediment resuspension indicator would not prevent the identification of LSC formation by other means (e.g., forcing space, regime diagram, conditional averages, full depth velocity fluctuations, Reynolds and normal stress profiles, Stokes drift profiles).

**ECAD method to estimate heat flux**

Wind stresses at 41008 and the Navy towers were estimated by first converting wind speeds at their measurement heights to that at 10 m, using the method of Smith (1988) and then converting to stress estimates following Large and Pond (1981). Air-sea bulk sensible and latent heat fluxes are calculated for Navy tower and Buoy 41008 data following Fairall et al. (1996). Pyranometer measurements at the towers also permit estimates of shortwave and longwave heat fluxes at those locations. Wind, stress, and flux calculations were all performed in MATLAB using the air-sea toolbox (Pawlowicz et al., 2001).

Pyranometers are not routinely deployed at NDBC buoys, nor are such measurements available at Buoy 41008. To arrive at estimates of shortwave and longwave heat fluxes using just NDBC buoy data in-situ, an ECAD approach was devised. First, satellite SST imagery was examined (in this case, from the Rutgers repository), and a daily flag assigned to indicate level of cloudiness in the immediate vicinity of Buoy 41008. Flags ranged from 0 (complete cloud cover over the region) to 1 (completely clear all around) by 0.25 increments.

Using this assessment of cloud cover, first a cloud correction factor is estimated (cloudcor function in MATLAB air-sea toolbox) and used as input (blwhf function in MATLAB air-sea toolbox) along with measured surface temperature to estimate net longwave at the buoy. Both functions were used selecting the Bunker option for the parametrization bulk formula as described in Fung et al., (1984). Knowing cloud cover, SST, $T_{air}$ and the relative humidity, this function calculates net heat loss from the ocean considering an estimate of the part emitted by the ocean as black-body radiation reflected back into the ocean by cloud cover and the atmosphere. Net longwave radiation must vary between the maximum emitted by the ocean and zero. For this location in September, the average net values are several hundred $W/m^2$, and do not vary appreciably, since it depends mostly on SST, and instantaneous changes in cloud cover are not reflected in these assessments based on daily SST.

To estimate shortwave fluxes, first the no-sky hourly insolation was calculated with the Smithsonian formula for the latitude and time/date of the periods of interest. Next the clear sky daily average was estimated from the clskswr function (MATLAB air-sea toolbox) and used to downscale the no-sky hourly estimates following Reed (1977). Finally, these clear sky hourly estimates were diminished according to the cloud cover flags from the SST imagery, by up to 50% for complete cloud cover. This maximum degradation is actually not quite sufficient, in comparison to that measured on very cloudy days by the pyranometers at the towers. This result may also be region, humidity, or cloud-type dependent.

All four heat flux components were estimated using data from NDBC buoy 41008 and at towers R2 and R8, and the ECAD estimates of $Q_{lw}$ and $Q_{sw}$ at all three locations were compared with Navy Tower R2 and R8 pyranometer data. Not surprisingly, sensible and latent heat fluxes for the three locations were equivalent to each other, as the estimates are from nearby locations using similar measurements and identical methodology. ECAD $Q_{lw}$ and $Q_{sw}$ estimates were also similar at the three sites, however, compared slightly less well with the R2 and R8 pyranometer based $Q_{lw}$ and $Q_{sw}$. For $Q_{lw}$, the reduction of fairly uniform background values during storms is of very small magnitude relative to storm enhanced sensible and latent heat flux losses. The real shortcoming of the ECAD method for buoy 41008 is in the shortwave comparison to that measured at the tower nearby. One saving grace is that increased cloud cover diminishes both $Q_{sw}$ into the ocean (in daylight) and $Q_{lw}$ out of the ocean, so their storm contributions compensate somewhat, whether measured properly, or roughly estimated. Total heat flux from the ECAD method at buoy 41008 and the measurements from towers R2 and R8 illustrate remarkably good agreement for positive total flux values, while negative values suffer more from the poor-quality ECAD shortwave estimates, however it is primarily the positive values that are of the most interest, since to date only episodes during destabilizing heat fluxes have been examined.

Once validated, the ECAD method presented herein can be used for deeper sites with no available pyranometer data for longwave and shortwave radiation, such as for the CASPER dataset. For CASPER, meteorological data from NDBC buoys 44014 and 41025 were used to estimate wind stress, speed, and direction. The use of two nearby buoys was ideal in this situation as the passage of Hurricane Joaquin during session 301 contributed to a horizontal gradient in the wind velocity field near the VADCP.

## 5.3 RESULTS

### Georgia Shelf in 2007 (BOTTOMS-UP at Tower R2) and 2004 (Towers R2, R8 and Gray's Reef NDBC Buoy 41008)

Using a range of diagnostics to assess competing forcing and the circulation response from VADCP data, Savidge and Gargett (2017) demonstrated LSC extending to the bottom in 26 m depth waters at R2 on the Georgia shelf. A shortened demonstration is shown here, using just the three criteria as described by Gargett and Grosch (2014), of intermediate wave character, $\log_{10}(|Ra|) < 5.5$, $\log_{10}(La) < 0.5$. The demonstration is repeated using the multiple types of wave field estimates available (41008 buoy, R2 VADCP and pressure gauge, Fig. 5.4) and for both the measured and ECAD versions of $Q_{lw}$ and $Q_{sw}$. A further demonstration is made on the Georgia shelf in September 2004, when appropriate data from Gray's Reef buoy 41008, Tower R2 at 26 m depth and Tower R8 at 42 m were all available to assess the three criteria. Bottom mounted ADCP 6-min average data was also available at R2 and R8 to give an indication of the ocean response, though not at the level of detail that the 2007 VADCP 1 Hz sampling provided.

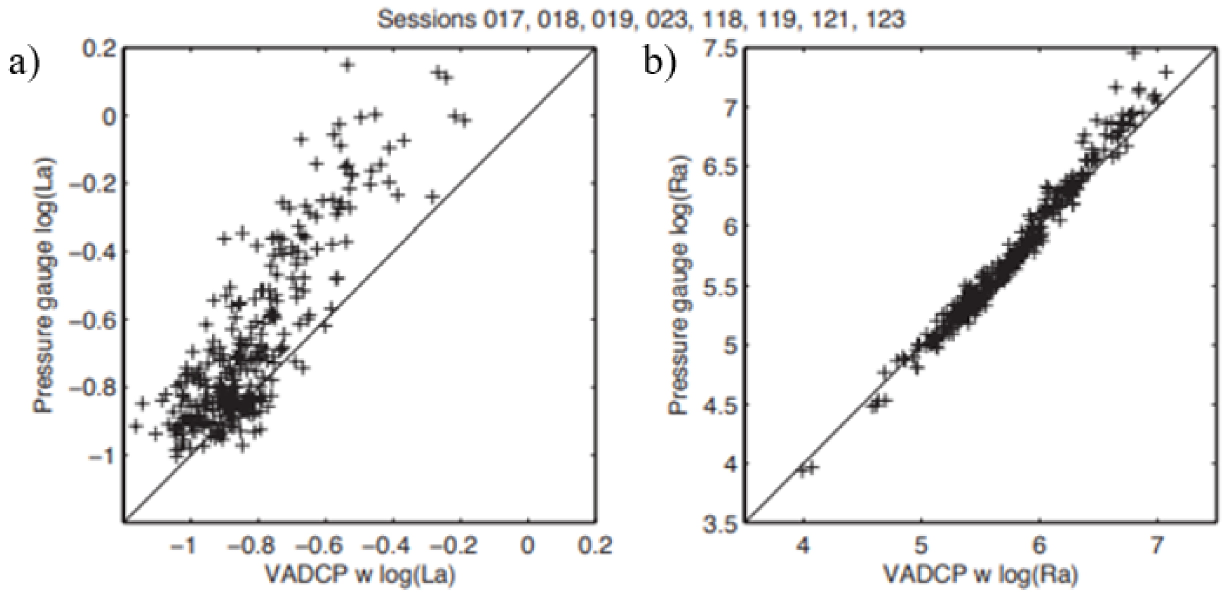


Figure 5.4: R2 VADCP estimate of forcing parameters a) *La* and b) *Ra* and pressure gauge.

$\text{Log}_{10}(Ra)$ consistently falls below the threshold during periods of high wind, apparently modulated by the magnitude and sign of estimated total heat flux (Fig. 5.4a). In 2007, the *Ra* estimates based on the ECAD (satellite SST-based) $Q_{lw}$ and $Q_{sw}$ track those estimated from measurements well (Fig. 5.5). Very little difference is evident between different methods of measuring waves, whether by pressure sensor or using VADCP beam velocities. *Ra* estimates from the two locations R2 and 41008 are not appreciably different, despite the different depths (*H*), and likely different $t_*$ contribution to *Ra* from a wave field in a shallower ocean.

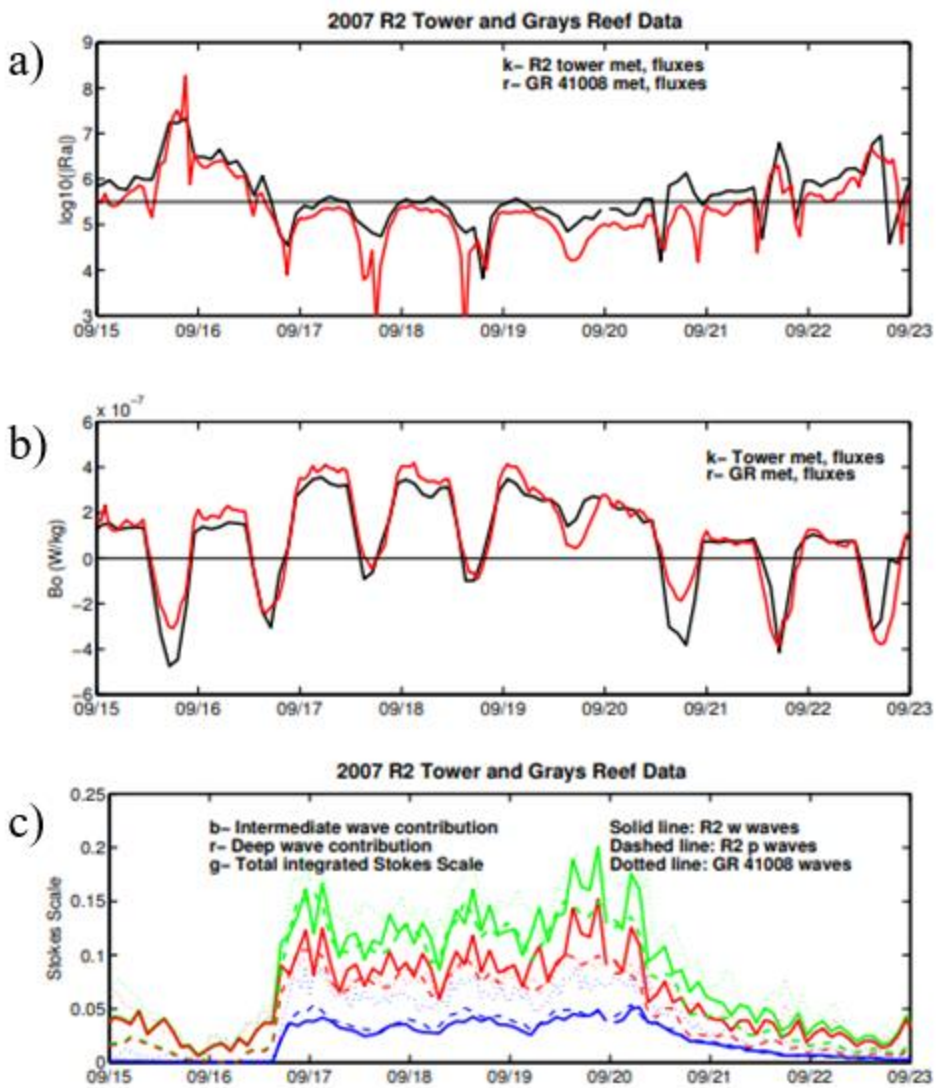


Figure 5.5: Diagnostics for timeseries shown in Figure 5.2.

The evolving intermediate character of the wavefield is illustrated by increasing magnitudes of the components in the Stokes velocity scale of wavelengths longer than 0.2*H (Fig. 5.5c). For this diagnostic, the water depth does make a noticeable contribution between Gray’s Reef and R2. The wave spectrum from a shallower location will likely contain more intermediate wave content, though the total Stokes value is roughly equivalent at the two locations.

Eliminating the periods when the water column is stratified, periods of low *Ra*, non-zero and intermediate wave contribution to intermediate Stokes scale velocities ($v_{si}$) correspond well to high backscatter, large vertical velocity periods that Savidge and Gargett (2017) identify as LSC (Fig. 5.6). Further, *Ra* and $v_{si}$ (the intermediate wave contribution to the Stokes velocity scale) estimates from the ECAD method appear to reasonably correspond to high backscatter, large vertical velocity periods, so reasonably predict periods when LSC were present.

In September 2004, the two navy towers R2 and R8 were both equipped with sufficient instrumentation to calculate the high-resolution external diagnostics for comparison to estimates from 41008 over the same period. These are useful to explore a greater range of depths than in the 2007 data. In addition, standard four-beam ADCPs were deployed at both tower locations during this period. Periods of high winds and wave appear at both locations along with coincident elevated backscatter (Fig. 5.6).

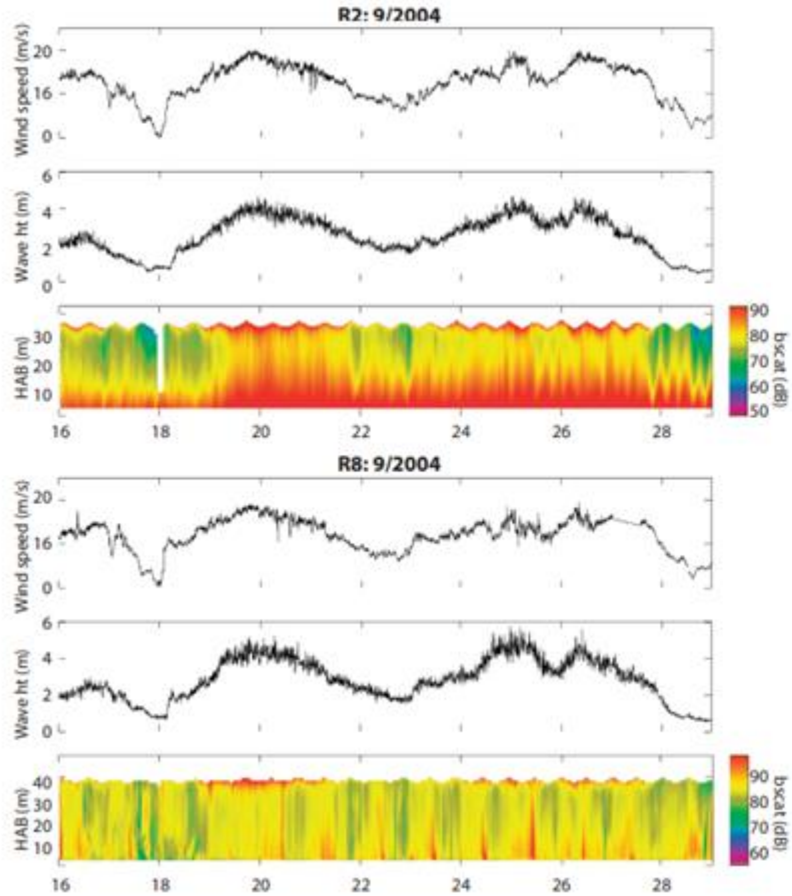


Figure 5.6: Timeseries from towers R2 and R8 in September 2004. Upper three panels are time series of 6-minute averages from tower R2 including speed at 50m height above the sea surface, significant wave height from integration of 6-minute subsamples of 20Hz pressure data, and 600kHz ADCP backscatter corrected for attenuation and beam spreading. Lower three panels are similar data from tower R8 where backscatter from a 300kHz ADCP is shown, corrected for attenuation and beam spreading.

The September 2004 *Ra* and $v_{si}$ estimates from the towers and Gray's Reef also indicate several periods during which both criteria for LSC are met. The evolving intermediate character of the wavefield is illustrated by increasing magnitudes of components in the Stokes velocity scale of wavelengths longer than 0.2*H (Fig. 5.7). $U_s$ increases with increasing depth on the shelf, consistent with larger significant wave heights farther offshore during most storm system passages. The onset of non-zero values in the component due to intermediate range of waves shows earlier onset in shallower water. Intermediate wave character coincides with reduced *Ra* during high wind and wave environments in most of the estimates for 2004, but for these cases, it is not clear whether one routinely precedes the other in the onset of LS. Both the magnitude of the intermediate wave part and the percentage of the total $U_s$ that intermediate waves represent ($v_{si}$) varies with depth and storm event, so that a threshold value of either has not yet been established. Thus far, direct measurements of LSC velocity structure by VADCP (at R2 in 2007) has coincided with even slight onset of non-zero $v_{si}$. Closer inspection of a sequence of LSC die-off periods may assist in determining what percentage or magnitude is ‘enough’.

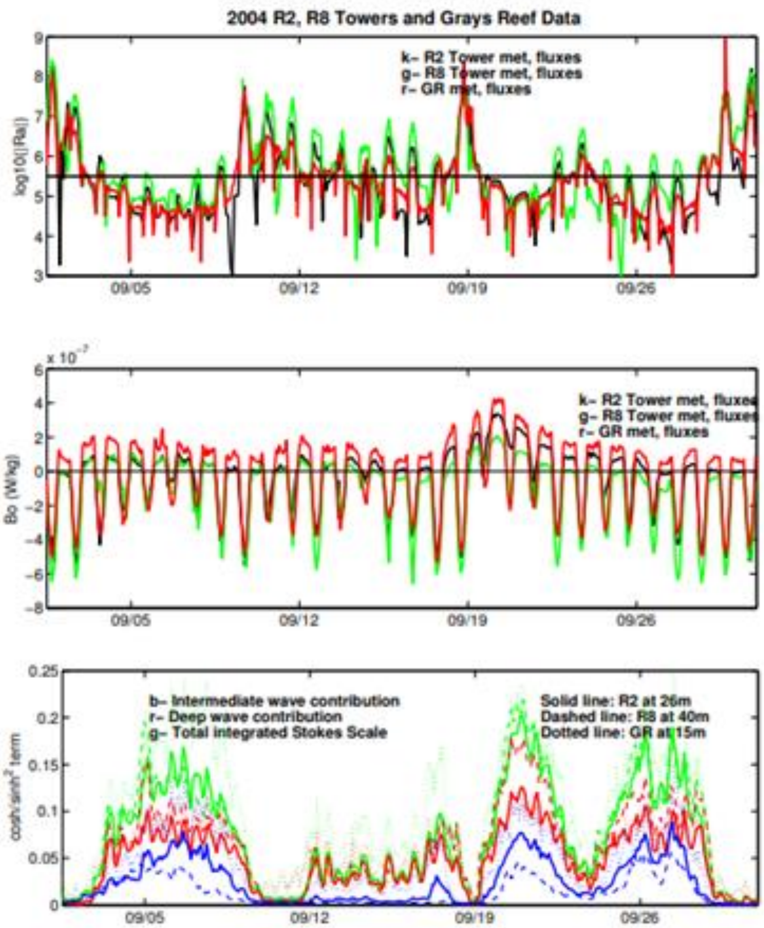


Figure 5.7: Diagnostics for September 2004 20 Hz using wave spectra from 2-hour subsets of 20Hz pressure records at R2 and R8. Upper panel shoes Ra values for R2, R8 and GR. Middle panels show $B_0$ (Surface buoyancy flux) values for the same locations. Lower panel shows wave contribution at the locations separated into deep wave, intermediate wave, and total contribution for integrated Stokes scale.

During September 2004, surface and bottom CTD data are available from R2 to assess stratification there, but not at Gray's Reef or R8. High full-water column backscatter at R2 and external diagnostics consistent with LSC also correspond to periods when the water column is unstratified.

At R8, high full-water column backscatter appears when *Ra* and $v_{si}$ both indicate possible LSC, but only when strong vertical shear in horizontal velocities disappears. This disappearance might arguably correlate with mixing of the water column and removal of stratification. Furthermore, the 6-minute average velocity fields at R2 and R8, when rotated into downwind coordinates, produce ordered velocity relationships consistent with the advection in wind-elongate cells past the ADCPs there, when averaged conditionally over 2-hour blocks (Fig. 5.8).

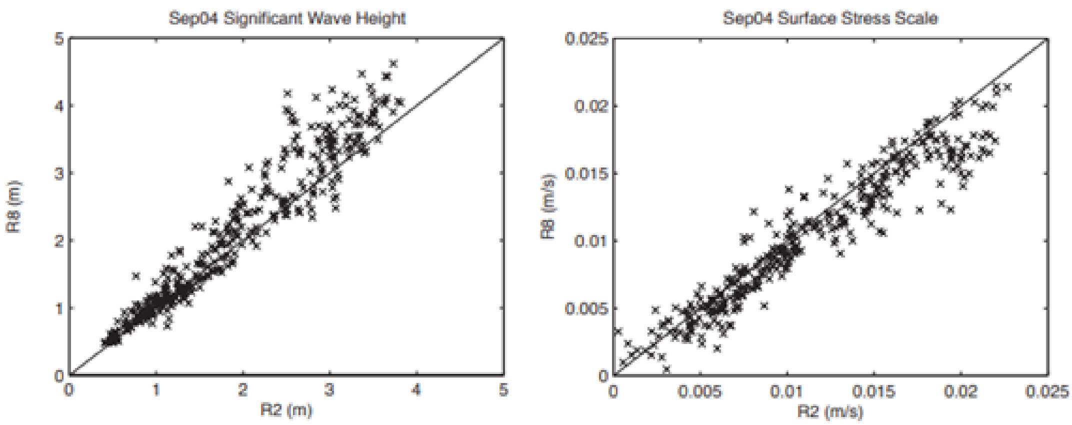


Figure 5.8: Comparison of winds and waves at towers R2 and R8 in September 2004. Left panel: R2 vs R8 significant wave heights from 2-hour subsets of 20 Hz pressure spectra. Right panel: R2 vs R8 surface stress scale from 2-hour subsets of archived 6-minute average data.

In cases where the *Ra* and $v_{si}$ calculated from the in-situ wind, buoyancy and wave data indicate LSC may exist at R2 and R8 in September 2004, one might reasonably expect LSC also to exist in shallower water at Gray's Reef. And indeed, the ECAD estimates of *Ra* and $v_{si}$ at Gray's Reef in 18 m water trace the R2 and R8 estimates reasonably well, suggesting LSC there are at the same time.

Finally, note that forcing of sufficient levels as assessed in the ECAD fashion at 18 m does not imply that LSC occur at 44 m depth at the same time. Rather, the implication is that it is reassuring for occasions when LSC are suspected at 44 m from local forcing data, that ECAD flux estimates from shallower water nearby also suggest likely LSC there are reassuring. Therefore, for sites with buoys at deeper depths, the ECAD method seems promising.

**CSP (2015)**

The ECAD method is used to examine the CASPER data in 40 m depth waters. During a short period in late September 2015, after the destruction of strong late summer stratification there, conditionally averaged wind aligned velocities during high wind and waves suggest full depth LSC (Fig. 5.9), as do a variety of other diagnostics calculated from the VADCP data.

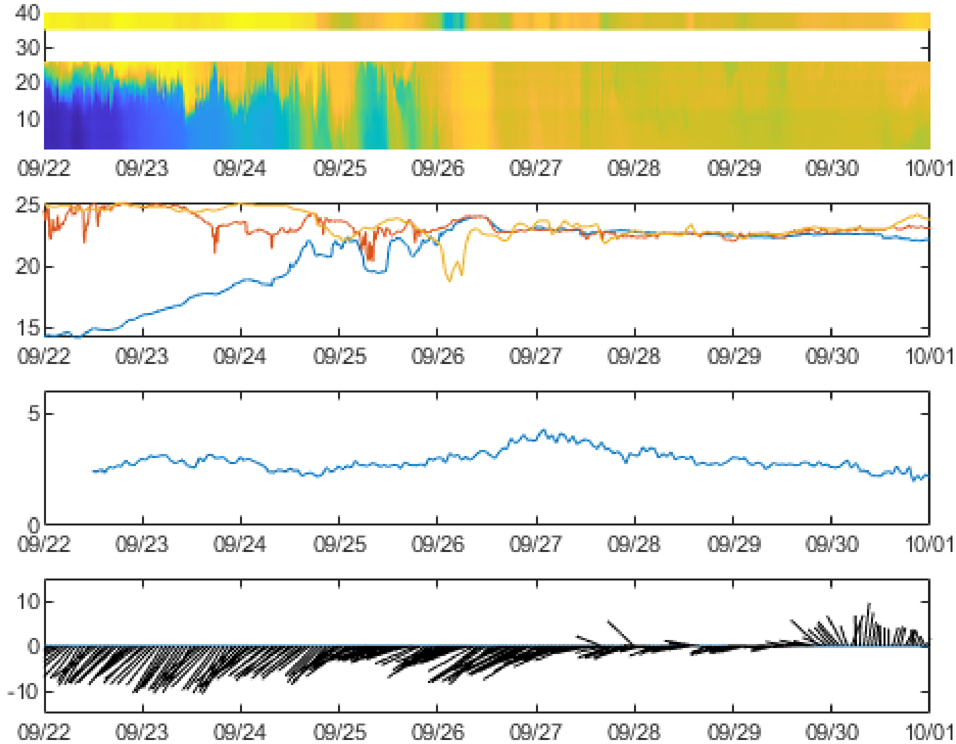


Figure 5.9: Auxiliary data from nearby buoys where events are likely present for CASPER dataset (September 22 to October 1st, 2015). From top to bottom, the graphs depict a) water temperature (Celsius); b) surface water temperature (yellow), bottom water temperature (blue), mean water temperature (red) (Celsius); c) sea surface wave height (m); d) wind speed and direction (m/s). Events are expected to happen when water becomes unstratified, when the wind is sufficiently strong and steady in direction, accompanied by an increase of surface wave height.

ECAD estimates of the forcing diagnostics are estimated from nearby NDBC stations 44014 and 41025. Ignoring periods during which the diagnostics would not be expected to apply, i.e., stratified conditions or unsteady wind direction (shaded), it is apparent that positive diagnostics correlate well with strong vertical velocities through the entire water column, as expected from LSC. In order to look at the forcing behind CSP prospective events, the heat flux and Rayleigh numbers were estimated with the ECAD method using satellite and nearby buoy auxiliary data (Fig. 5.10).

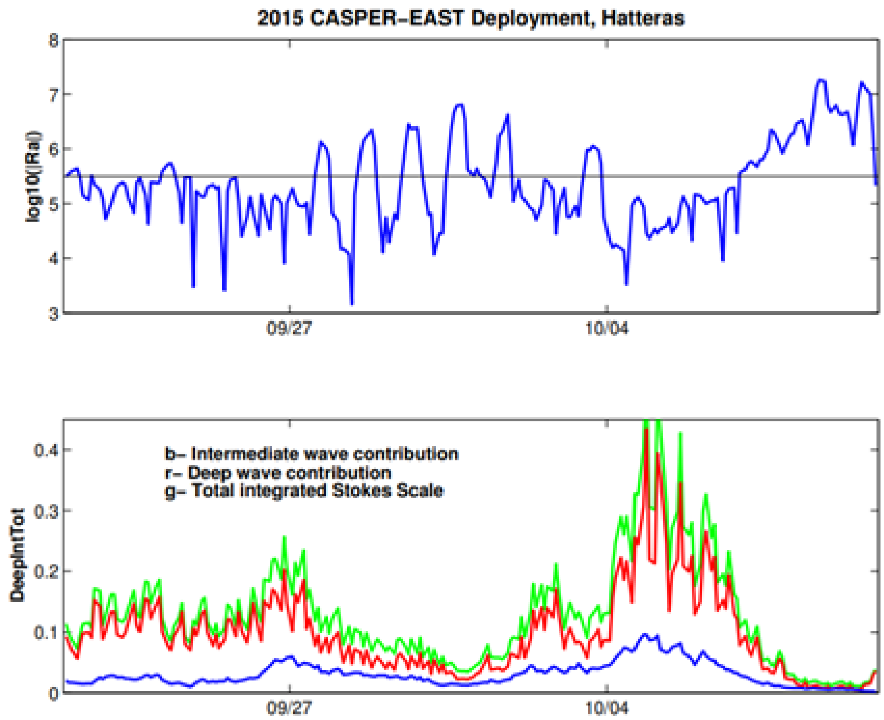


Figure 5.10: External diagnostics for October 2015, CASPER data session 301.

During periods of steady winds, unstratified waters, and intermediate wave type, *La* and *Ra* were estimated and plotted in regime diagrams (Figure 5.11). Convection and LSC archetypes presenting dissimilar structures, with LSC being wind elongated, while convection is horizontally isotropic, LSC events are associated with larger values of $\overline{\langle w'^2 \rangle}$, the depth-averaged variance of vertical velocity, than convection and are expected to fall within values of $\log_{10}(|Ra|) < 5.5$, and values of $\log_{10}(La) < -0.5$. All data points during these records fall within these thresholds.

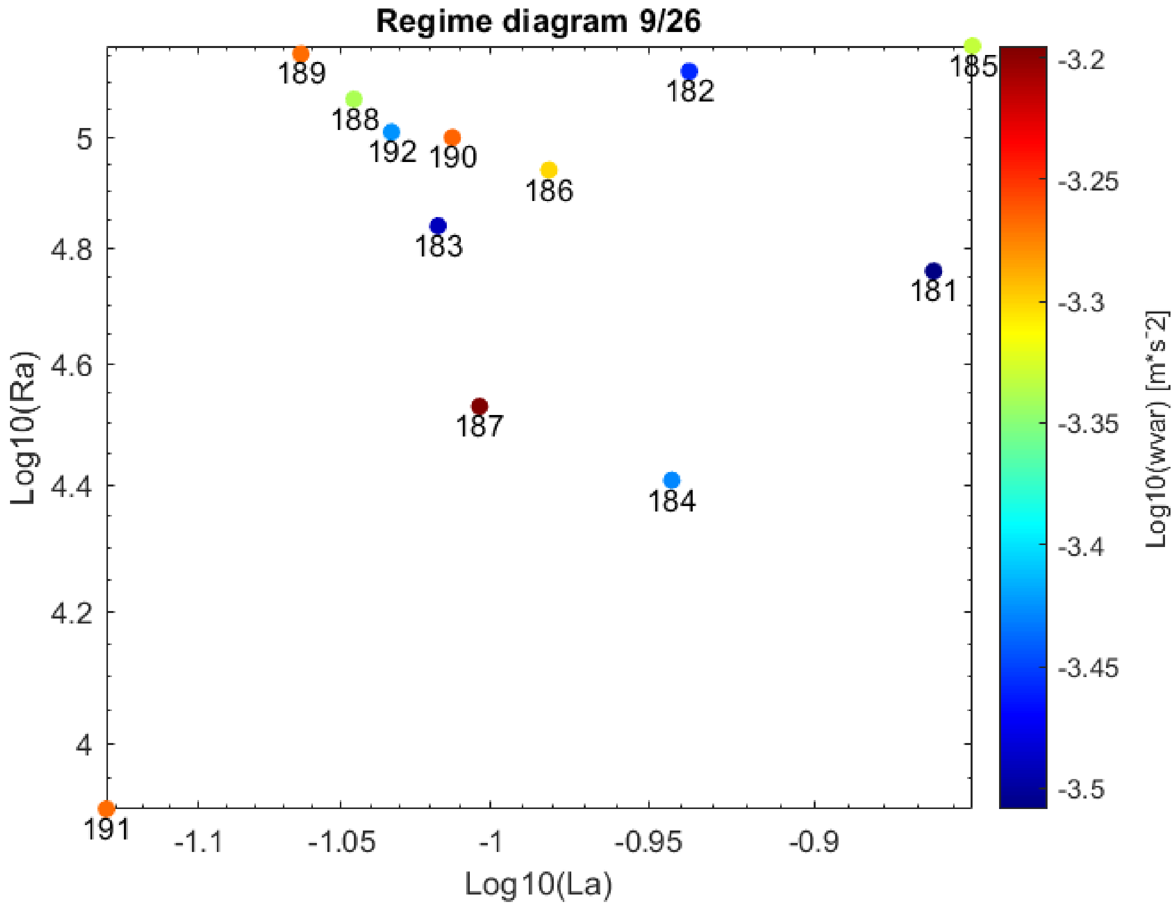


Figure 5.11: Distribution of records from 26 September 2015 at CASPER in a *Ra-La* regime diagram.

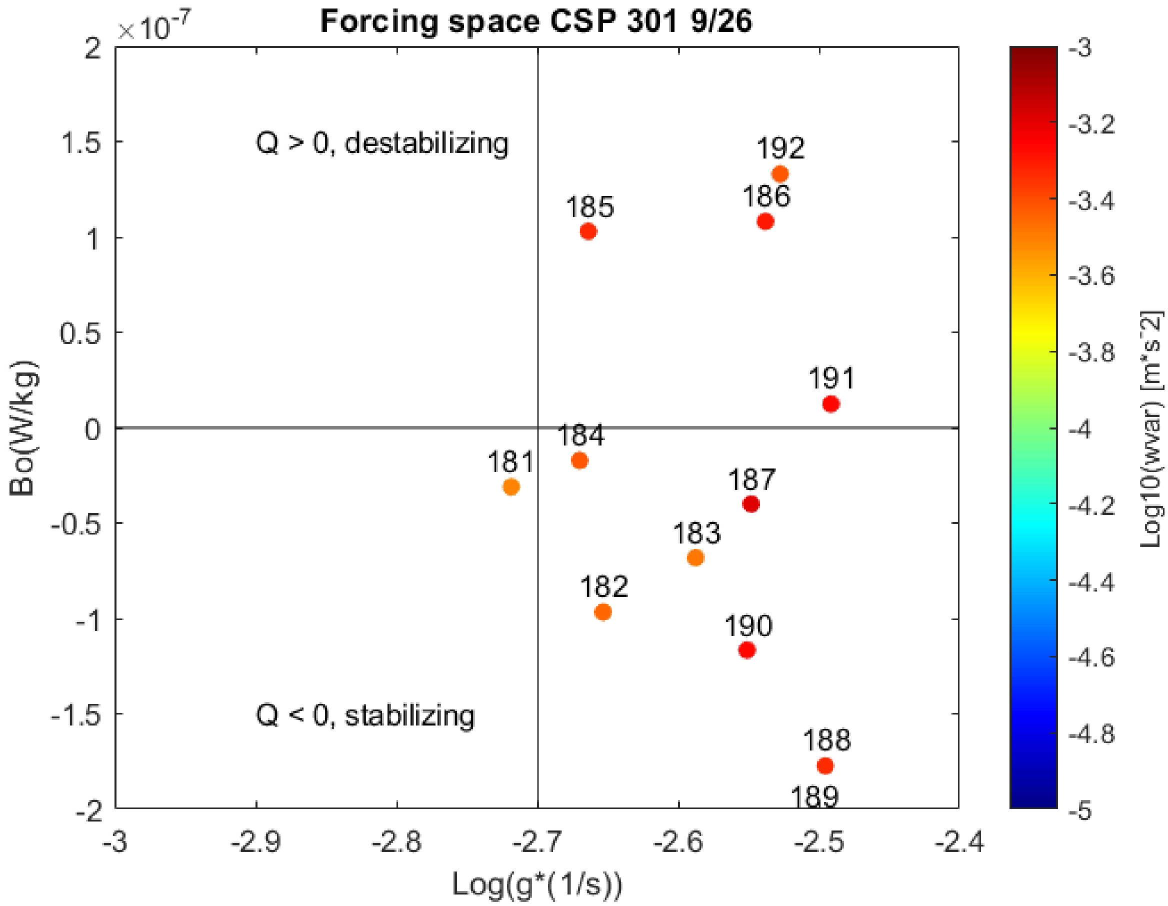


Figure 5.12: Distribution of records from 26 September 2015 at CASPER in a $B_0$-$g^*$ forcing space. Vertical reference like marks Langmuir forcing threshold for LSC and horizontal reference line separates buoyant stabilizing and destabilizing waters.

Following Gargett (2022), an alternative outlook is proposed using a forcing space instead of regime diagrams since the later may present issues relating to uncertainties in correction of Stokes surface velocity calculated from wave frequency spectra, the roughly constant nature of *La* in wind-forced wave conditions, as well as due to the definition of *La*, a small value for *La* can represent strong Stokes forcing, but it can also mean that wind stress is decreasing.

The proposed forcing space shows a competition between Buoyancy and Langmuir forcing represented by the parameters $B_0$ (surface Buoyancy flux) and log$10(g^*)$ (see Table 5.1). Using this proposed forcing space for the 26 Sep 2015 dataset (Fig. 5.12), values of $B_0$, fluctuating velocities, and $\log_{10}(g^*)$ all fall within the same range as the 2004 archetypal LEO event, as noted in Gargett et al. (2004), the event may occur in a small range of either stabilizing or destabilizing waters, though for the 2004 archetypal event, they vary within 1 and -1 W/kg, while for this CSP event, it varies from 1.5 to -1.5 W/kg.

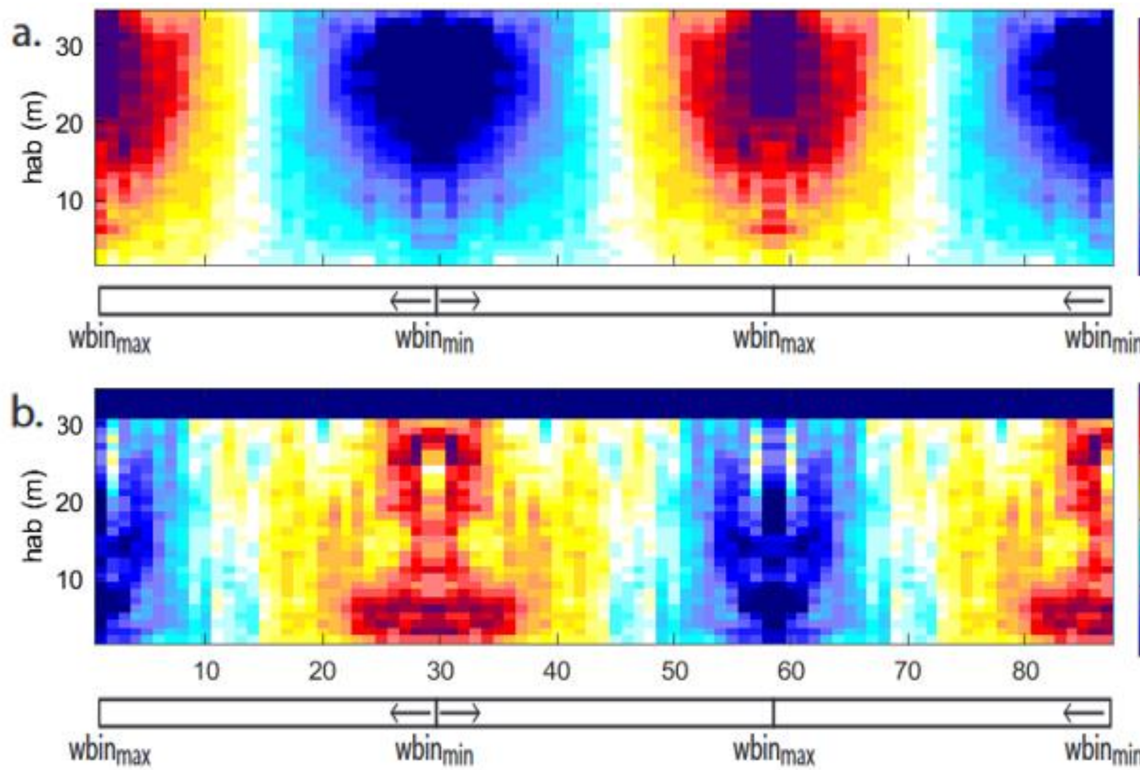


Figure 5.13: Fluctuating velocities conditionally averaged with respect to vertical fluctuating velocities during the 9/26/2015 CASPER event. Horizontal values for w' from 30 to 60 organized from highest negative $\overline{w'}$ (depth average) to highest positive $\overline{w'}$, mirrored in both directions to facilitate visualization; $\overline{u'}$ values are relative to $\overline{w'}$ at that time.

Another characteristic of LSC is the expected shift between vertical velocity fluctuations and downstream velocity fluctuations, i.e., downwind flow coinciding with downwelling limb of LC, upwind flow coinciding with upwelling limb of LC, with downwelling branches converging near surface and diverging near bottom, and conversely, upwelling branches diverging near surface and converging near bottom. Considering the simplest theoretical LSC event, the case of wind-parallel velocity, a downwelling feature is associated with enhanced downwind velocity, and an upwelling feature is associated with diminished downwind velocity fluctuations. As expected, for CASPER prospective LSC events, negative vertical velocity fluctuations are strongly correlated with high positive downstream velocity fluctuations, and positive vertical velocity fluctuations are correlated to high negative downstream velocity fluctuations (Fig. 5.13).

## 5.4 DISCUSSION

Several caveats are necessary for the analyses considered here. First, at all three VADCP deployment locations, the wave frequency band did not overlap with the frequency band occupied by the turbulent response in the velocity fields. Therefore, simple filtering was sufficient to assure that in water velocity-based turbulence diagnostics were not biased by wave energy. This will not necessarily apply in other locations where VADCPs may be deployed, hence requiring other methods to remove wave bias (Kirincich and Rosman, 2011; Chapter 4 herein). These datasets provided an excellent opportunity to develop these methods.

Second, provisional diagnostics calculated over half-hour, hourly or two-hourly data-subsets were all consistent, verifying that the two-hour increments provided stable statistics, and resulted in both relatively consistent forcing over those periods, and the sampling of circulation response over sufficient numbers of turbulent structures. That is, the size of Langmuir cells and the rate at which they drifted past the VADCP, depending on tides or other low-frequency mean velocities, provided adequate sample size during sequential two-hour periods. This may also not universally apply; stability of estimates over a range of sample lengths should be explored in every dataset.

Third, the method used to estimate cloud coverage based on SST is a very rough and subjective evaluation of how much of the day the site may have experienced cloud cover and it could be refined with higher temporal or spatial resolution SST imagery than the Rutgers daily composite used herein.

For the September 2004 events, pressure-based regime diagrams from R2 and R8 are similar to each other (Fig. 5.14), and to those estimated for September 2007 with VADCP-derived wave (Fig. 5.7). In each case, there are occasions when forcing is expected to be dominated by the Langmuir vortex force. Two-hour records where bottom stress calculated from pressure exceeds the mobilization threshold of silt (gray - 60 microns), sand (black - 388 microns) and medium sand (green - 505 microns, like those dominating sediments at R2 (Nelson et al., 1999) are shown. When forcing is sufficient that full depth LSC can be expected, the wave field can also be expected to have mobilized sediments, as coincident high wind, wave and full-water column backscatter events recorded at the shelf edge during SABSOON suggest.

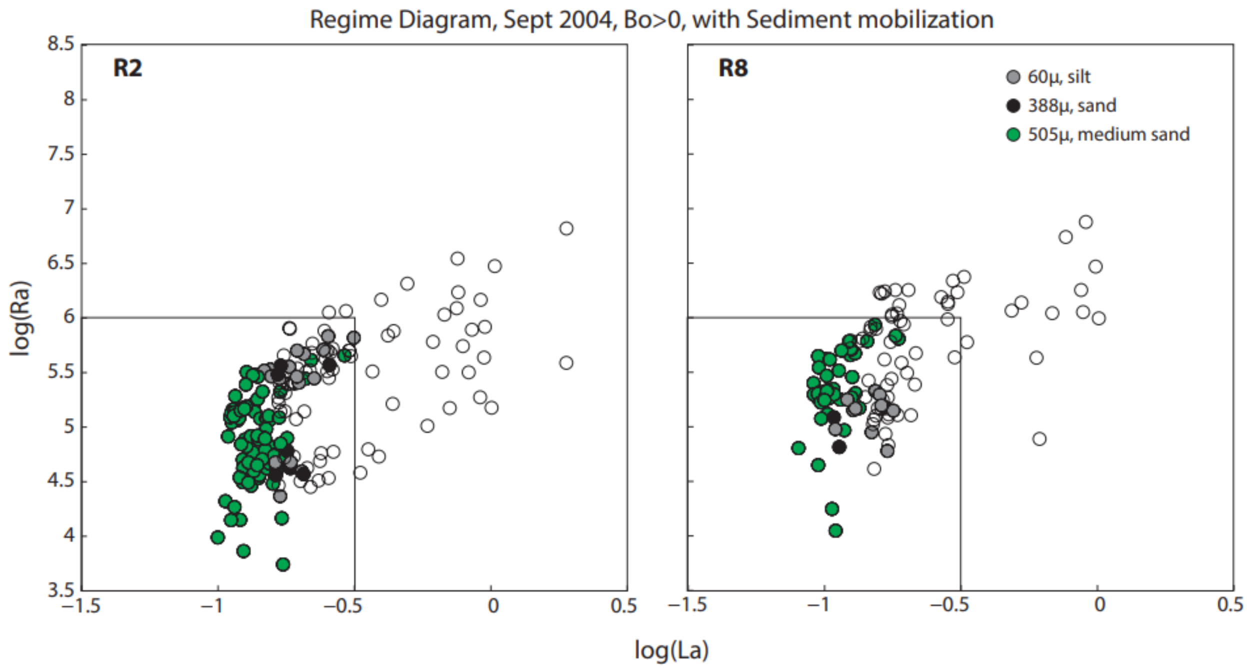


Figure 5.2: Regime plots for Sept 2004, including high wind wave and full water column backscatter events. *La* is estimated at the surface. *Ra* is calculated at 0.2H below the sea surface using pressure gauge wave spectra. Bottom stress magnitude calculated from pressure is color-coded for two hour record values exceeding the mobilization threshold of silt (gray - 60 microns), sand (black - 388 microns) and medium sand (green - 505 microns). Boxes in the lower left corner of each panel where $\log_{10}(La) < -0.5$ and $\log_{10}(Ra) < 6$ indicate conditions when the Langmuir vortex force is expected to be dominant.

For the September 2015 event off of Duck, the nearest NDBC meteorological towers were more distant from the VADCP than the SABSOON packages located on the Navy towers off Georgia. Moreover, these NDBC buoys do not record the shortwave and longwave radiation data needed to estimate surface ocean heat fluxes. The ECAD method described herein was used alongside auxiliary data from nearby NDBC buoys 44014 and 41025 to estimate heat flux for the CASPER data set. Despite the saturation of backscatter intensity in the bottom of the water column, all other diagnostics such as constant wind, waves of intermediate type, destratification of water column, and high vertical velocity fluctuations of in-situ and external measurements reveal LCS events at 40 meters depth. Regime diagrams and forcing space showed that during this period values for *Ra* and *La* fell within the parameters' thresholds for LS, and Langmuir forcing dominated over convection.

## 5.5 CONCLUSION AND FUTURE WORK

The ECAD method proposed herein for calculation of missing longwave and shortwave radiation data by estimating cloud coverage with SST imagery and buoy data is presented as an alternative for the lack of pyranometer data. Sensible and latent heat fluxes for buoy 41008 were similar to the values measured at towers R2, R6, and R8. Small differences in longwave measurements between the methods were inconsequential in establishing LSC parameters. A weakness of the proposed ECAD method lies in a significant difference in shortwave estimation compared to pyranometer measurements, which should be compensated by diminished shortwave radiation into the ocean and diminished longwave radiation out of the ocean during high cloud cover associated with strong storms (periods in which LSC events are more likely due to increased wind and waves). Ultimately, the ECAD method at buoy 41008 and the measurements from tower R2 and R8 showed notable agreement for positive total heat flux values, while negative heat flux values suffered from poor shortwave estimates. This shortcoming does not pose a problem when looking at the forcing space during LSC events, since Langmuir forcing seems to dominate and generate the familiar vortex structures in either stable or unstable heat flux conditions.

Intermediate wave character predominates during high wind and wave events at tower R2 in 26 *m* depth water, when the 3D circulation and stress profile diagnostics show LSC, similarly to what is observed in LEO. Equivalent VADCP measurements of the 3D oceanic circulation response to storm forcing do not yet exist at deeper locations in the coastal ocean, with the exception of the CSP dataset presented herein. Intermediate wave character on the outer GA shelf at 40 m depth occurs during high wind events. During such events, the destratification of waters due to mixing make it possible that LSC may occur, leading to resuspension of sediments beyond the bottom BL. Regime diagrams indicate the dominance of vortex forcing, which suggests that even at the shelf edge, the dominant oceanic response to high wind and wave events will be Langmuir cells, apparently also reaching the bottom.

# CHAPTER 6

# ORGANIZATION OF LANGMUIR SUPERCELLS AT VARYING DEPTHS

## 6.1 INTRODUCTION

Significant wind speeds (greater than 3 m/s) with relatively constant direction in time may lead to wave-current interaction of sufficient strength to generate Langmuir circulations (LC), which manifest as pairs of counter-rotating vortices oriented approximately downwind. While LC have been historically observed in the deep ocean and lakes, recent attention has been paid to LC events occurring on continental shelves, which under sufficiently strong winds and wave conditions may erode stratification and reach the bottom boundary layer (BBL; Gargett et al., 2004). LC that comprises the full water column are called Langmuir Supercells (LSC), which are an important mechanism of sediment resuspension and transport in shallow coastal waters. However, our understanding of these events and their impact on coastal regions is still not fully developed.

LSCs have been observed in shallow coastal waters ranging from the archetypal event discussed in Gargett et al. (2004), in 16 m deep, weakly stratified waters off the coast of New Jersey, in 26 m waters depth off the Georgia coast (Savidge and Gargett, 2017), and in 40 m water depth off the coast of North Carolina (Chapter 5). Events in the 16 m depth waters were observed to have higher organization compared to the events in 26 m waters (Savidge and Gargett, 2017); however, the relationship between organization and depth for LSC is still an open question.

Organization of LSC is defined as LSC whose forcing are sufficiently strong to maintain the archetypal LSC structure as described in Gargett et al. (2004). These highly coherent structures are able to move wave-mobilized sediment out of the BBL (Savidge and Gargett, 2017). However, while the same forcing parameters may generate an organized LSC event in shallower waters (i.e., 15 m depth as in Gargett et al., 2004) in deeper waters, LCS appears less organized over water depth (i.e., 26 m as in Savidge and Gargett 2017 or 40 m as in Chapter 5). Consequently, current coastal models that generate LSC events may fail to properly capture LSC structures in deeper regions.

Following the definition of organization of LSC, a method to quantify the organization of events was proposed by calculating organization scores (Gargett and Savidge, 2020). This method seemed useful when comparing LSC events, however, it failed to separate coherent structures generated from the Langmuir forcing versus buoyancy forcing (Gargett, 2022). Gargett (2022) identified locations in a forcing space displaying competition of Langmuir and buoyancy forcing. While organizational scores failed to identify if an event was convection or LSC, it was observed that the turbulent shear stress $\langle -u'w' \rangle$ recorded values near zero during unstable convection throughout the water column, and as conditions moved in the forcing space away from convection, towards Langmuir forcing, $\langle -u'w' \rangle$ increased.

These two methods of estimating organization maybe used in tandem. Turbulent shear fluctuations $\langle -u'w' \rangle$ can be estimated to characterize if the counter-rotating roll vortices are generated by convection or LSC. Then, the organization of structures identified as LSC can be estimated using organizational scores.

Herein, I use these methods discussed and further described in the Data and Methods section to estimate and compare organization of LSC across three different sites in 16 m, 26 m, and 40 m depth waters. Isolating periods across sites when LSC are present, allows us to better understand differences that may rise due to difference in depth alone, since variables such as stratification levels and wind-wave alignment are usually the same when conditions for LSC are met (wind-wave alignment for a significant amount of time, and waters becoming unstratified). I will use these comparisons to examine the role of depth in the development and organization of LSC.

LSC have been identified from ADCP data when backscatter originated from the surface and bottom boundary layer appears when waters are unstratified, with regime diagram values within a parameter range of non-dimensional numbers discussed in the following section (Gargett and Grosch, 2014), which implies dominance of Langmuir vortex forcing in the production of turbulence over shear and buoyancy forcing. Also, waves must be able to "feel" and interact with the bottom boundary layer, which requires the wavefield to be of intermediate type. All LSC events analyzed herein fulfill all the requirements for LSC identification.

## 6.2 DATA AND METHODS

Observational data are from three separate bottom-mounted VADCP (5-beam) deployments at different sites with different depths and conditions. In 2003, the first deployment was off the coast of New Jersey at the LEO-15, a site established by the Middle Atlantic Bight National Undersea Research Center as part of the Long-term Ecosystem Observatory (Gargett et al., 2004; Gargett et al., 2014), henceforth referred to as LEO. A second deployment was mounted at Navy Tower R2 on the Georgia mid-shelf in 26 m depth waters, in 2007 and 2008, as part of the Benthic Observatory and Technology Testbed On the Mid Shelf – Understanding Processes (BOTTOMS-UP) project, herein referred to as BUP (Savidge et al., 2008; Gargett et al., 2014). In the Fall of 2015, a third deployment was mounted in 39 m depth waters of the coast of Duck, NC, as an extension of the Coupled Air-Sea Processes and Electromagnetic Ducting Research (CASPER). The VADCP and associated T-chain parts of the overall project are referred to as CSP in this work. The instrumentation, characteristics, and available auxiliary data are described below. Described below are the instruments and characteristics of each site.

**LEO**

Approximately 6 km off the coast of New Jersey, a VADCP was mounted at the B node (39 27.69' N, 74 14.68' W) of the LEO-15 cabled ocean observatory. The VADCP recorded velocity profiles roughly from 25 April to 31 October 2003. The vertical beam provided measurements of vertical velocity ($w$) from about 1 meter above bottom (mab) to the sea surface, with local resolution of 0.4 m. Slant beams provided standard estimations of horizontal velocity components ($u$,$v$). Velocity data were continuously sampled at 1 Hz and returned as sequential records of about 2.4 hr length, a period sufficiently short that forcing conditions and water depth were often found to be constant.

Atmospheric auxiliary data necessary to quantify forcing of surface-layer turbulence at LEO were obtained from a meteorological tower located on the beach shore roughly 6 km west of the tower. Tower wind speed and direction measurements are highly correlated to those of nearby buoy (Münchow and Chant, 2000). A bottom mounted CTD recorder at the B node of LEO-15 provided sporadic temperature and salinity profiles. During storms, however, CTD was suspended to avoid risk of tangling the tether.

**BUP**

The second deployment was part of the BOTTOMS-UP project (Savidge et al., 2008), imbedded in the SABSOON (Seim, 2000) observatory on the Georgia continental shelf. A 600

*Hz* RDI VADCP was deployed near Navy tower R2, 65 km east of St. Catherine's Island, GA, in 27 m depth waters. This instrument recorded beam velocity profiles through the water column, with all 5 beams synchronized and sampled at 1 Hz. The bin size was 0.95 m starting from 1.6 mab. Full water column stratification was monitored using a thermistor chain. Sea surface currents and wave fields were monitored by a shore-based Wellen Radar (WERA) high-frequency radar network. The bottom two bins were discarded for analysis as the VADCP did not sample the lower boundary layer well, and the top two bins showed interference from vertical beam side lobes.

A data acquisition system (DAS) package mounted on the R2 tower at 50 m above surface supplied auxiliary meteorological data, as part of the Atlantic Bight Synoptic Observatory Network (Seim, 2000) Instruments in the package operated continuously and recorded average values over 6 minutes and was comprised of an R.M. Young anemometer for wind speed and direction, Rotronics relative humidity and air temperature sensors, IntelliSense barometric pressure, and Eppley shortwave and longwave radiation sensors. Auxiliary data also included internally recording Onset Hobo T sensors arranged on a T-chain, which provided 5-minute averaged temperature data through the water column.

**CSP**

For all deployments, processing steps included identification of the sea surface level in the fifth vertical beam backscatter, elimination of data at that level and above in the vertical beam. Slant beams were oriented 25° from the vertical, so elimination of slant beam data was necessary in the top 9 % of water column, where it would be contaminated by side-lobe pickup of the surface. VADCP backscatter from the fifth beam has been corrected for beam spreading and absorption, but not calibrated to the size or concentration of reflectors in water column. A fish identification algorithm was used along each beam to flag data contaminated by the presence of fish (Gargett and Wells, 2007). Short temporal gaps were filled by fitting 2$^{nd}$ order polynomials vertically in each beam. Turbulent velocity fluctuations are extracted from larger velocities associated with surface waves by low-pass filtering. Backscatter saturation occurred in some occasions when recorded intensity exceeded 70 dB, at which point backscatter intensity in these situations were omitted. Meteorological auxiliary data was obtained from nearby NDBC buoys 44014 (36.609 N 74.842 W) and 41025 (35.010 N 75.454 W), which were used to estimate heat flux using the ECAD method (Chapter 5) to assess buoyancy forcing.

For all datasets, measured parameters such as velocity and fluctuations are rotated into a wind-aligned coordinate system. For the LEO dataset, session 043 will be analyzed, as it contains the archetypal LSC event which will be used as a reference for other LSC events. For the BUP dataset, sessions 001 and 023 will be used, as LSC events with different forcing conditions have been observed there. Lastly, for CSP, session 301 will be used, as two LSC events with seemingly different forcing take place during that session.

**Regime diagram and forcing space**

Turbulence production in the oceans is often the result of multiple distinct forcing acting on the flow. When determining the presence of LSC, it is important to know what forcing dominates turbulence production to assess if the observed turbulent structures are indeed LSC. Wind stress can act directly over the surface of the ocean generating turbulence through shear, or indirectly through its effect on the surface waves. Another important possible source of turbulence production in the upper ocean is the buoyancy forcing, which, through convection, can affect water stability and compete with wind-wave forcing as observed in the TKE budget equation (Kitaigorodskii and Lumley, 1983; Polton and Belcher, 2007):

$$0 = -\overline{u'w'}\frac{\partial \bar{U}}{\partial z} - \overline{v'w'}\frac{\partial \bar{V}}{\partial z} - \overline{u'w'}\frac{\partial U_s}{\partial z} + \overline{w'b'} - \frac{\partial}{\partial z}\left(\overline{w'E'} + \frac{1}{\rho}\overline{w'p'}\right) - \in, \tag{6.1}$$

where $u$,$v$,$w$ are respectively the downwind, crosswind, and vertical velocity components, $\rho$ is the density, $\overline{u'w'}$ and $\overline{v'w'}$ are Reynolds stresses, and comprise the effects of shear in the mean current and production due to Stokes shear, $\overline{w'b'}$ is the turbulent buoyancy flux, which denotes production and destruction of turbulence due to buoyancy forcing, $\overline{w'E'}$, the turbulent energy flux, and, $\overline{w'p'}$ the pressure work flux, which together represents transport of TKE due to turbulent fluctuations; and ∈ is the dissipation rate due to molecular viscosity.

Regime diagrams are often used to show the parameter field of two non-dimensional numbers, which is useful when assessing dominant forcing in turbulence production. Historically, Langmuir supercells have been studied in a buoyancy vs Langmuir vortex forcing regime diagram. The former is usually represented by the Hoenikker number (Li and Garrett, 1995) or the Rayleigh number (Gargett and Grosch, 2014). The latter is usually represented using Langmuir number ($La$), or turbulent Langmuir number ($La_t = \sqrt{La}$), defined as a ratio of destruction over production of turbulence due to Langmuir vortex effects of Stokes forcing acting on the wavefield.

*Ra* and *La* are used in the regime diagrams herein, derived using Equations 6.2 and 6.4:

$$Ra = \left(\frac{\alpha_T g}{k_T}\right)(Q t_*^2), \tag{6.2}$$

Where $\alpha_T$ is the coefficient of thermal expansion, $g$ is the acceleration of gravity, $\kappa_T$ is the thermal conductivity, $Q$ is the surface heat flux, and $t_*$ associated with the growth time of LC in an unstratified sheared fluid (From appendix Gargett and Grosch, 2014, derived from Leibovich, 1977):

$$t_* \equiv \left(\frac{dU_S}{dx_3}\frac{dU}{dx_3}\right)^{-1/2}, \tag{6.3}$$

And the Langmuir number is defined as:

$$La \equiv \left(\frac{u_*}{u_{S_0}}\right), \tag{6.4}$$

where $U_S$ is the Stokes velocity, $U$ is the mean velocity, $u_*$ is the surface stress velocity, $u_{S_0}$ is the surface stokes velocity, and $x_3$ is vertical distance with positive upwards from the water surface.

Gargett (2022) however, described a few shortcomings of using a regime diagram associated with uncertainties in estimating $U_{S0}$, the fact that *La* is roughly constant in wind-forced conditions in the ocean, and due to the nature of scaling parameters (i.e. a sharp decrease in $U_{S0}$ followed by a decrease in shear velocity, $u^*$, would at first reveal an increase in *La*, which in that case would not imply an increase in Stokes forcing).

To address these shortcomings, both in regime diagrams and forcing space, an alternative proposed in Gargett (2022) uses a parameter field of more directly understandable dimensional forcing parameters. The first parameter is surface buoyancy flux, $B_0$, computed from the surface heat flux Q as shown in Equation 6.5:

$$B_0 = g\alpha Q/\rho C_v, \tag{6.5}$$

where, $\alpha$ is the thermal expansion coefficient of seawater at surface, and $C_v$ is the specific heat of seawater at constant volume. The second parameter in the forcing space is the LC growth rate $g^* = {t^*}^{-1}$, associated with the timescale, $t^*$,used as a measure of wind-wave forcing (Gargett and Grosch, 2014).

Values of $log_{10}(g^*)$ above the critical value of -2.7 represent Langmuir forcing associated with full depth structures (Gargett and Savidge, 2020). Values on the left hand-side of the forcing space may represent times when turbulent structures associated with convection appear, while values in the right hand-side of the forcing space are associated with dominating Langmuir forcing. Vertical velocity fluctuations appear to increase from lower to higher values of $g^*$. Values of $B_0$ are positive out of the water, and are associated with destabilizing stratification, while negative values of $B_0$ are stabilizing.

A structure found in the examined datasets will be considered a Langmuir Supercell if it possesses all expected characteristics of an LSC (wind-wave alignment, unstratified waters, wave of intermediate type, bottom, and top origin backscatter, etc.), while appearing in the expected regions for LSC in both the regime diagram and forcing space.

**Shear fluctuations method to identify convection or Langmuir Structures**

Gargett (2022) shows that shear turbulent stress fluctuations $\langle -u'w' \rangle$ time averaged over a record can be used as a tool to identify if observed large-eddy turbulent structures within that record are a product of convection or Langmuir forcing. For all observed events of the LEO dataset, $\langle -u'w' \rangle$ was near zero when convection was the dominating forcing, and it increased with increasing Langmuir forcing reaching much higher positive values for full depth Langmuir structures.

Values of $\langle -u'w' \rangle$ for each record are estimated following Gargett (2022). Time averaged $\langle -u'w' \rangle$ is averaged over depth from the near bottom bin through the last bin before potential surface origin sidelobe effects could contaminate slant beam data used to estimate *u'*. The stress metric described above serves to quantify qualitative changes in organization of turbulent velocity fields, as it increases from convection to LSC.

### Organizational scores

When comparing Langmuir Supercell events, it is useful to quantify structural organization. Herein, the method for estimating organizational scores proposed in Appendix B of Gargett and Savidge (2020) is followed. The goal of organizational scores is to determine how close the full-depth turbulent velocity field of a given Langmuir Supercell event compares to the archetypal LEO 043 Langmuir Supercell event described in Gargett et al. (2004). The major features of the archetypal well-organized LSC event are as following:

1. Downward vertical velocities regions coincide with enhanced near-bottom downwind velocity fluctuations, and conversely, upward vertical velocity regions coincide with negative near-bottom downwind velocity fluctuations.
2. Near-bottom crosswind velocities change signs at approximately the center of the downwelling/upwelling limbs of the LSC structure.

Since both major features are accentuated near bottom, *u* and *v* values from the bottom 5 meters of the water column are used for the estimates described henceforth. Organization scores are quantified for each downwelling and upwelling during a record by how closely observations match the features described above, then the record is assigned an organizational score equal to the averaged organizational scores of each downwelling and upwelling during the record. This method however is somewhat flawed as turbulent structures dominated by convection in the presence of mean downwind shear could produce characteristics similar to the major features of LSC (Gargett, 2022).

Once LSC are identified, instrument data is rotated into a wind-aligned coordinate system, and shear fluctuations indicate that turbulent structures are a result of Langmuir forcing, I estimate organizational scores. A Hanning window is used to smooth data for each record in time (6 min) and vertically (three bins). Then the velocity field is rotated to wind coordinates, where $u$ is aligned downwind, and $v$ is positive to the left of the wind.

The vertical velocity field is averaged over depth to produce a time series $\overline{w}$, which can be plotted over the velocity field. In the example shown, it can be noted how both major features described above are present. Points where $\overline{w}$ changes sign are estimated to identify when each downwelling and upwelling started and ended.

For each of the major features described, an organizational score correlated with that feature is calculated for each downwelling/upwelling interval:

1. A uscore of 1 is assigned to an interval if the time averaged downwind velocity during that interval $\langle u \rangle$ is positive in case of a downwelling interval, or negative in case of an upwelling interval. Else, the interval is assigned a uscore of 0.
2. A vscore of 1 is assigned to an interval if the time averaged crosswind velocity during that interval $\langle v \rangle$ changes sign between ¼ and ¾ of the length of the interval (as a perfectly centered change in sign might be a rare occurrence due to tilt with depth).

Each record is assigned a Uscore equal to the average uscore of all its intervals, and a Vscore equal to the average vscore of all its intervals. Typical archetypal LSC events present records with Uscore > 0.6, and Vscore > 0.3. The method described above to quantify structural organization of turbulent structures is somewhat flawed as turbulent structures dominated by convection could produce characteristics similar to the major features of LSC (Gargett, 2022). To account for that, shear fluctuations are estimated as described in the previous section to separate cases of convection generated structures from LCS structures.

Shear turbulent stress fluctuations will be used to confirm structures are not formed due to convection, in such cases, with forcing values pointing towards Langmuir forcing, organizational scores Uscore and Vscore can be used to estimate structural organization of full depth LSC.

Further, a comparison between both estimates of organization can be made. While $\langle -u'w' \rangle$ may be a good way to separate convection from LSC, Uscore and Vscore might still be the better method to quantify organization once an LSC is identified as an observed turbulent structure that is not generated due to convection. If $\langle -u'w' \rangle$ matches organizational scores, then shear fluctuations would be a much simpler and direct way to estimate organization than Uscore and Vscore.

## 6.3 RESULTS AND DISCUSSION

### LEO 043

A forcing space of the Archetypal LSC event at LEO is used to illustrate a clear distinction between records dominated by convection and those dominated by Langmuir forcing leading to LSC (Fig. 6.1). On the left side of the forcing space, records present lower vertical velocity fluctuations, and convection dominates turbulence production. As Langmuir forcing increases, so does the Langmuir growth rate $g^*$ and vertical velocity fluctuations also increase. When $g^*$ exceeds the critical threshold of $log_{10}(g^*) = -2.7$, LCS structures can appear (Gargett and Grosch, 2014).

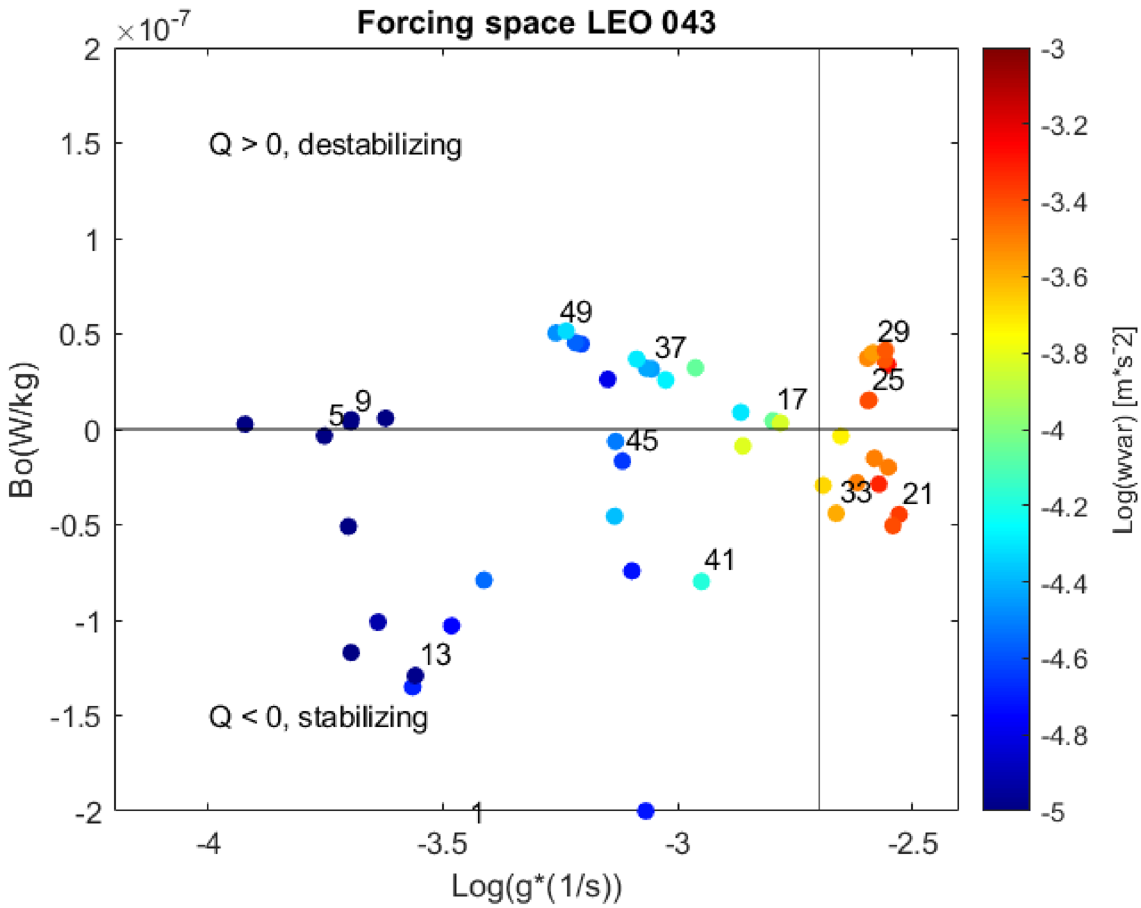


Figure 6.1: Forcing Space for LEO 043 dataset, numbers northeast of circles denote record number, horizontal vertical line separates regions of stabilizing waters ($Q < 0$) and destabilizing waters ($Q > 0$), vertical reference line marks threshold for appearance of LSC ($log_{10}(g^*) = -2.7$).

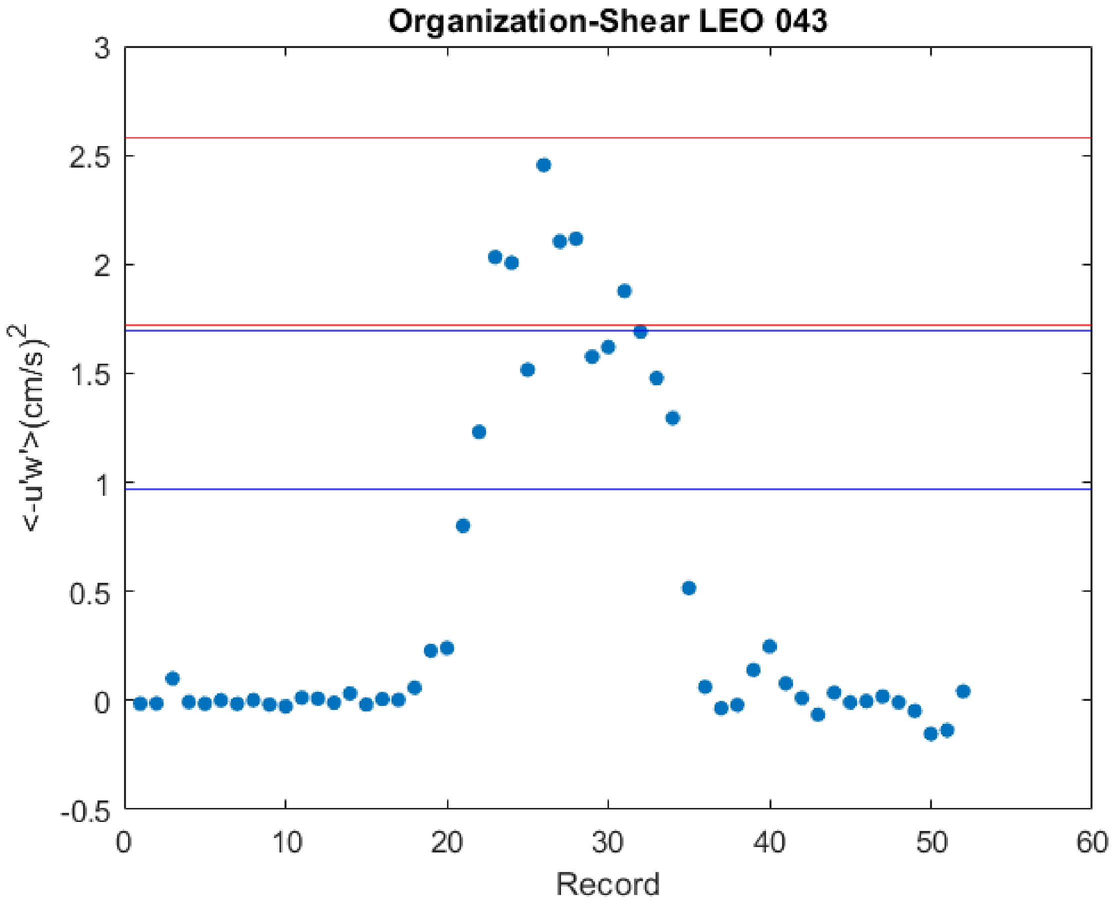


Figure 6.3: Shear turbulent stress fluctuations for LEO 043. Blue reference lines denote values for records near or above critical $g^*$, and red reference lines denote values for records with $\log_{10}(g^*)$ between -2.6 and -2.4, like the archetypal LSC records in LEO 043.

Estimates of shear fluctuations show that during records dominated by convection, values of $\langle -u'w' \rangle$ are near zero (before and after LCS events), with increasing $\langle -u'w' \rangle$ as wind-wave forcing adds turbulence to the system, reaching its maxima during the LCS event (Figure 6.2). This trend agrees with analysis of Gargett (2022), and a similar trend is expected from LCS events at deeper sites.

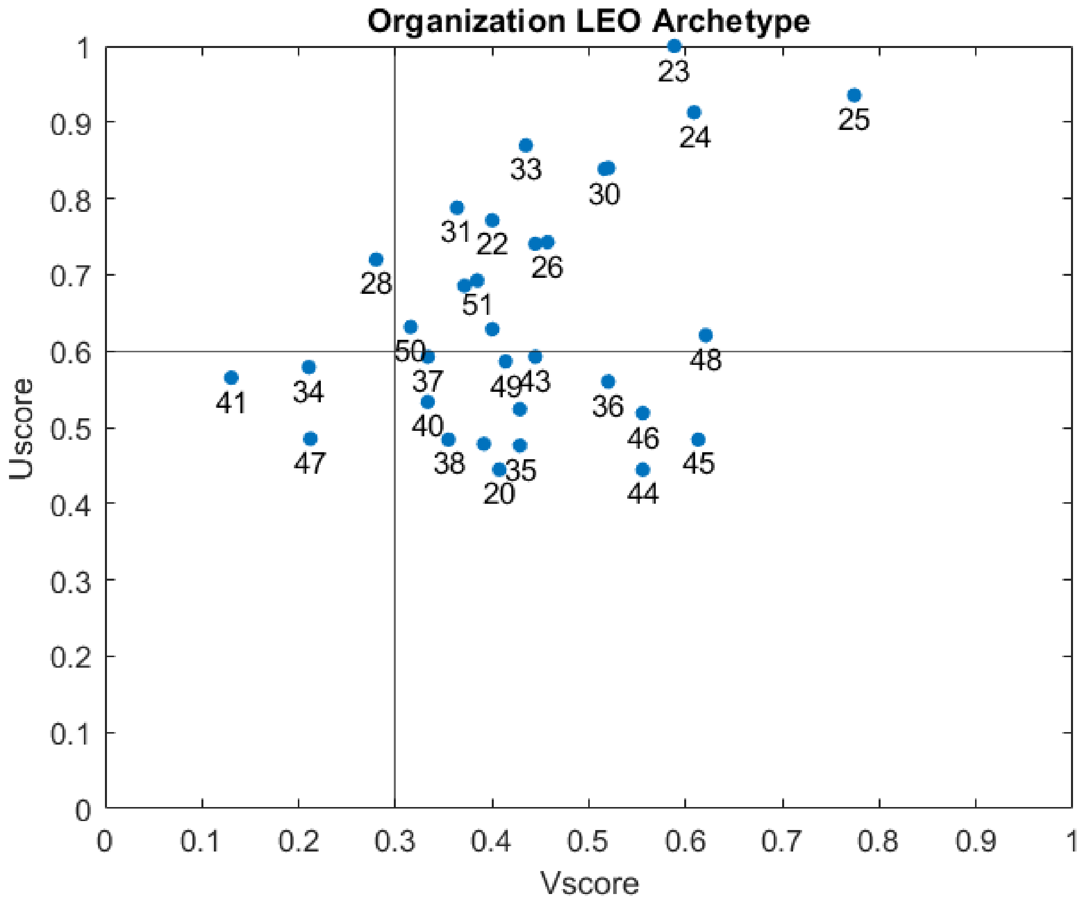


Figure 6.4: Organizational scores for LEO 043, reference lines marks threshold set in Gargett and Savidge (2020) for organized LSC records.

Organizational scores for the LEO 043 archetypal event are relatively high, and most records during the event exceed the threshold for organized events (Fig. 6.3). The average Uscore and Vscore for this event also passes the suggested threshold for organized events (Table

6.1). Events at deeper sites are expected to present lower organizational scores as orientation of LSC changes with depth (McWilliams et al., 1997; Yan et al., 2022).

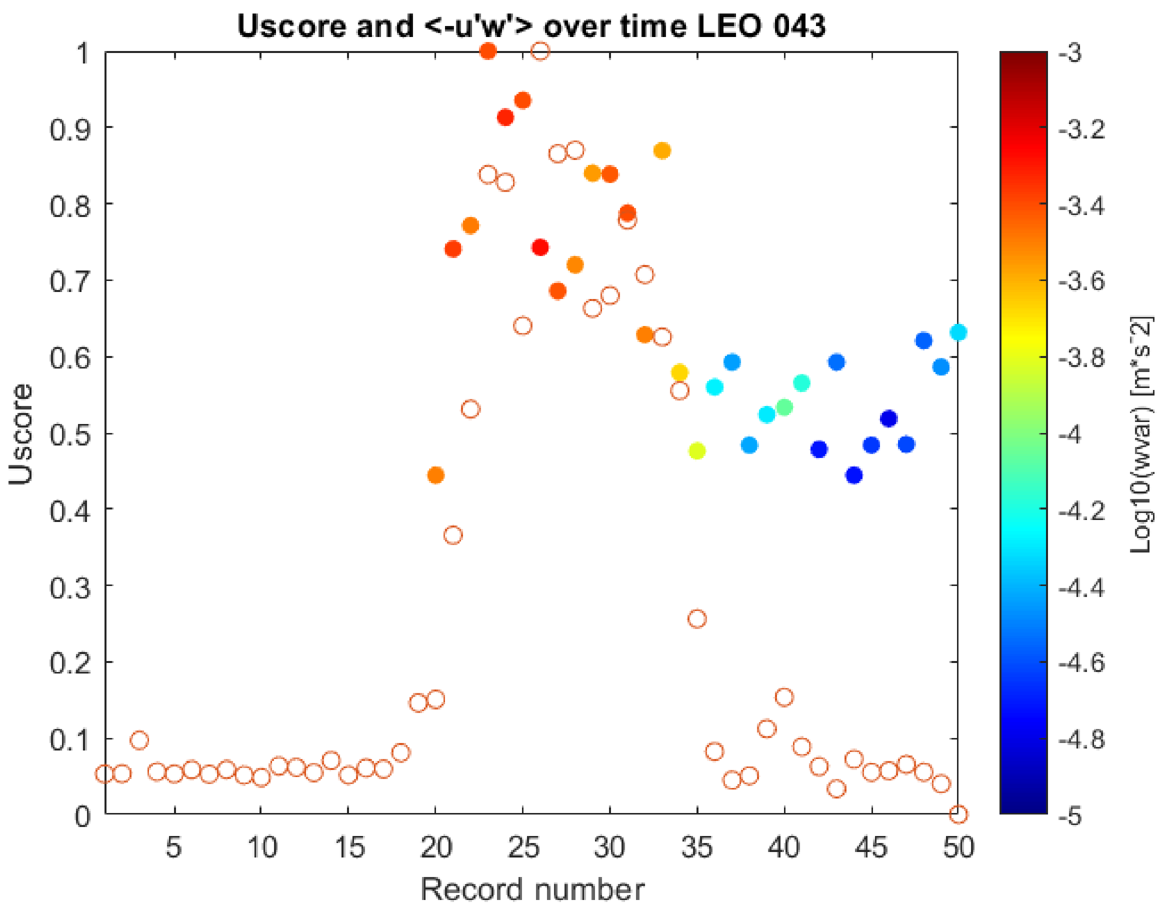


Figure 6.5: Downwind organizational scores (Filled – vertical velocity fluctuations) and scaled shear turbulent fluctuations (empty) over time for LEO 043.

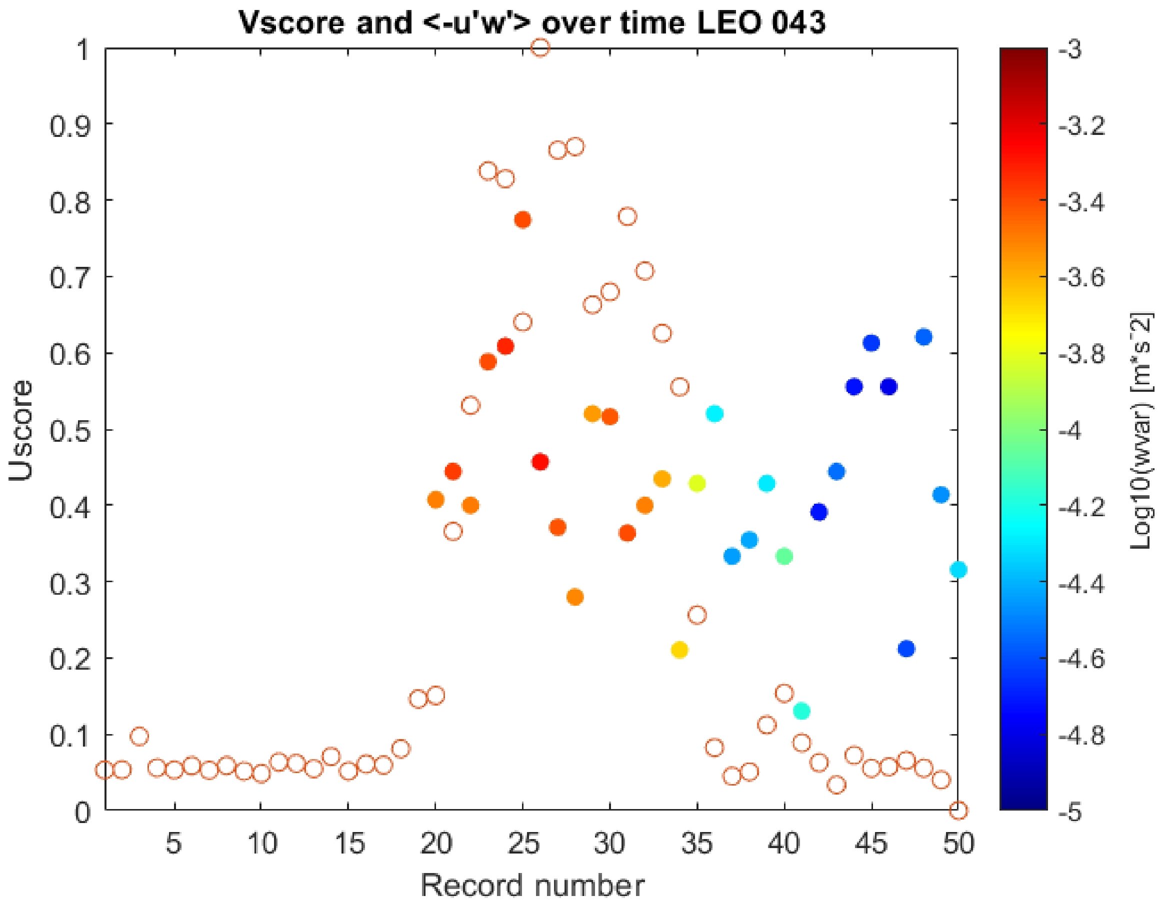


Figure 6.6: Crosswind organizational scores (Filled – vertical velocity fluctuations) and scaled shear turbulent fluctuations (empty) over time for LEO 043.

As the event starts, with increased Langmuir growth rate, organizational scores (both Uscore and Vscore) and $\langle -u'w' \rangle$ both increase. Organizational scores and shear turbulent stress fluctuations reach a maximum during records 23, 24, and 25 (records with highest organizational scores), followed by a decrease of these same parameters as the event peters out and $g^*$ drops below LSC threshold (Fig. 6.4 and 6.5).

For an organized event such as the one during LEO 043, organizational scores may be redundant with $\langle -u'w' \rangle$, as the latter not only presents similar progression during the event, with the advantage of being near zero when Langmuir growth rate is sufficiently low. This relationship, however, seems to only appear during simple short events, as this behavior could not be replicated for events taking place during multiple days or during the passage of a tropical storm. A possible explanation for the behavior could be the very definition of the first major feature of LSC structures that vertical fluctuations coincide with opposite sign downwind fluctuations yields a high Uscore.

**BUP 001 and 023**

Forcing space of two distinct events at BUP are shown to illustrate how organization of LSC events at the same site may vary depending on forcing conditions. The first, BUP 001, discussed in depth in GS20 contains an LSC event which occurred during the passage of tropical storm Barry, which heavily affected forcing conditions at the site due to increased winds and waves, as well as a sudden change in wave direction as the eye passed (Fig. 6.6).

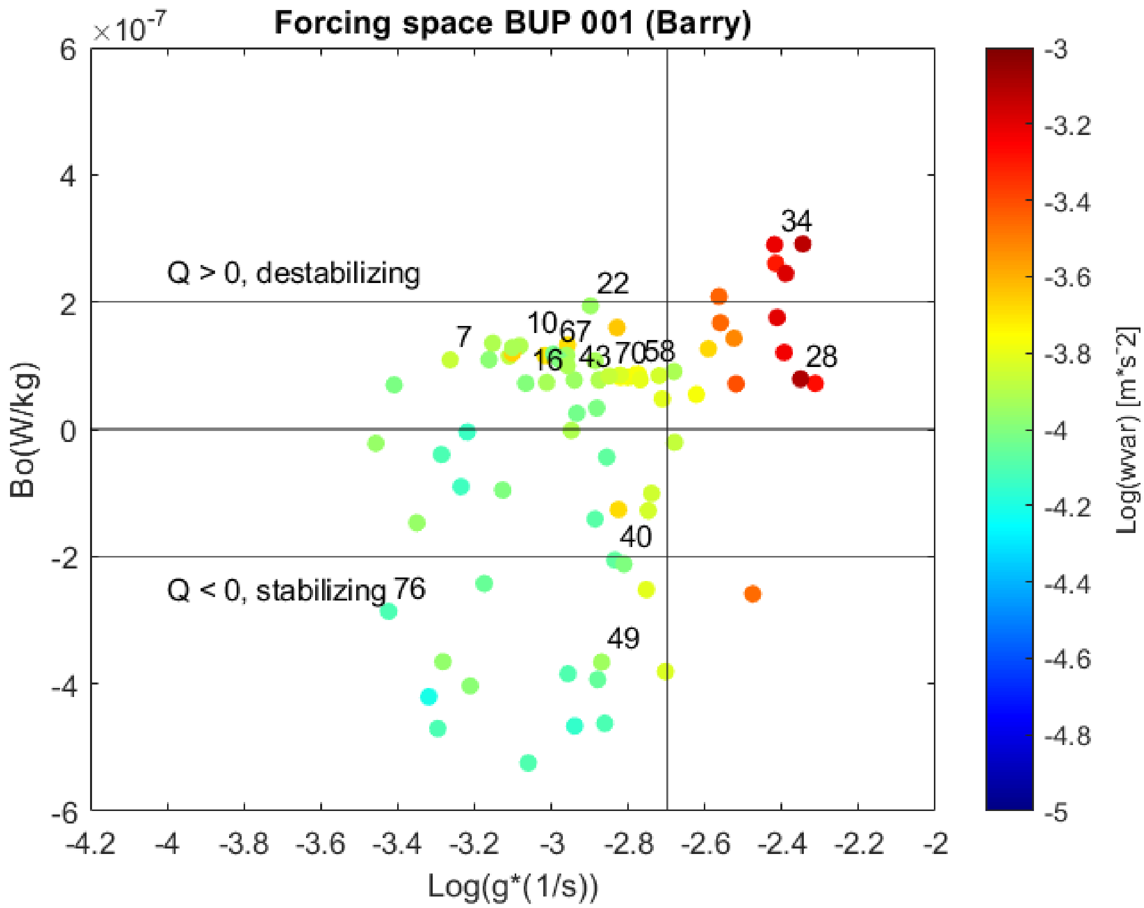


Figure 6.7 Forcing space for BUP 001 dataset, numbers northeast of circles denote record number, horizontal vertical line separates regions of stabilizing waters ($Q < 0$) and destabilizing waters ($Q > 0$), vertical reference line marks threshold for appearance of LSC ($log_{10}(g^*) = -2.7$).

Records with strong wind-wave forcing and $g^*$ above the critical threshold for LCS (Fig. 6.6), allows for identification of records which could present full depth Langmuir structures. Records below $g^*$ threshold present higher vertical velocity fluctuations and are more spread out in the forcing space compared to those of LEO 043, which is likely due to the added effects of tropical storm Barry. It is of note that $g^*$ during this event reach greater values than those observed in LEO 043.

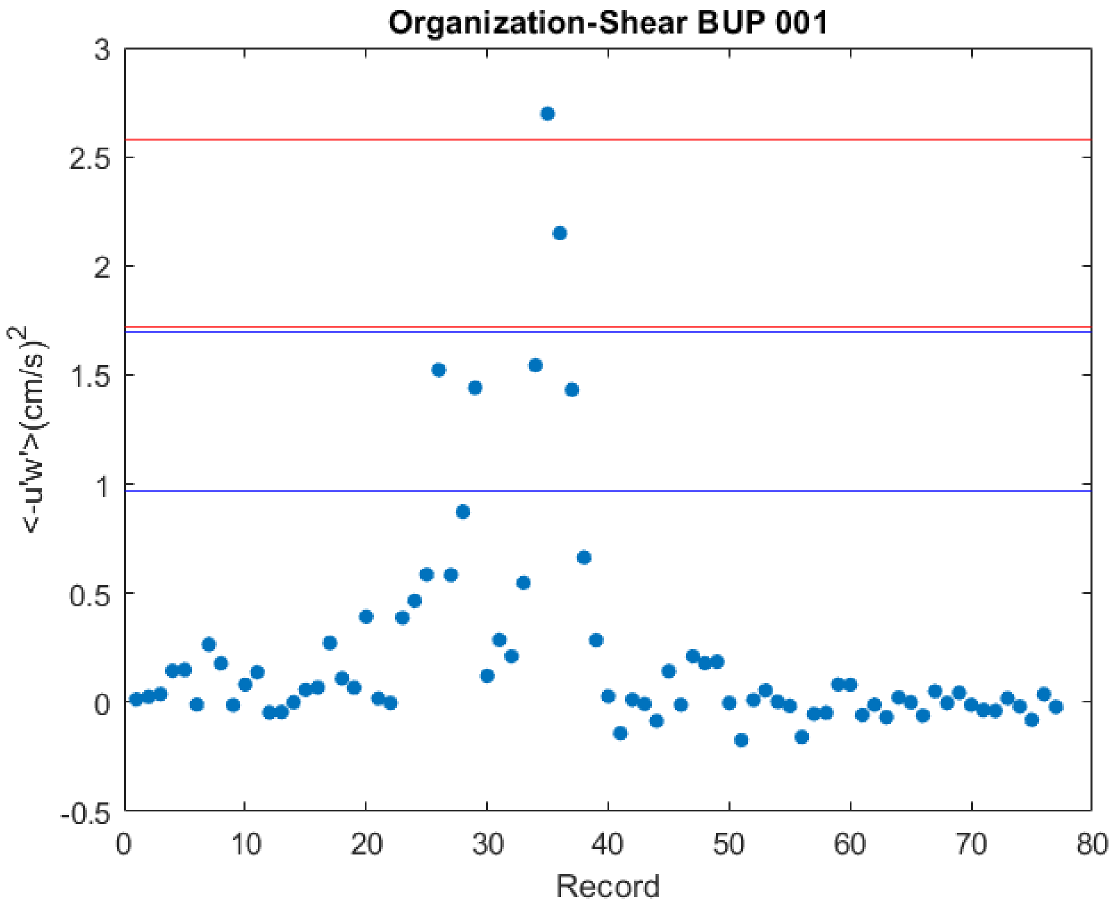


Figure 6.8: Shear turbulent stress fluctuations $\langle -u'w' \rangle$ for BUP 001. Blue reference lines denote values for records near or above critical $g^*$, and red reference lines denote values for records with $\log_{10}(g^*)$ between -2.6 and -2.4, like the archetypal LSC records in LEO 043.

Shear fluctuations for this event follow a similar trend to what was observed for LEO 043, with near zero $\langle -u'w' \rangle$ values before and after the event, when convection dominates turbulence production, and maximum $\langle -u'w' \rangle$ during full LCS event (Fig. 6.7), peak $\langle -u'w' \rangle$ values is also greater than that of LEO 043.

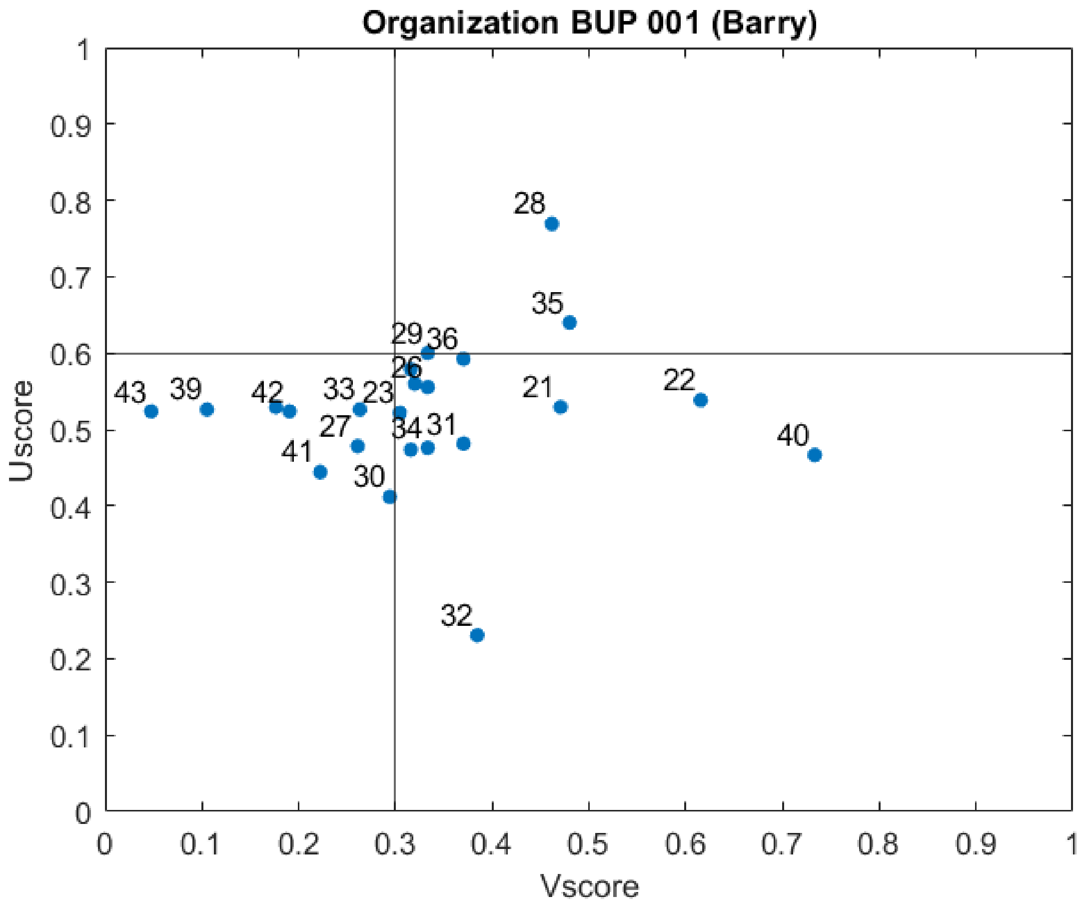


Figure 6.9: Organizational scores for BUP 001, reference lines marks threshold for organized LSC records.

Organizational scores for BUP 001 are observably lower than those of the archetypal LEO 043 (Fig. 6.8). Only records 28 and 35 present organizational scores above the threshold for organized LCS structure (both Uscore > 0.6 and Vscore > 0.3), records noted in Gargett and Savidge (2020) to be near the respective peaks of wind forcing during the passage of tropical storm Barry, when locally forced waves increase in magnitude and decrease in frequency.

Despite achieving higher $g^*$ and higher shear fluctuations than LEO 043, organizational scores are overall lower.

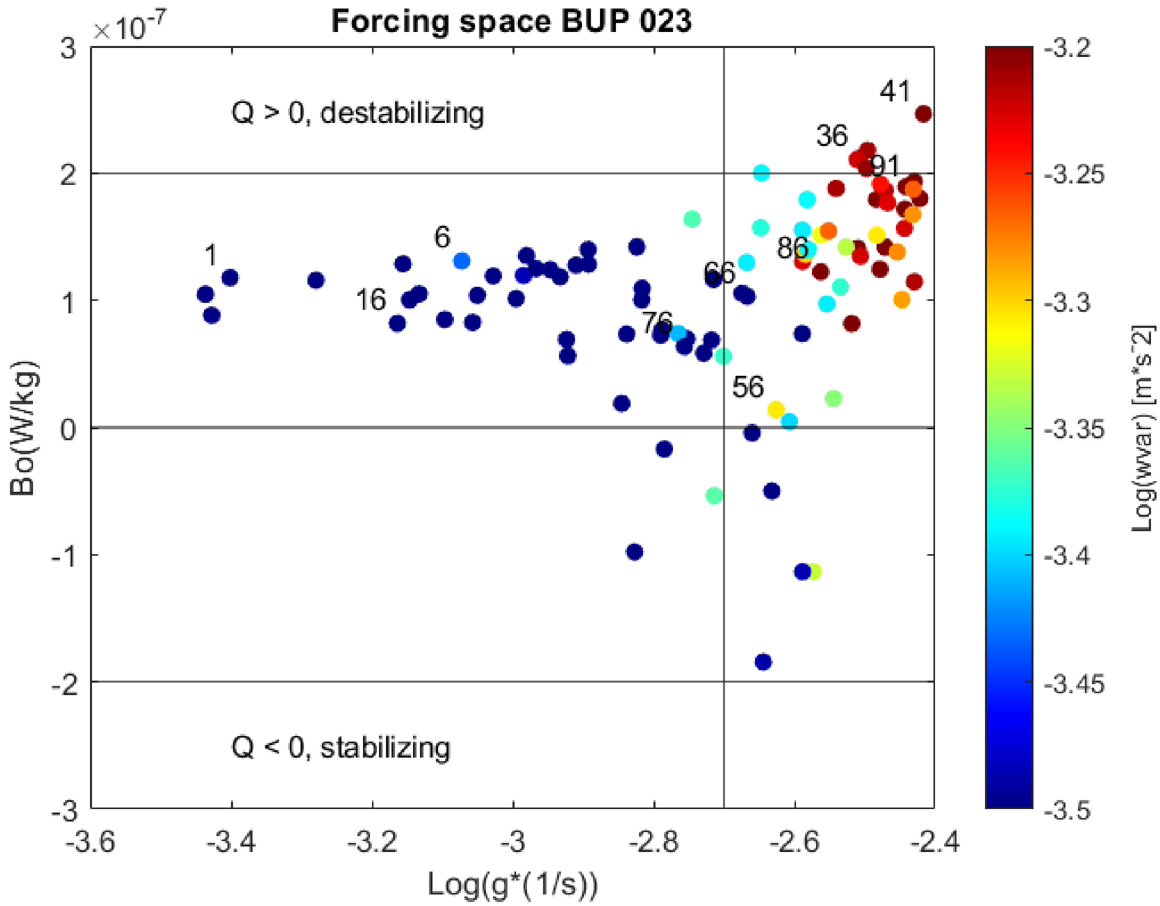


Figure 6.10: Forcing space for BUP 023 dataset, numbers northeast of circles denote record number, horizontal vertical line separates regions of stabilizing waters ($Q$ < 0) and destabilizing waters ($Q$ > 0), vertical reference line marks threshold for appearance of LSC ($log_{10}(g^*) = -2.7$).

Another full depth LSC event at BUP occurs in BUP 023 and presents more traditional parameters for this site (Fig. 6.9). The Langmuir growth rate threshold value for LCS is reached in two different occasions, between records 30 and 60, and in records 80 and above, with the former presenting higher vertical velocity fluctuations.

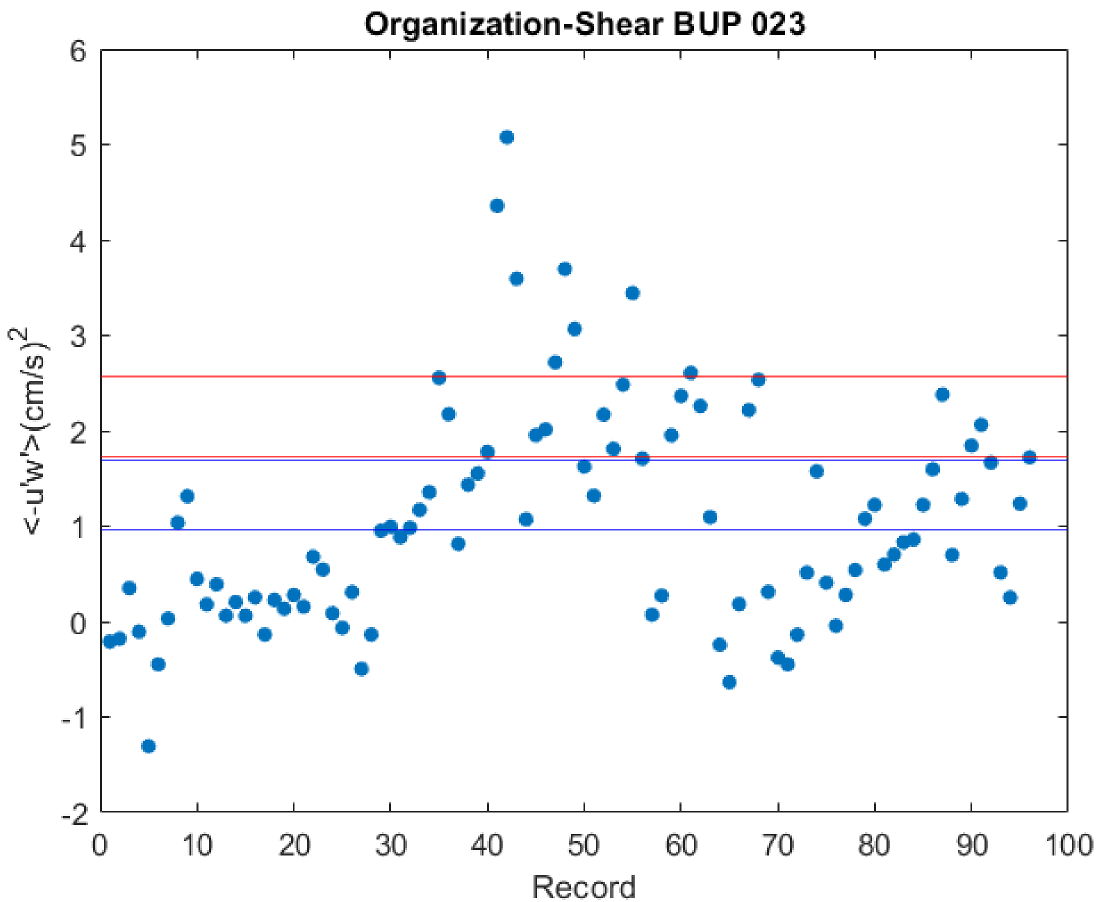


Figure 6.11: Shear turbulent stress fluctuations $\langle -u'w' \rangle$ for BUP 023. Blue reference lines denote values for records near or above critical $g^*$, and red reference lines denote values for records with $\log_{10}(g^*)$ between -2.6 and -2.4, like the archetypal LSC records in LEO 043.

Contrary to what is observed in other events, shear fluctuations $\langle -u'w' \rangle$ are near zero only in a few instances, and it fluctuates through the record length reaching values much greater than what is observed for LEO 043 and BUP 001. However, peak values for $\langle -u'w' \rangle$ are still achieved when $g^*$ passes the threshold for LCS (Fig. 6.10).

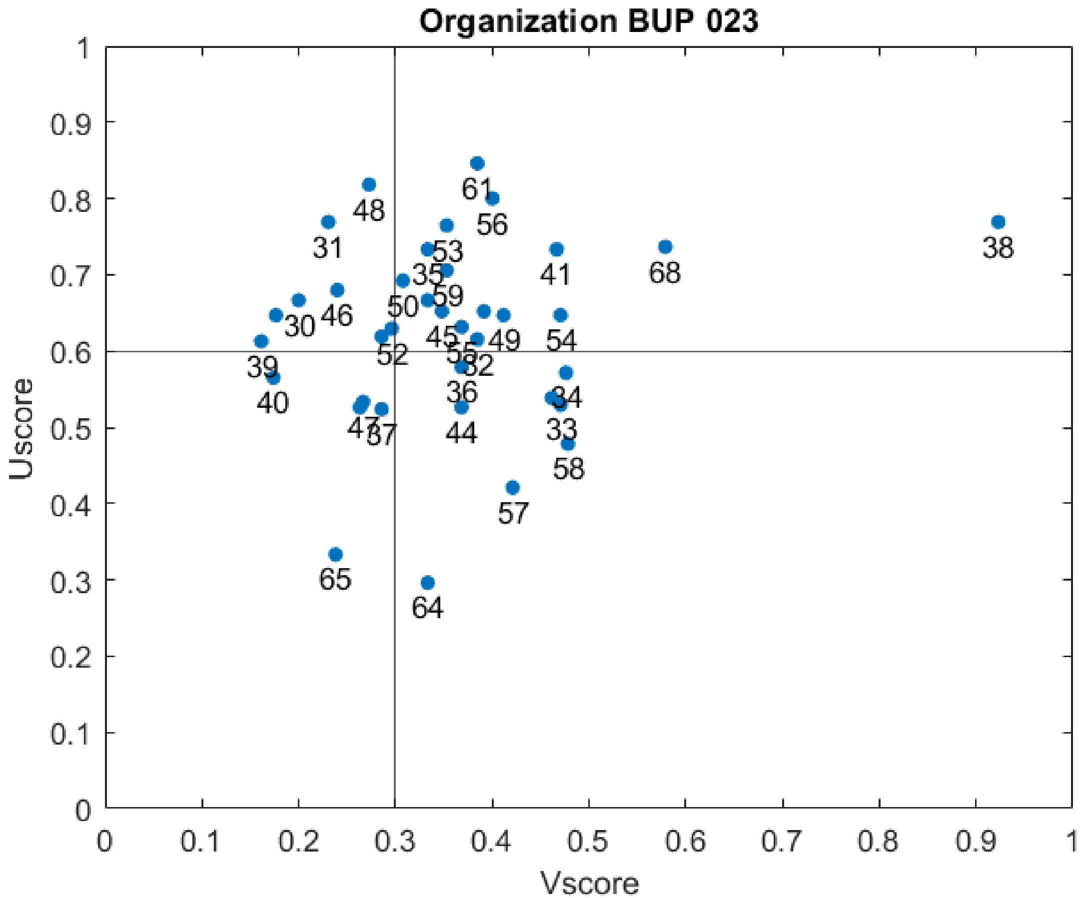


Figure 6.12: Organizational scores for BUP 023. Reference lines marks threshold for organized LSC records.

Organizational scores for BUP 023 are decidedly greater than for BUP 001. However, organizational scores are still below those of LEO 043, despite BUP 023 presenting much greater values for $\langle -u'w' \rangle$ (Fig. 6.11).

**CSP 301**

The question then becomes whether LCS events at deeper sites can maintain structural organization or not. Two LCS events found in CSP 301 (Chapter 5) at 40 m depth are evaluated to answer the question above, the first one occurred in later September of 2015, the later occurred in early October of 2015, and they will be referred herein as CSP 301 September, and CSP 301 October events, respectively.

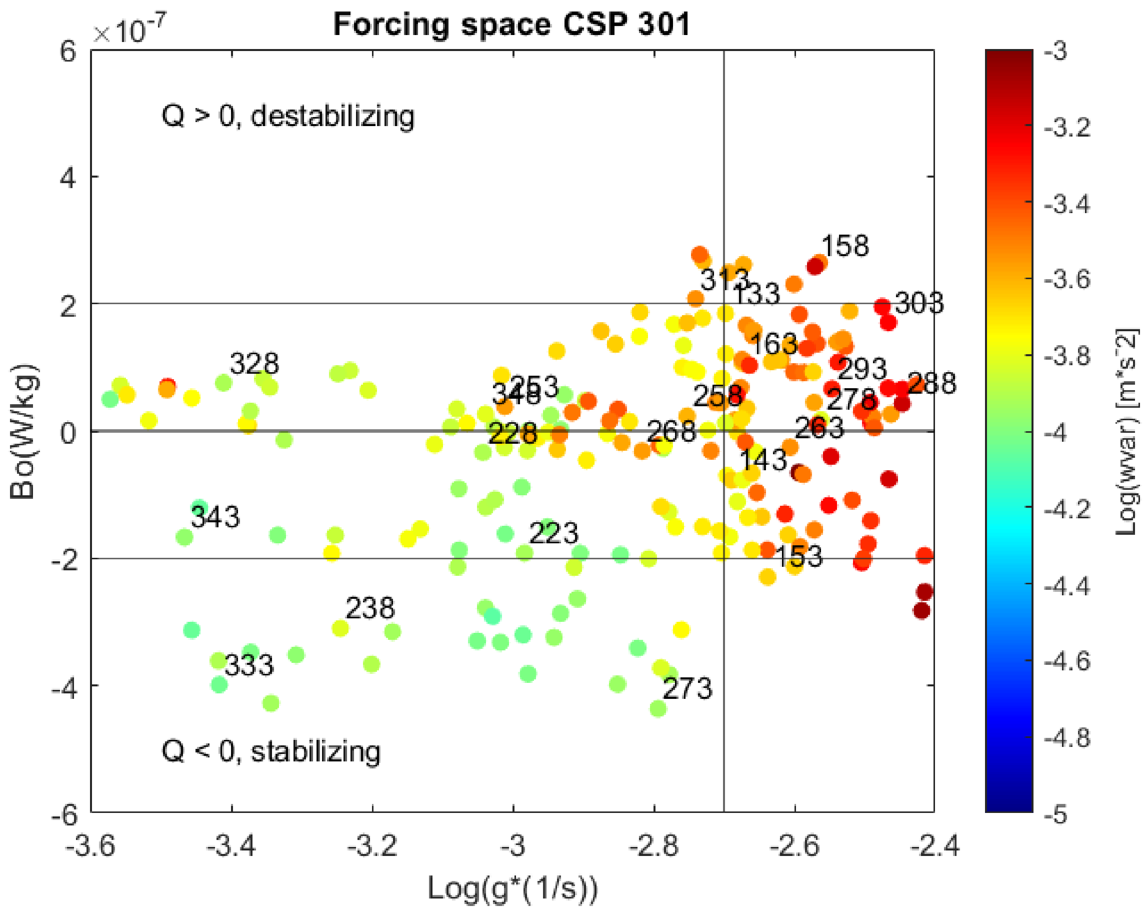


Figure 6.13: Forcing Space for CSP 301 dataset, numbers northeast of circles denote record number, horizontal vertical line separates regions of stabilizing waters ($Q < 0$) and destabilizing waters ($Q > 0$), vertical reference line marks threshold for appearance of LSC ($log_{10}(g^*) = -2.7$).

Critical $g^*$ accompanied by high vertical velocity fluctuations are reached twice during CSP301 (Fig. 6.12). Between records 180-197 (CSP 301 September LSC event), and between records 287-313 (CSP 301 October LSC event). Notice that vertical velocity fluctuations seem greater at CSP during this session compared to events at other locations. To better appreciate the differences between the two events in CSP 301, I will examine their forcing spaces separately.

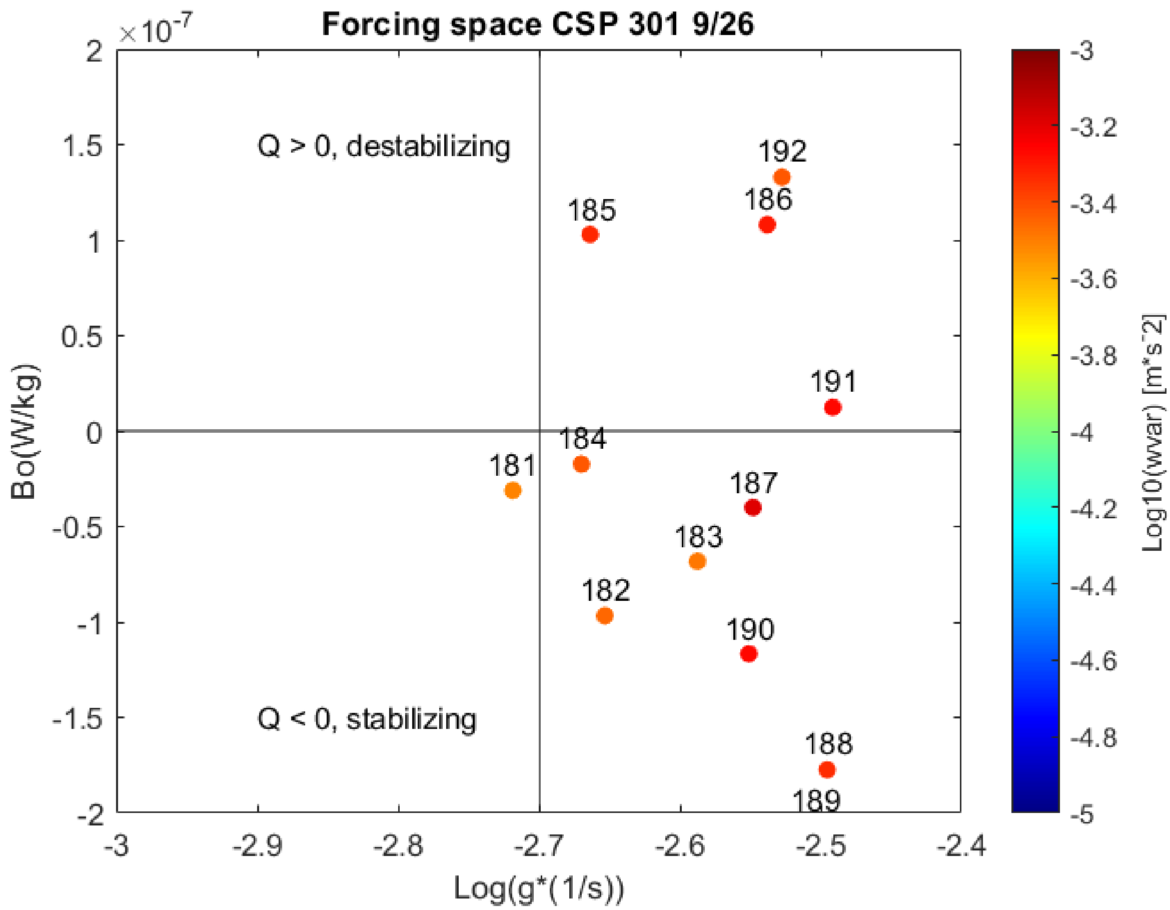


Figure 6.14: Forcing space for CSP 301 September 26th LSC event. Numbers northeast of circles denote record number, horizontal vertical line separates regions of stabilizing waters ($Q < 0$) and destabilizing waters ($Q > 0$), vertical reference line marks threshold for appearance of LSC ($log_{10}(g^{*}) = -2.7$).

On the 26th, after waters become unstratified, forcing space reveals that Langmuir forcing dominates turbulent production. Isolating CSP 301 September records reveal that all but one record at the beginning of the event has Langmuir growth rate values above critical (Fig. 6.13).

While $g^*$ does not vary much, $B_0$ sharply moves towards destabilizing conditions (182→183→184→185→186), and later towards stabilizing conditions (186→187→188→189), only to sharply move towards destabilizing waters at the end of the day (189→190→191). However, sharp changes in $B_0$ seem to take 4-6 hours to affect velocity fluctuations compared to sharp changes in $g^*$, which may affect fluctuations much faster. This change in $B_0$ is likely associated with the daily cycle in buoyancy forcing due to it being a function of surface heat flux.

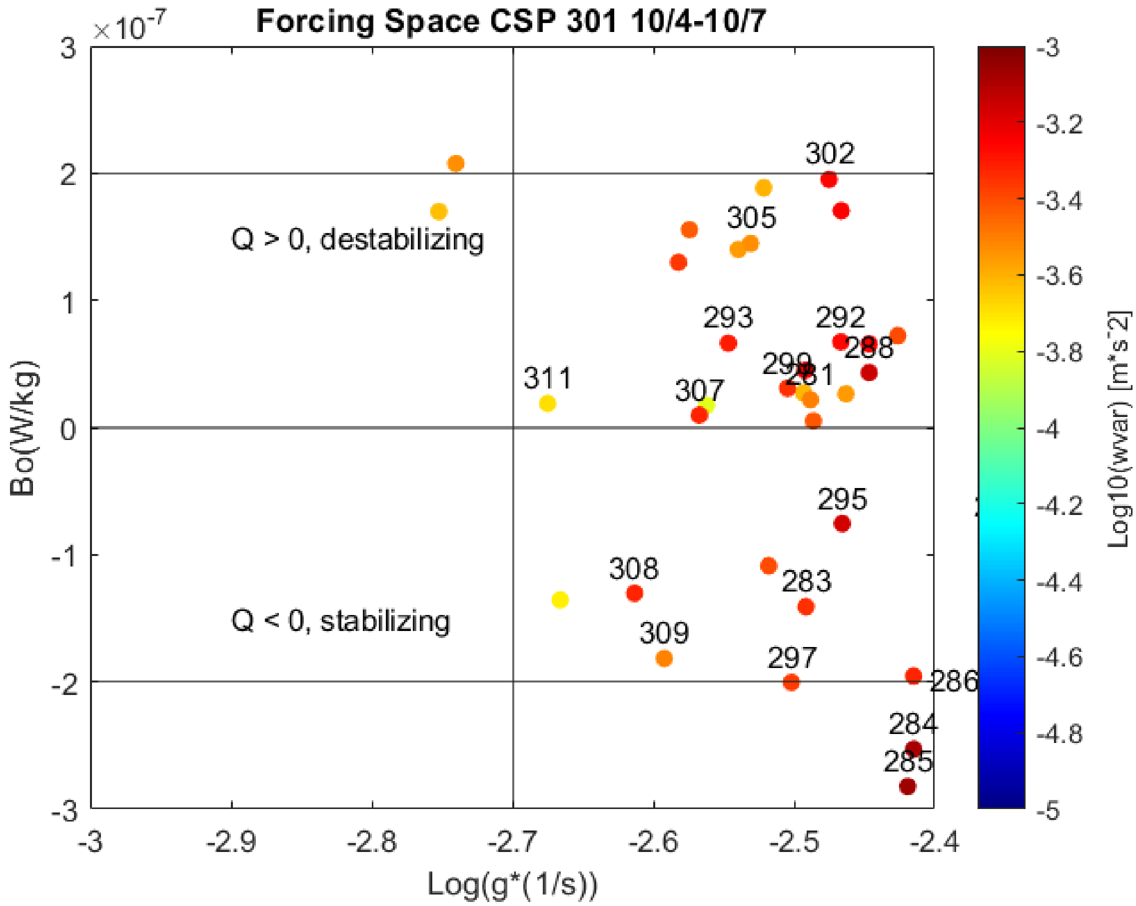


Figure 6.15: Forcing space for CSP 301 October 4th-7th LSC event. Numbers north of circles denote record number, horizontal vertical line separates regions of stabilizing waters ($Q < 0$) and destabilizing waters ($Q > 0$), vertical reference line marks threshold for appearance of LSC ($log_{10}(g^{*}) = -2.7$).

Analogous to the September event, the records during the October event fall within the $g^{*}$ threshold for LCS, reaching $g^{*}$ values greater than those of the previous event. There is fair variability of both $B_0$ and $g^{*}$ between records. Rapid changes in $B_0$ (310→311 or 284→285→286) do not immediately affect $\overline{w'^2}$, as expected, and rapid changes in $g^{*}$ (308→309→310 or 300→301→302→303) affect $\overline{w'^2}$ much quicker (Fig. 6.14). This could be related to the passage of hurricane Joaquin, which passed through the same latitude on October 4th.

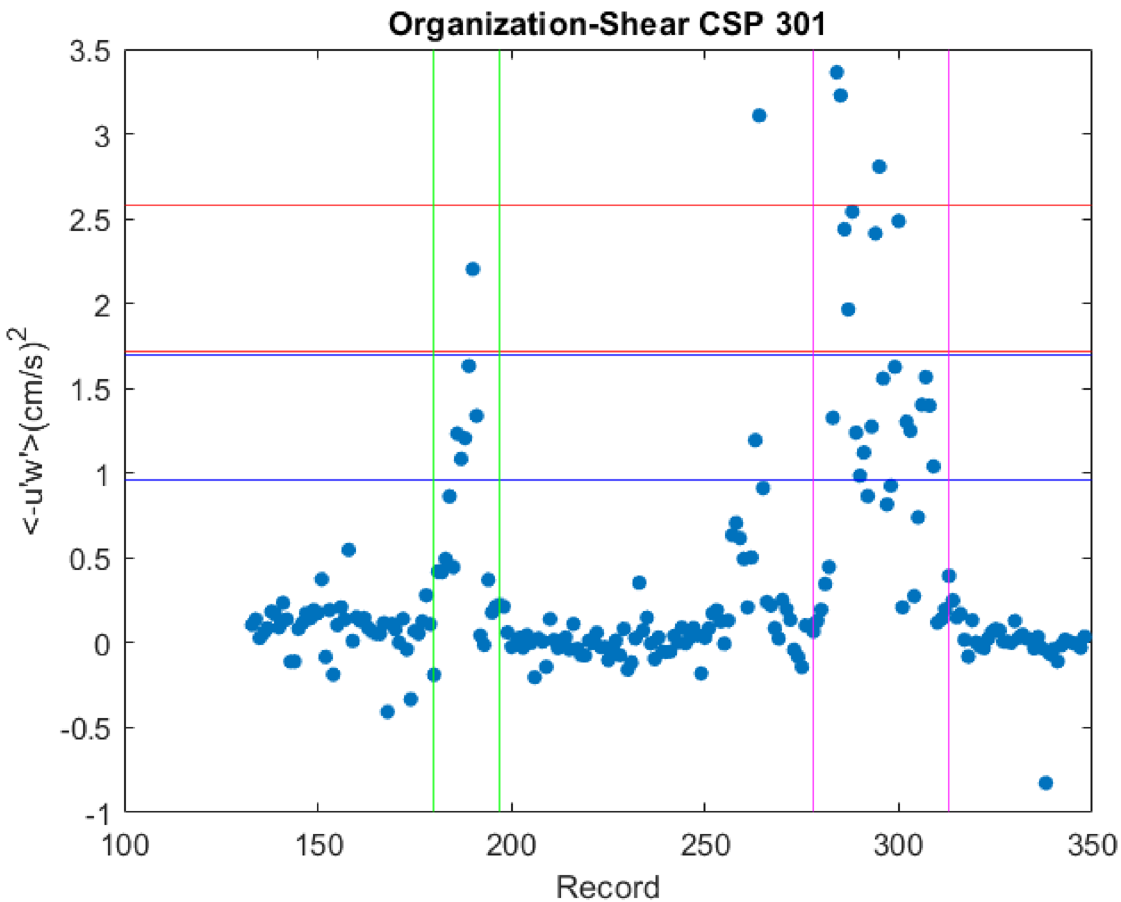


Figure 6.16: Shear turbulence stress fluctuations $\langle -u'w' \rangle$ for CSP 301. Blue reference lines denote values for records near or above critical $g^*$, and red reference lines denote values for records with $\log_{10}(g^*)$ between -2.6 and -2.4, like the archetypal LSC records in LEO 043. Vertical reference lines mark beginning and end of the September (green) and October (magenta) LSC events.

Shear fluctuations $\langle -u'w' \rangle$ for CSP 301 indicate that records during the LSC events exhibit relatively high values, while they are near zero when buoyancy forcing dominates turbulent production. Records with high shear fluctuations outside the bounds of events are likely attributable to increased Langmuir forcing, though not strong enough to generate full-depth LSC structures. Both the mean and peak shear fluctuations are higher for the second event; however, this does not guarantee that the second event is more organized than the first one (Fig. 6.15).

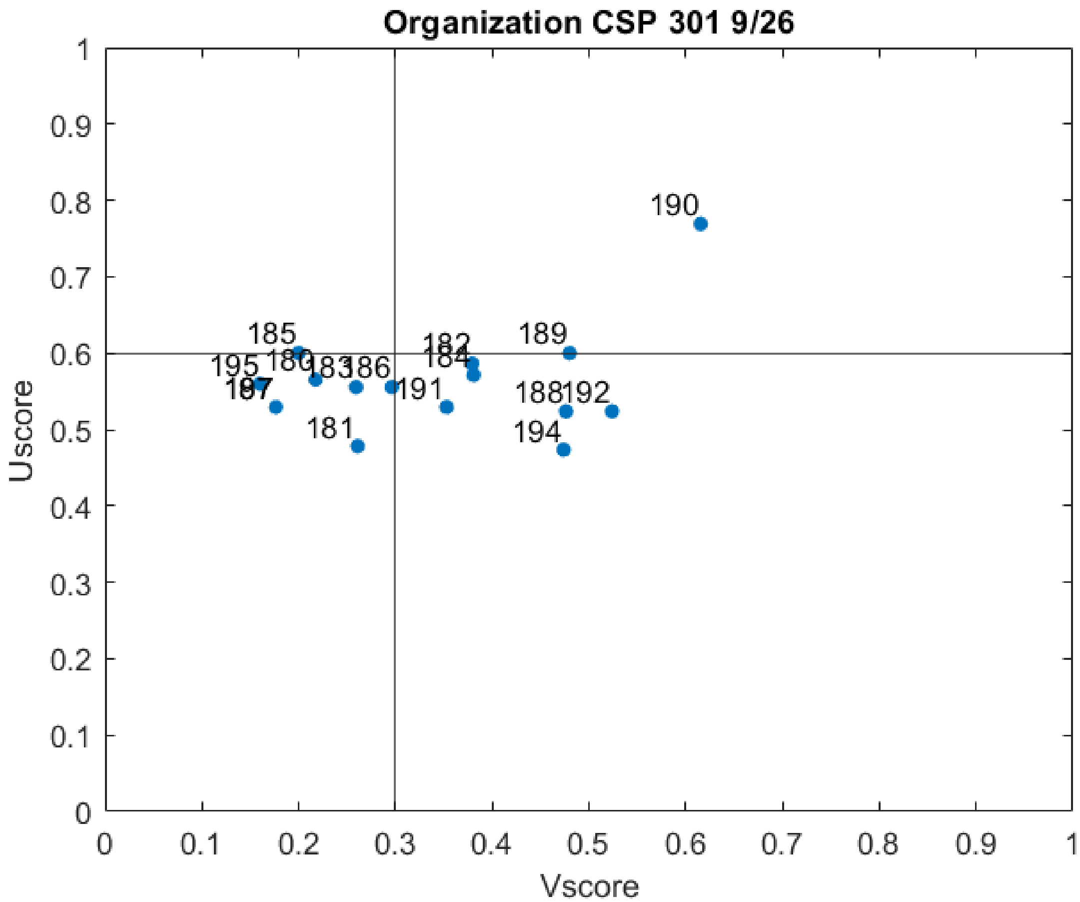


Figure 6.17: Organizational scores for CSP 301 September LSC event. Reference lines marks threshold for organized LSC records.

The CSP 301 September event features one organized record, with Uscore exhibiting minimal fluctuations, while Vscore varies significantly from one record to the next (Fig. 6.16). On average, this event ranks higher than the BUP 001 event during Tropical Storm Barry in both

Uscore and Vscore (Table 6.1), yet demonstrates lower organization compared to the events in BUP 023 and LEO 043.

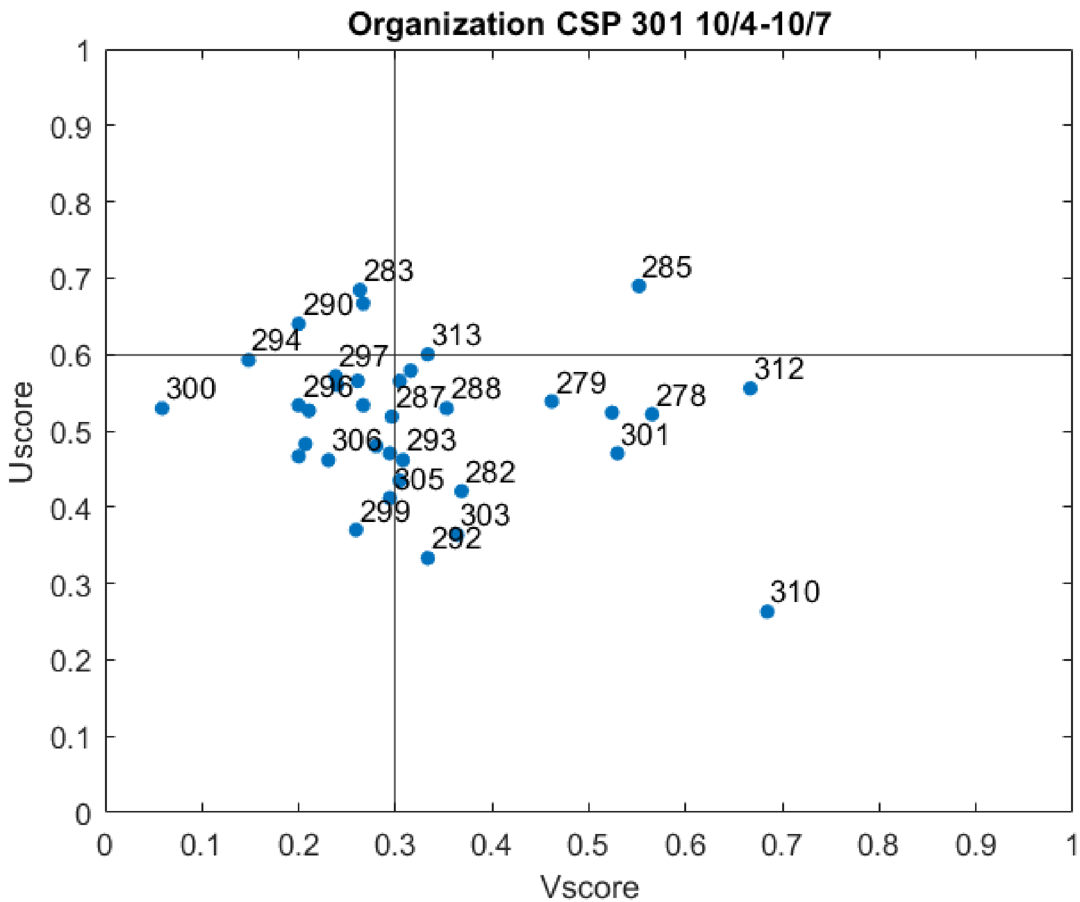


Figure 6.18: Organizational scores for CSP 301 LSC October event. Reference lines marks threshold for organized LSC records.

The organizational scores for the CSP 301 September event are noticeably higher than those for the CSP 301 October event (Fig. 6.16 and 6.17). Like the September event, only one of the records in the October event reaches the organized threshold. Despite having lower $g^*$ and lower $\langle -u'w' \rangle$ shear fluctuations, the CSP 301 September event exhibits greater average Uscore and Vscore values than the October event (Table 6.1). Furthermore, a significant portion of the October event fails to meet both Uscore and Vscore thresholds required for an organized event.

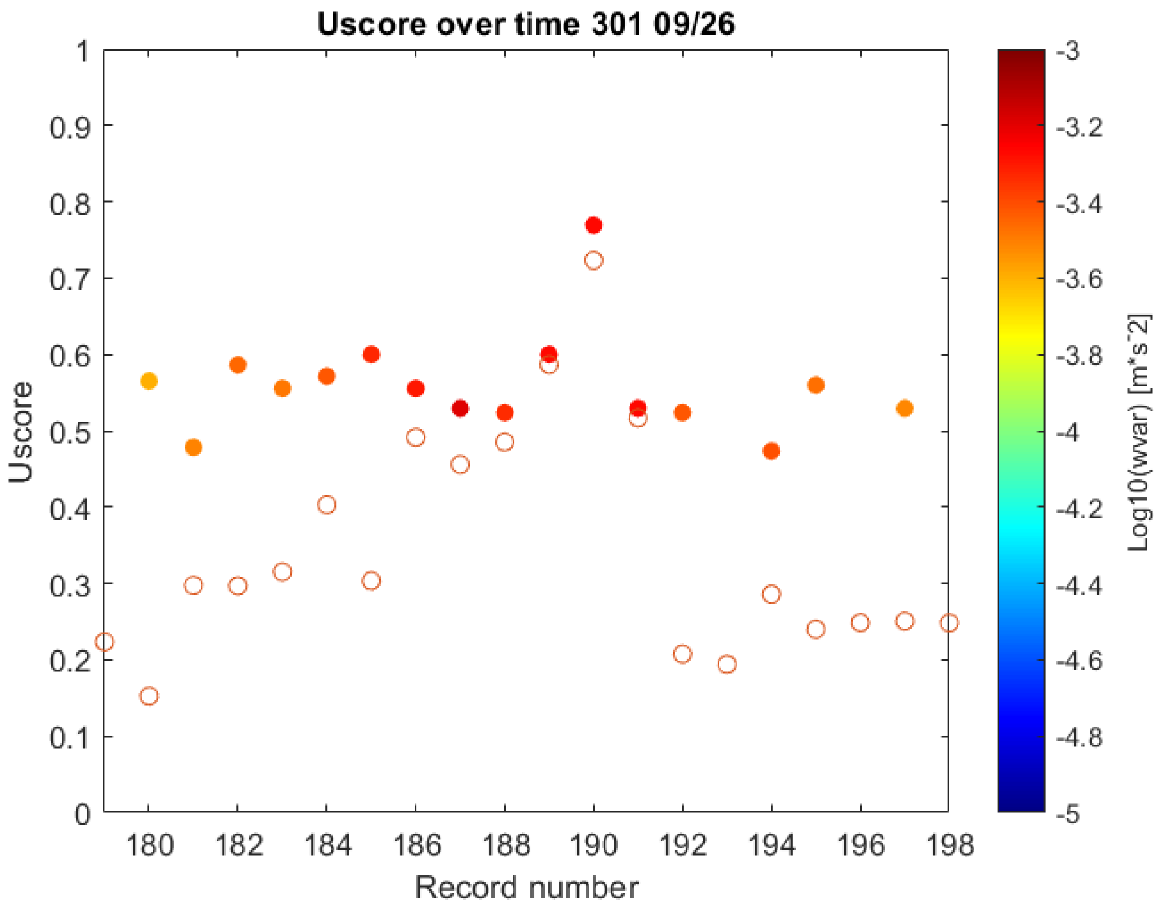


Figure 6.19: Downwind organizational scores (Filled – vertical velocity fluctuations) and scaled shear turbulent fluctuations (empty) over time for CSP 301 September.

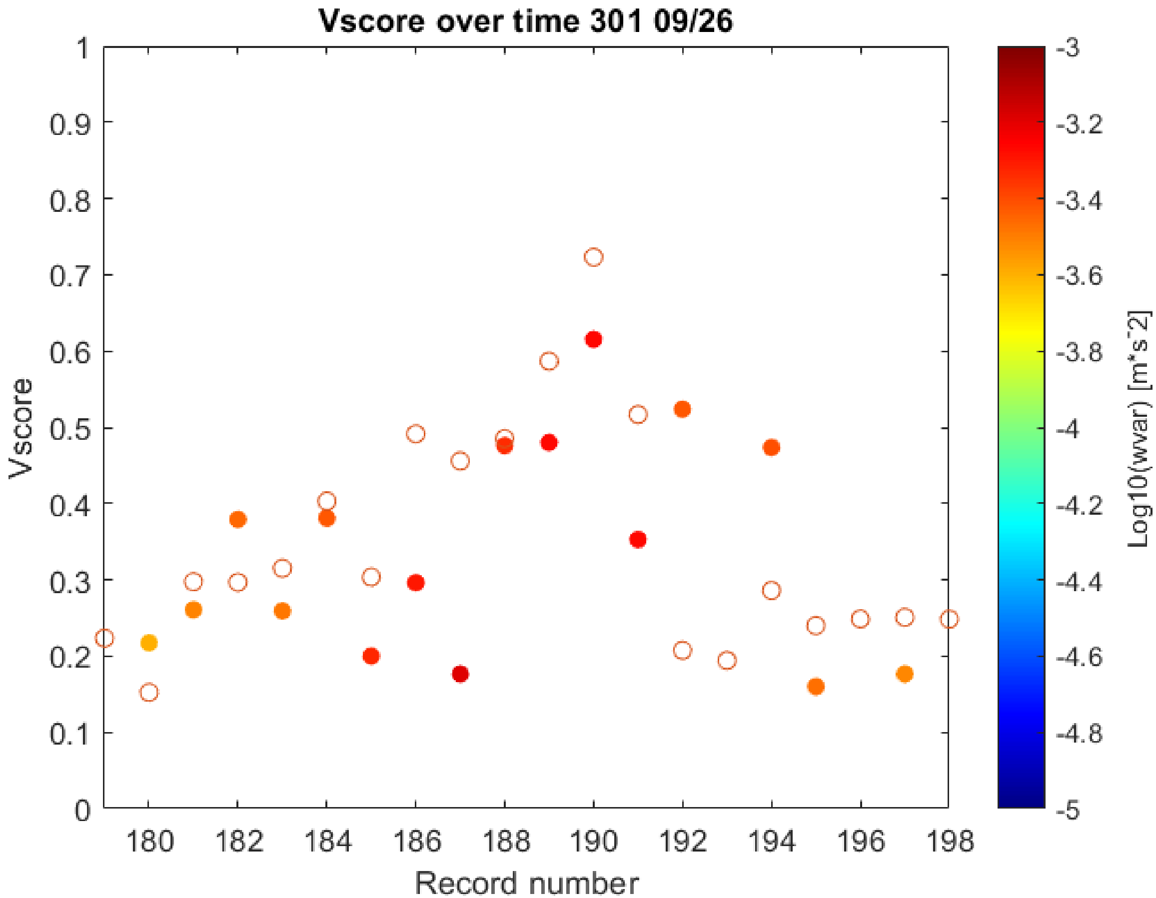


Figure 6.20: Crosswind organizational scores (Filled – vertical velocity fluctuations) and scaled shear turbulent fluctuations (empty) over time for CSP 301 September.

Interestingly, the CSP 301 September event exhibits a similar pattern to the archetypal LEO 043 event, where both Uscore and Vscore increase with $\langle -u'w' \rangle$ from the event's onset, reaching a maximum in record 191 (the sole organized record in the event), and subsequently decreasing as the Langmuir growth rate declines. A shared characteristic between both events is their development and dissipation within the same day, aligning with the same heat flux daily cycle, and not being influenced by the passage of a tropical storm or hurricane, as observed in the more chaotic BUP 001 and CSP 301 October events.

TABLE 6.1: Forcing parameters and organizational scores time-averaged between all records within given LSC event. Highlighted are highest (green) and lowest (red) parameter values between events.

| **Event** | $\overline{\langle La \rangle}$ | $\overline{\langle Ra \rangle}$ | $\overline{\langle B_0 \rangle}$ | $log_{10}\overline{\langle g^* \rangle}$ | $\overline{\langle Uscore \rangle}$ | $\overline{\langle Vscore \rangle}$ | $\overline{\langle -u'w' \rangle}$ |
|---|---|---|---|---|---|---|---|
| **CSP 301 Sep** | -1.0181 | 4.8673 | $1.0654 \times 10^{-8}$ | -2.5905 | 0.5594 | 0.3393 | **0.6761*** |
| **CSP 301 Oct** | -1.1581 | 4.7625 | $2.3598 \times 10^{-9}$ | -2.5133 | 0.5091 | 0.3243 | 1.2279 |
| **BUP 023** | -0.9106 | 5.0070 | $1.4339 \times 10^{-7}$ | -2.5307 | 0.6331 | 0.3554 | 1.8590 |
| **BUP 001** | -0.8938 | 5.2832 | $1.4658 \times 10^{-7}$ | -2.4755 | 0.5274 | 0.2484 | 1.1095 |
| **LEO 043** | -1.0215 | 4.4195 | $1.8475 \times 10^{-9}$ | -2.6365 | 0.7483 | 0.4503 | 1.2425 |

In Table 6.1 key average parameters for all events and sites and LSC events discussed herein are presented. Other events at these sites have similar parameters as the events focused on this work (with exception of BUP 001 due to TS Barry). All of the events fall within the (*La*, *Ra*) parameter space for LSC. While $\langle -u'w' \rangle$ seems to be a great parameter in separating structures generated due to convection and wave-wind forcing, a higher value for $\langle -u'w' \rangle$ does not guarantee higher structural organization when compared to events between different sites (BUP 023 had higher $\langle -u'w' \rangle$ than LEO 043) or between events at the same site (CSP 301 October had higher $\langle -u'w' \rangle$ than CSP 301 September).

BUP 023 exhibited the highest values of shear fluctuations, followed by the archetypal LEO 043, which is closely trailed by the CSP 301 October event, then BUP 001, with the CSP 301 September event ranking the lowest. Intriguingly, these results do not correspond to the ranking of sites concerning organizational scores, which would be led by LEO 043, and where the September CSP 301 event ranked higher than the October CSP 301 event.

$\langle -u'w' \rangle$ may be a key parameter when examining whether or not observed structures are generated due to turbulence production of LSC or convection but comparing organizational scores in the same location versus $\langle -u'w' \rangle$ seems to reveal that there are cases at the same site where stronger shear fluctuations correlate to stronger organizational scores (BUP) and there are cases where weaker shear fluctuations correlate to weaker organizational scores (CSP).

Since organizational scores are directly associated with the structure of LSC, they may provide a more accurate measure of organization than shear fluctuations, particularly once shear fluctuations are employed to distinguish instances of convection and Langmuir forcing domination.

Looking at the cases at the same sites, higher $g^*$ is associated with higher organizational scores (Table 6.1), as CSP 301 Sep event had higher average $g^*$, Uscore, and Vscore than CSP 301 Oct, and BUP 023 had higher average $g^*$, Uscore, and Vscore than BUP 001.

Organization appears to diminish with depth, with the exception of the BUP 001 event, which was likely due to the passage of Tropical Storm Barry and change of LSC orientation with depth. Nevertheless, even deeper sites such as CSP present LSC events with records within the threshold for organized LSC proposed in the appendix of Gargett and Savidge (2020), with Uscore > 0.6 and Vscore > 0.3.

In summary, higher $\langle -u'w' \rangle$ does not guarantee higher organizational values. Organizational scores seem to be a more effective way of representing organization once shear fluctuations disclose whether observed structures are due to buoyancy or Langmuir forcing. Higher values for $\langle -u'w' \rangle$ at BUP 023 could be associated with waters being highly destabilized.

The event of CSP 301 Oct also had higher shear fluctuations compared to the previous CSP 301 Sep event despite having lower $g^*$, Uscore, and Vscore. Another possible difference could be related to the waters being unstratified for the CSP 301 October event but previously stratified for the CSP 301 September event.

## 6.4 CONCLUSION AND FUTURE WORK

Various methods for evaluating the organization of Langmuir Supercells (LSC) have been proposed to better quantify the orderliness of a given event's structure. In this study, organizational scores and shear turbulent fluctuations were estimated for different events at three distinct sites with varying depths. A key conclusion of this research is that neither organizational scores nor $\langle -u'w' \rangle$ values are sufficient on their own to determine if a particular LSC event is organized, or if it is more or less organized than another event at a different site. However, their limitations seem to complement each other.

While $\langle -u'w' \rangle$ serves as a useful tool to determine if observed turbulent structures are a product of convection or LSC, it does not effectively assess whether one LSC event is more or less organized than another, either between sites (e.g., BUP 023 having greater $\langle -u'w' \rangle$ than LEO 043) or within a site (e.g., CSP 301 October event having greater $\langle -u'w' \rangle$ than CSP 301 September event).

Organizational scores accurately distinguish highly organized events (e.g., LEO 043) from less organized events (e.g., BUP 001). However, the arbitrary nature of Uscore and Vscore suggests that modifications to the proposed estimation method could improve its ability to capture and differentiate more organized LSC structures from other turbulent structures. For instance, Vscore could be adjusted to consider whether crosswind fluctuations change direction at all, while Uscore could be made a function of $\langle -u'w' \rangle$, as the primary feature of organized LSC is that downward vertical velocity regions coincide with enhanced near-bottom downwind velocity fluctuations and upward vertical velocity regions coincide with negative near-bottom downwind velocity fluctuations. By definition, these characteristics would be reflected in increased $\langle -u'w' \rangle$ values. Integrating organizational scores and $\langle -u'w' \rangle$ into a single organizational system could address the shortcomings of organizational scores, as non-zero $\langle -u'w' \rangle$ values would distinguish LSC events from convection.

LSC event organization appears to decrease with depth, but the reasons for this decrease warrant further investigation. If LSC changes orientation with depth, then Uscore and Vscore might not fully account for the two major features used to estimate LSC organization unless corrected for that change in orientation.

# CHAPTER 7

## CONCLUSION AND FUTURE WORK

This dissertation has made significant contributions to our understanding of Langmuir Supercells (LSC) behavior, parameterization, and structural organization at varying depths. Through the development and application of novel methodologies and an examination of LSC organization, this research has provided valuable insights into LSC dynamics and their impact on ocean mixing and transport processes. The key findings from this study can be summarized as follows:

1. The rotary spectra method was successfully developed as an alternative wave-turbulence separation technique, proving promising for simulated data and *in situ* datasets.
2. The novel ECAD method for estimating longwave and shortwave radiation data in the absence of pyranometer data was introduced and demonstrated as a viable alternative for analyzing LSC events.
3. The combination of organizational scores and $\langle -u'w' \rangle$ values provided a more comprehensive understanding of LSC event organization at different depths.
4. The observation of LSC event organization decreasing with depth contributed to a deeper understanding of the phenomenon and its implications on oceanic processes.

Of particular interest to the engineering community are the potential implications of LSC on oil spill response strategies and coastal ecosystem management. LSC has been shown to affect the dispersion and transport of pollutants, such as oil spills, in the ocean. Additionally, LSC can impact sediment transport and resuspension in the benthic boundary layer, with important implications for coastal ecosystem management. In light of these accomplishments, several areas for future work have been identified. These include addressing the limitations encountered in this study and further refining the methodologies employed to enhance our understanding of LSC dynamics and their impacts on ocean mixing and transport processes.

Future work could focus on improving the rotary spectra method for wave separation, refining the ECAD method for estimating radiation data, and developing a more comprehensive system for evaluating LSC organization. Additionally, investigating the underlying reasons for the decrease in LSC event organization with depth and conducting more in-depth analysis of orientation changes in LSCs at different depths could further refine the estimation methods for LSC organization. Continued research on LSC dynamics at varying depths and under different forcing conditions will contribute to a more complete understanding of these turbulent phenomena and their implications for oceanic processes. Refining the methodologies employed in this study can enhance our understanding of LSC dynamics and their impacts on ocean mixing and transport processes. Lastly, the rotary spectra method to separate fluctuations from waves and turbulence may have an impact on research in the turbulent community, not only as a new tool which can be compared to alternatives and used when reasonable, it provides a new outlook into the problem.

REFERENCES


Bishop, C. T., & Donelan, M. A. (1987). Measuring waves with pressure transducers. Coastal Engineering, 11(4), 309-328.Doi: https://doi.org/10.1016/0378-3839(87)90031-7

Bricker, J. D., & Monismith, S. G. (2007). Spectral Wave–Turbulence Decomposition, Journal of Atmospheric and Oceanic Technology, 24(8), 1479-1487. doi: https://doi.org/10.1175/JTECH2066.1

Cahoon, L. B., Laws, R. A., & Thomas, C. J. (1994). Viable diatoms and chlorophylla in continental slope sediments off Cape Hatteras, North Carolina. Deep Sea Research Part II: Topical Studies in Oceanography, 41(4-6), 767-782.doi: https://doi.org/10.1016/0967-0645(94)90047-7

Chubarenko, I., Chubarenko, B., Esiukova, E., & Baudler, H. (2010). Mixing by Langmuir circulation in shallow lagoons Irina Chubarenko, Boris Chubarenko, Elena Esiukova, Henning Baudler. Baltica, 23(1).

Craik, A., & Leibovich, S. (1976). A rational model for Langmuir circulations. Journal of Fluid Mechanics, 73(3), 401-426. doi:10.1017/S0022112076001420

Dierssen, H. M., Zimmerman, R. C., Drake, L. A., & Burdige, D. J. (2009). Potential export of unattached benthic macroalgae to the deep sea through wind-driven Langmuir circulation. Geophysical Research Letters, 36(4).doi: https://doi.org/10.5194/bg-6-487-2009, 2009.

Fairall, C. W., Bradley, E. F., Rogers, D. P., Edson, J. B., & Young, G. S. (1996). Bulk parameterization of air-sea fluxes for tropical ocean-global atmosphere coupled-ocean atmosphere response experiment. Journal of Geophysical Research: Oceans, 101(C2), 3747-3764.doi:  https://doi.org/10.1029/95JC03205

Feddersen, F., & Williams , A. J., III. (2007). Direct Estimation of the Reynolds Stress Vertical Structure in the Nearshore, Journal of Atmospheric and Oceanic Technology, 24(1), 102-116. doi: https://doi.org/10.1175/JTECH1953.1

Fung, I. Y., Harrison, D. E., & Lacis, A. A. (1984). On the variability of the net longwave radiation at the ocean surface. Reviews of Geophysics, 22(2), 177-193.doi:https://doi.org/10.1029/RG022i002p00177

Gargett, A. E. (2022). Forcing Space: An Alternative to Regime Diagrams for Predicting Characteristics of Turbulence in the Ocean Surface Mixing Layer, Journal of Physical Oceanography, 52(3), 519-535. doi: https://doi.org/10.1175/JPO-D-21-0145.1

Gargett, A. E., & Grosch, C. E. (2014). Turbulence Process Domination under the Combined Forcings of Wind Stress, the Langmuir Vortex Force, and Surface Cooling, Journal of Physical Oceanography, 44(1), 44-67. doi: https://doi.org/10.1175/JPO-D-13-021.1

Gargett, A. E., & Savidge, D. K. (2020). Winds, Waves, and Turbulence on a Shallow Continental Shelf during Passage of a Tropical Storm, Journal of Physical Oceanography, 50(5), 1341-1364. doi: https://doi.org/10.1175/JPO-D-20-0024.1

Gargett, A., & Wells, J. (2007). Langmuir turbulence in shallow water. Part 1. Observations. Journal of Fluid Mechanics, 576, 27-61. doi:10.1017/S0022112006004575

Gargett, A., Savidge, D. K., & Wells, J. R. (2016). Necessary Conditions for the Langmuir Supercell Events That Dominate Sediment Transport on Shallow Shelves. American Geophysical Union, 2016, MG14A-1881.

Gargett, A., Wells, J., Tejada-Martinez, A. E., & Grosch, C. E. (2004). Langmuir supercells: A mechanism for sediment resuspension and transport in shallow seas. Science, 306(5703), 1925-1928. DOI: 10.1126/science.1100849

Grosch, C. E., & Gargett, A. E. (2016). Why Do LES of Langmuir Supercells Not Include Rotation?, Journal of Physical Oceanography, 46(12), 3595-3597. doi: https://doi.org/10.1175/JPO-D-16-0092.1

Jahnke, R. A., Nelson, J. R., Richards, M. E., Robertson, C. Y., Rao, A. M. F., & Jahnke, D. B. (2008). Benthic primary productivity on the Georgia midcontinental shelf: Benthic flux measurements and high-resolution, continuous in situ PAR records. Journal of Geophysical Research: Oceans, 113(C8). doi:https://doi.org/10.1029/2008JC004745

Kirincich, A. R., & Rosman, J. H. (2011). A Comparison of Methods for Estimating Reynolds Stress from ADCP Measurements in Wavy Environments, Journal of Atmospheric and Oceanic Technology, 28(11), 1539-1553. doi: https://doi.org/10.1175/JTECH-D-11-00001.1

Kitaigorodskii, S. A., & Lumley, J. L. (1983). Wave-Turbulence interactions in the Upper Ocean. Part I: The Energy Balance of the Interacting Fields of Surface Wind Waves and Wind-Induced Three-Dimensional Turbulence, Journal of Physical Oceanography, 13(11), 1977-1987. doi: https://doi.org/10.1175/1520-0485(1983)013<1977:WTIITU>2.0.CO;2

Langmuir, I. (1938). Surface motion of water induced by wind. Science, 87(2250), 119-123.doi: 10.1126/science.87.2250.11

Large, W. G., & Pond, S. (1981). Open Ocean Momentum Flux Measurements in Moderate to Strong Winds, Journal of Physical Oceanography, 11(3), 324-336. doi: https://doi.org/10.1175/1520-0485(1981)011<0324:OOMFMI>2.0.CO;2

Leibovich, S. (1977). On the evolution of the system of wind drift currents and Langmuir circulations in the ocean. Part 1. Theory and averaged current. Journal of Fluid Mechanics, 79(4), 715-743. doi:10.1017/S002211207700041X.

Leibovich, S. (1983). The form and dynamics of Langmuir circulations. Annual Review of Fluid Mechanics, 15(1), 391-427.doi: http://dx.doi.org/10.1146/annurev.fl.15.010183.002135

Li, K., Zhang, Z., Chini, G., & Flierl, G. (2012). Langmuir Circulation: An Agent for Vertical Restratification?, Journal of Physical Oceanography, 42(11), 1945-1958. doi: https://doi.org/10.1175/JPO-D-11-0225.1

Li, M., & Garrett, C. (1995). Is Langmuir Circulation Driven by Surface Waves or Surface Cooling?, Journal of Physical Oceanography, 25(1), 64-76. doi: https://doi.org/10.1175/1520-0485(1995)025<0064:ILCDBS>2.0.CO;2

Li, M., Garrett, C., & Skyllingstad, E. (2005). A regime diagram for classifying turbulent large eddies in the upper ocean. Deep Sea Research Part I: Oceanographic Research Papers, 52(2), 259-278.doi:https://doi.org/10.1016/j.dsr.2004.09.004

Malarkey, J., & Thorpe, S. A. (2016). Line Vortices and the Vacillation of Langmuir Circulation, Journal of Physical Oceanography, 46(7), 2123-2141. doi: https://doi.org/10.1175/JPO-D-16-0006.1

Mcwilliams, J., SULLIVAN, P., & MOENG, C. (1997). Langmuir turbulence in the ocean. Journal of Fluid Mechanics, 334, 1-30. doi:10.1017/S0022112096004375

Mooers, C. N. (1973, December). A technique for the cross spectrum analysis of pairs of complex-valued time series, with emphasis on properties of polarized components and rotational invariants. In Deep Sea Research and Oceanographic Abstracts (Vol. 20, No. 12, pp. 1129-1141).Elsevier.doi:https://doi.org/10.1016/0011-7471(73)90027-2

Münchow, A., & Chant, R. J. (2000). Kinematics of Inner Shelf Motions during the Summer Stratified Season off New Jersey, Journal of Physical Oceanography, 30(2), 247-268. doi: https://doi.org/10.1175/1520-0485(2000)030<0247:KOISMD>2.0.CO;2

Nelson, J. R., Eckman, J. E., Robertson, C. Y., Marinelli, R. L., & Jahnke, R. A. (1999). Benthic microalgal biomass and irradiance at the sea floor on the continental shelf of the South Atlantic Bight: spatial and temporal variability and storm effects. Continental Shelf Research, 19(4), 477-505. doi: https://doi.org/10.1016/S0278-4343(98)00092-2

Pawlowicz, R., Beardsley, B., Lentz, S., Dever, E., & Anis, A. (2001). Software simplifies air-sea data estimates.doi:  https://doi.org/10.1029/01EO00004

Polton, J. A., & Belcher, S. E. (2007). Langmuir turbulence and deeply penetrating jets in an unstratified mixed layer. Journal of Geophysical Research: Oceans, 112(C9). doi: https://doi.org/10.1029/2007JC004205

Pugh, D. T. (1996). Tides, surges and mean sea-level (reprinted with corrections).

Reed, R. K. (1977). On Estimating Insolation over the Ocean, Journal of Physical Oceanography, 7(3), 482-485. doi: https://doi.org/10.1175/1520-0485(1977)007<0482:OEIOTO>2.0.CO;2

Reichl, B. G., Ginis, I., Hara, T., Thomas, B., Kukulka, T., & Wang, D. (2016). Impact of Sea-State-Dependent Langmuir Turbulence on the Ocean Response to a Tropical Cyclone, Monthly Weather Review, 144(12), 4569-4590. doi: https://doi.org/10.1175/MWR-D-16-0074.1

Savidge, D. K., & Gargett, A. E. (2017). Langmuir supercells on the middle shelf of the South Atlantic Bight: 1. Cell structure. Journal of Marine Research, 75(2), 49-79.

Savidge, W. B., Gargett, A., Jahnke, R. A., Nelson, J. R., Savidge, D. K., Short, R. T., & Voulgaris, G. (2008). Forcing and Dynamics of Seafloor-Water Column Exchange on a Broad Continental Shelf. Oceanography, 21(4), 179–185. doi:http://www.jstor.org/stable/24860023

Scully, M. E., Fisher, A. W., Suttles, S. E., Sanford, L. P., & Boicourt, W. C. (2015). Characterization and Modulation of Langmuir Circulation in Chesapeake Bay, Journal of Physical Oceanography, 45(10), 2621-2639. doi: https://doi.org/10.1175/JPO-D-14-0239.1

Seim, H. E. (2000). Implementation of the South Atlantic Bight synoptic offshore observational network. Oceanography, 13(SPL. ISS. 2), 18-23. doi: 10.5670/oceanog.2000.29

Shaw, W. J., & Trowbridge, J. H. (2001). The Direct Estimation of Near-Bottom Turbulent Fluxes in the Presence of Energetic Wave Motions, Journal of Atmospheric and Oceanic Technology, 18(9), 1540-1557. doi: https://doi.org/10.1175/15200426(2001)018<1540:TDEONB>2.0.CO;2

Smith, J. A. (2001). Observations and theories of Langmuir circulation: a story of mixing. In Fluid Mechanics and the Environment: Dynamical Approaches: A Collection of Research Papers Written in Commemoration of the 60th Birthday of Sidney Leibovich (pp. 295-314). Berlin, Heidelberg: Springer Berlin Heidelberg. https://doi.org/10.1007/3-540-44512-9_16

Smith, S. D. (1988). Coefficients for sea surface wind stress, heat flux, and wind profiles as a function of wind speed and temperature. Journal of Geophysical Research: Oceans, 93(C12), 15467-15472.Doi:https://doi.org/10.1029/JC093iC12p15467

Teixeira, M. A. C. (2018). A Model for the Wind-Driven Current in the Wavy Oceanic Surface Layer: Apparent Friction Velocity Reduction and Roughness Length Enhancement, Journal of Physical Oceanography, 48(11), 2721-2736. doi: https://doi.org/10.1175/JPO-D-18-0086.1

Tejada-Martínez, A., & Grosch, C. (2007). Langmuir turbulence in shallow water. Part 2. Large-eddy simulation. Journal of Fluid Mechanics, 576, 63-108. doi:10.1017/S0022112006004587

Thorpe, S. A. (2004). Langmuir circulation. Annu. Rev. Fluid Mech., 36, 55-79.

Trowbridge, J. H. (1998). On a Technique for Measurement of Turbulent Shear Stress in the Presence of Surface Waves, Journal of Atmospheric and Oceanic Technology, 15(1), 290-298. doi: https://doi.org/10.1175/1520-0426(1998)015<0290:OATFMO>2.0.CO;2

Walker, R., Tejada-Martínez, A. E., & Grosch, C. E. (2016). Large-Eddy Simulation of a Coastal Ocean under the Combined Effects of Surface Heat Fluxes and Full-Depth Langmuir Circulation, Journal of Physical Oceanography, 46(8), 2411-2436. doi: https://doi.org/10.1175/JPO-D-15-0168.1

Wang, Q., Alappattu, D. P., Billingsley, S., Blomquist, B., Burkholder, R. J., Christman, A. J., Creegan, E. D., de Paolo, T., Eleuterio, D. P., Fernando, H. J. S., Franklin, K. B., Grachev, A. A., Haack, T., Hanley, T. R., Hocut, C. M., Holt, T. R., Horgan, K., Jonsson, H. H., Hale, R. A., Kalogiros, J. A., Khelif, D., Leo, L. S., Lind, R. J., Lozovatsky, I., Planella-Morato, J., Mukherjee, S., Nuss, W. A., Pozderac, J., Ted Rogers, L., Savelyev, I., Savidge, D. K., Kipp Shearman, R., Shen, L., Terrill, E., Marcela Ulate, A., Wang, Q., Travis Wendt, R., Wiss, R., Woods, R. K., Xu, L., Yamaguchi, R. T., & Yardim, C. (2018). CASPER: Coupled Air–Sea Processes and Electromagnetic Ducting Research, Bulletin of the American Meteorological Society, 99(7), 1449-1471. doi: https://doi.org/10.1175/BAMS-D-16-

Yan, C., McWilliams, J. C., & Chamecki, M. (2022). Overlapping Boundary Layers in Coastal Oceans, Journal of Physical Oceanography, 52(4), 627-646. doi: https://doi.org/10.1175/JPO-D-21-0067.1